Self-Induced Transparency Solitons in Nanophotonic Waveguides

Andreas Pusch

2012

Thesis submitted for the degree of Doctor of Philosophy of Imperial College

Department of Physics

Imperial College London

Declaration of Originality

I hereby declare that the material presented in this thesis is my own work unless otherwise cited or acknowledged in the text.

Andreas Pusch

Abstract

This thesis explores the existence and properties of self-induced transparency (SIT) solitons in nanophotonic waveguides. SIT solitons are shape-preserving solutions of the semi-classical Maxwell-Bloch equations, a system of nonlinearly coupled differential equations. In a first investigation, collisions of counterpropagating simultons (SIT solitons in absorbing three-level systems) are studied numerically in the plane-wave approximation and a polarisation- and group-velocity dependent soliton birth is uncovered. Apart from their fundamental interest, such light-light interaction effects may be of use for optical computing applications if they can be transferred to tightly confined light pulses. Confining light is usually achieved by using dielectric waveguides that exhibit group velocity dispersion leading to chirped pulses, which experience absorption when entering an absorbing medium. If the chirp is strong enough and the pulse intense enough, they can even completely invert an absorber. When investigating chirped pulse propagation through a dense ensemble of two-level system it is found that the chirped pulses dynamically reshape into unchirped pulses experiencing transparency. Furthermore, the conditions on the waveguide geometry to enable SIT are analysed, identifying a nanophotonic slot waveguide with a low-index gap, exhibiting high electric field enhancement and a homogeneous field profile, as the ideal candidate system for guided SIT solitons. This analysis is supported by two-dimensional numerical calculations that show the solitary character is maintained during propagation if the absorber density is high enough to ensure a slow-down of the pulse and to thus counteract the waveguide dispersion. Finally, the soliton birth due to simulton collisions and optical memory schemes proposed for plane-wave SIT are investigated in the two-dimensional slot waveguide and found to also be possible in this geometry.

Acknowledgements

I want to thank...

- my supervisor Prof. Ortwin Hess for giving me the opportunity to perform research over a period of 4 years, for the freedom to follow my own curiosity, and the opportunity to collaborate on other projects in the group.
- Dr. Klaus Bhringer for the initial introduction to the intricacies of the numerical simulation of Maxwell-Bloch equations.
- Dr. Joachim Hamm for the reliable and easily extendable FDTD code, for always being there to discuss physics or numerical implementations, especially for pointing me towards the slot waveguide, for helping me write our publications and also for creating Figure 6.6 of this thesis.
- Sebastian Wuestner for being a reliable and always helpful friend and colleague, always listening (or pretending to listen) to my ramblings, always providing me with a snippet of code for a particular computational task, and whose research, to which I could also contribute, provided me with much needed variety.
- Dr. Kosmas Tsakmakidis for a number of nice and passionate discussions and the many creative and instructive hours spent writing together.
- my fellow PhD students for proofreading parts of my thesis, many a nice lunch-time conversation, and the nice workplace atmosphere.

I also am grateful to my friends for much entertainment, emotional support, and for teaching me to play pool.

Last but not least I am very much indebted to my parents and my sisters for all the support, in many ways, that they have given me over the years.

It seems to be the inexorable laws of supply and demand that forces the lower classes into the slavery of poverty. And an individual can no more dispute this power than the winds and tides. But in reality, it is the same cause that always has, and always must, result in slavery:

The monopolization by some of what nature meant for all.

As long as we recognize private property in land, our boasted freedom will inevitably involve slavery. Until it is abolished, Declarations of Independence and Acts of Emancipation are in vain. So long as one person can claim exclusive ownership of land – from which other people must live – slavery will exist. Indeed, as material progress grows, it must grow and deepen.

Henry George, *Progress and Poverty*

List of Publications

Portions of this thesis have been drawn from the following publications and manuscripts:

A. Pusch, J. M. Hamm and O. Hess, "Controllable interaction of counterpropagating solitons in three-level media", *Phys. Rev. A*, **82** 023805 (2010)

A. Pusch, J. M. Hamm and O. Hess, "Femtosecond nanometer-sized optical solitons", *Phys. Rev. A*, **84** 023827 (2011)

A. Pusch, J. M. Hamm and O. Hess, "Dynamic transition from complete population transfer to self-induced transparency", *Phys. Rev. A*, **85** 043807 (2012)

The following articles have been published during my PhD but not included in this thesis:

S. Wuestner, A. Pusch, K. L. Tsakmakidis, J. M. Hamm and O. Hess, "Overcoming Losses with Gain in a Negative Refractive Index Metamaterial", *Phys. Rev. Lett.*, **105** 127401 (2010)

S. Wuestner, A. Pusch, K. L. Tsakmakidis, J. M. Hamm and O. Hess, "Gain and plasmon dynamics in negative-index metamaterials", *Phil. Trans. R. Soc. A*, **369** 3525 (2011)

S. Wuestner, E. I. Kirby, A. Pusch, K. L. Tsakmakidis, J. M. Hamm, and O. Hess, "Gain in negative-index metamaterials and slow-light waveguides," *Proc. of SPIE* (Metamaterials: Fundamentals and Applications III) **7754**, 775414 (2010)

S. Wuestner, A. Pusch, K. L. Tsakmakidis, J. M. Hamm and O. Hess, "Comment on "Spaser Action, Loss Compensation, and Stability in Plasmonic Systems with Gain", *Phys. Rev. Lett.* **107** 259701 (2011)

A. Pusch, S. Wuestner, J. M. Hamm, K. L. Tsakmakidis and O. Hess, "Coherent Amplification and Noise in Gain-Enhanced Nanoplasmonic Metamaterials: A Maxwell-Bloch Langevin Approach", *ACS Nano*, **6** 2420 (2012)

S. Wuestner, J. M. Hamm, A. Pusch, F. Renn, K. L. Tsakmakidis and O. Hess, "Control and dynamic competition of bright and dark lasing states in active nanoplasmonic metamaterials", *Phys. Rev. B* **85** 201406 (2012)

Contents

Abstract **4**

Acknowledgements **5**

List of Publications **7**

List of Abbreviations **11**

List of Figures **13**

1 Introduction **15**

1.1 Background and motivation 15

1.2 Structure of the thesis 19

2 Light propagation **23**

2.1 The electromagnetic field 24

2.2 Waveguides 25

2.3 Optical solitons 33

3 Resonant light-matter interaction **39**

3.1 The optical Bloch equations 40

3.1.1 Two-level systems 41

3.1.2 Three-level systems 43

3.1.3 Local Field Effect and the effect of a Dielectric 45

3.2 Adiabatic rapid passage 45

3.3 Self-induced transparency 48

4 Simulton collisions **56**

4.1 Parallel polarisation 58

4.2 Orthogonal polarisation 61

4.3 Arbitrary relative polarisation 69

4.4 Conclusions 71

5 Adiabatic passage and self-induced transparency **73**

5.1 Adiabatic rapid passage in full time-domain 75

5.2 Pulse area theorem and adiabaticity condition 76

5.3 Resonant propagation of moderately chirped pulses 79

5.4 Resonant propagation of strongly chirped pulses 82

5.5 Conclusions 87

6 Self-induced transparency in nanophotonic waveguides **89**

6.1 One-dimensional equations and nonlinear propagation 90

6.1.1 Saturable nonlinearities 91

6.1.2 Saturable absorbers 92

6.1.3 Coherent absorbers 94

6.2 SIT in waveguides 99

6.3 Pulse collisions in gap waveguides 108

6.4 Memory schemes in $2D$ 112

6.5 Conclusions 113

7 Summary and Outlook **115**

A Numerical methods **119**

A.1 FDTD in one dimension 120

A.2 FDTD in two dimensions 121

A.3 Auxiliary differential equations 122

A.4 Pulse injection via the total field/scattered field method 124

A.5 Boundary conditions 125

A.6 Extraction of pulse velocities 126

A.7 Frequency-resolved optical gating 127

List of Abbreviations

Abbreviation	Meaning
SIT	Self-induced transparency
ARP	Adiabatic rapid passage
CPT	Complete population transfer
SVEA	Slowly varying Envelope Approximation
RWA	Rotating Wave Approximation
FDTD	Finite Difference Time Domain
NLSE	Nonlinear Schrödinger Equation
FWHM	Full-width half-maximum
QED	Quantum electro-dynamics
FROG	Frequency-resolved optical gating
ADE	Auxiliary differential equation
TFSF	Total-field scattered-field
PML	Perfectly matched layer

List of Figures

2.1 Schematic of slab waveguide 26
2.2 Fundamental mode of symmetric slab waveguide 30
2.3 Fundamental mode of slot waveguide 31
2.4 Dispersions of slab and slot waveguides 32

3.1 Three level configurations 43
3.2 Adiabatic states during chirped pulse excitation 47
3.3 Illustration of 2π-pulse 53

4.1 V-type and Λ-type three-level systems 57
4.2 Collision of simultons with parallel polarisations 60
4.3 Group velocity dependence of simulton collisions with parallel polarisation 61
4.4 Coherences during orthogonally polarised simulton collisions 62
4.5 Ground-state occupation maps of simulton collisions with orthogonal polarisation 65
4.6 Group velocity dependence for collisions of orthogonally polarised simultons 67
4.7 Simulton collision in the presence of dephasing 68
4.8 Polarisation-angle dependent group velocities after simulton collisions . . 70

5.1 Adiabatic rapid passage in full time-domain 77
5.2 Inversion in two-level system after excitation by pulses with varying chirp and area 78
5.3 FROG traces for moderately chirped pulses in absorbing medium 80
5.4 Envelopes and spectra of moderately chirped pulses in absorbing medium 81
5.5 Inversion left in absorbing medium by strongly chirped pulses 83

5.6 Evolution of spectrum of strongly chirped pulse in absorbing medium . . 83
5.7 Final pulse envelopes and spectra for strongly chirped pulse in absorbing medium 84
5.8 Frog traces of strongly chirped pulses after propagation through absorbing medium 86

6.1 Polarisation and effective saturation coefficient for fibre with saturable nonlinearity 92
6.2 Nonlinear phase shift of fibre with saturable nonlinearity 93
6.3 Inversion profile of 2π-pulse in slab waveguide 96
6.4 Pulse envelopes and spectra of 2π-pulse in slab waveguide 97
6.5 Evolution of 2π-pulse in slab waveguide 98
6.6 Train of 2π-pulses in slot waveguide 101
6.7 2π-pulse propagation characteristics in slot waveguide 103
6.8 Spectra and envelopes of 2π-pulses in slot waveguide 104
6.9 FROG traces of 2π-pulses in slot waveguide 105
6.10 Group velocity of 2π-pulses in slot waveguide 106
6.11 4π-pulse break up in slot waveguide 107
6.12 Spectra and envelopes of 4π-pulses in slot waveguide 107
6.13 Inversion after collisions of two-level solitons in slot waveguide 109
6.14 Electric field after collisions of two-level solitons in slot waveguide 110
6.15 Inversion after collisions of simultons in slot waveguide 111
6.16 Electric field after collisions of simultons in slot waveguide 111
6.17 Population and polarisation snapshots for memory scheme investigated in slot waveguide 113

Chapter 1

Introduction

1.1 Background and motivation

In 1865 James Clerk Maxwell published his famous set of equations [1] unveiling the link between electric and magnetic phenomena and the electromagnetic nature of light, thereby also confirming Huygens' findings that light can be described as a wave. One of the consequences of the wave nature of light is the superposition principle; different light fields interfere to produce troughs and crests in the intensity, but they do not directly influence each other's propagation behaviour. When describing light in the complementary picture – as photons – the superposition principle can be understood as a lack of interaction between two photons. Maxwell's equations also tell us, however, that light propagation through matter is determined by the so-called permittivity ϵ and permeability μ of the medium. If, now, one light field (or a collection of photons) interacting with the medium is able to change its permittivity or permeability it can indirectly interact with other light fields (or photons).

A first hint at this possibility was provided with John Kerr's experiments, published in 1875 [2, 3]. He applied an electric field to a glass plate and thus changed its optical properties, notably its refractive index $n = \sqrt{\epsilon\mu}$. This change turned out to be proportional to the square of the electric field strength. As light consists of electric and magnetic field components, it is evident that light should also, in principle, be capable of inducing a refractive index change proportional to its intensity, the AC Kerr effect. At the end of the 19th century, however, no light fields intense enough to produce measurable effects were available.

This changed in 1960 with the invention of the laser [4, 5], capable of producing intense, coherent light fields by exploiting stimulated emission in a pumped gain material, leading to the creation of a new sub-field of physics called nonlinear optics. It did not take long for fundamental effects such as second-harmonic generation [6], third-harmonic generation [7] and wave mixing [8, 9] to be discovered. The use of pulsed lasers and gas cells allowed for the discovery of another striking effect of nonlinear optics termed self-induced transparency (SIT) [10], setting off an astonishing number of experimental and theoretical research activities (see [11–13] and References therein) in the years to follow. In linear optics, i.e. for small pulse intensities, light travelling through a medium, which exhibits an electric dipole transition resonating with the light's frequency, is absorbed and its energy decreases exponentially with propagation distance. This is known as Lambert-Beer's Law and is regularly exploited to measure concentrations of substances, especially in analytic chemistry. McCall and Hahn [10], however, found that intense light pulses, which are much shorter than the relaxation times in the medium and obey the so-called area theorem – a relation between pulse amplitude and duration – can traverse an absorbing medium without losing energy. In essence, the first part of the pulse inverts the electronic population of the absorbing transition while the second part of the pulse harnesses this inversion in the form of stimulated emission. As a result, no light energy is lost to the medium and the pulse is slowed down due to the reshuffling of light from the leading edge to the trailing edge.

Mathematically, the propagation of intense light fields through resonant absorbers is described by the Maxwell-Bloch equations; a system of nonlinear partial differential equations for which an analytic solution can be found provided a number of assumptions are made [14]. Some of the early efforts towards a complete theoretical understanding of SIT were aimed at reducing the approximations while still being able to find analytical solutions and also to find additional solutions to the original SIT equations formulated in [10]. These efforts were greatly helped by a parallel development in the mathematics of nonlinear differential equations, which was initially motivated by the search of analytic solutions to nonlinear differential equations stemming from the physics of water waves. In 1895 Korteweg and de Vries [15] discovered that the motion of water waves in shallow canals could be described by a nonlinear differential equation, which is now known as Korteweg de Vries equation. By finding a stable solution to this equation they were able

to explain the phenomena of solitary waves originally observed by John Scott Russell in 1834 [16].

In the year of the discovery of SIT, Gardner *et.al.* [17] developed the inverse scattering transform method with which it became possible to systematically identify exactly solvable nonlinear differential equations and their stable solutions, which by then where called solitons [18]. This method was subsequently applied to other nonlinear differential equations, one of them the sine-Gordon equation, onto which the Maxwell-Bloch equations could be mapped [19, 20], allowing for a more systematic analysis of the possible SIT solutions. Another example of exactly solvable nonlinear equations providing the basis for optical solitons is the nonlinear Schrödinger equation (NLSE) that, as it turns out [21, 22], describes pulse propagation in waveguides exhibiting a Kerr nonlinearity and contains bright [21] and dark [22] soliton solutions.

The initial theoretical description of SIT assumed plane-wave propagation in one direction only. Early efforts to improve on this approximation to describe real wave-fronts were unfruitful since only some general trends such as tendencies for filamentation, break-up or self-focusing could be formulated [14]. In 2000 [23] a free-space solitary solution of the Maxwell-Bloch equations – a so-called light bullet [24, 25] – was found, but it has not yet been realised experimentally. To enable diffraction-free SIT solitons a promising approach is to employ waveguides, which provide a restriction to only one propagation direction but introduce a mode profile and dispersion. By ignoring the problem of dispersion it was possible to formulate a theory for pulse propagation in waveguides with an infinitely thin, resonantly absorbing layer [26, 27]. Ignoring, on the other hand, the problems posed by a fixed pulse profile generating an inhomogeneous profile of Rabi frequencies, it was possible to find soliton solutions to pulse propagation in waveguides comprising both a Kerr nonlinearity and resonant absorbers. In a first treatment [28] the conditions on the soliton where formulated such that the Kerr effect had to compensate for the dispersion whereas the SIT effect would provide a pulse slowdown. The conditions on the material parameters to ensure a simultaneous fundamental Kerr and SIT soliton are, however, prohibitive for the common erbium doped fibres. In the experimental realisation [29] of SIT in waveguides the self-phase modulation due to the Kerr effect was much bigger than the phase-change due to the dispersion of the waveguide and the resultant pulses are not combined Kerr and SIT solitary waves. Chi

et.al [30] questioned that the dispersion of the resonant absorbers could just be discarded and found, by employing a peculiar approximation that mixes the rotating wave approximation with a treatment of the full Maxwell-Bloch equations, that SIT could provide a negative dispersion to counteract the self-phase modulation of the Kerr effect. Later, Porsezian and Nakkeeran found a soliton solution to a propagation equation that also accounted for Raman effects and higher order nonlinearities [31]. This propagation equation presupposed, however, a specific relation between dipole strength of the absorber and Kerr nonlinearity in the waveguide. Thus, these works did not answer the question whether a SIT soliton in dispersive waveguides is also possible for arbitrary relations between Kerr coefficient and absorber coupling strength.

Another direction of research considered the effects of additional electronic levels on the propagation properties of the pulses. Konopnicki and Eberly [32] analysed SIT in three-level systems and showed that solitons acting on both transitions of the three-level system simultaneously (simultons) are possible albeit with some conditions on the electronic system. For a cascade system the electronic population has to be prepared appropriately, whereas Λ- and V-type systems require equal oscillator strengths to experience simulton propagation. When a Λ-type system has two different transition frequencies and oscillator strengths, in contrast, a 2π-pulse on the higher-frequency transition is unstable and acts as parametric amplifier for pulses resonant with the other transition [33]. For V-type systems with equal oscillator strengths a pulse area theorem has been found [34] that applies to the sum of the areas of the constituent parts of the simulton and is otherwise identical to the original pulse area theorem for two-level systems.

In recent years the focus of the research on SIT has shifted from analytical studies about mathematically strict soliton solutions to numerical studies of problems without analytical solutions. For example some studies investigated the collisions of counter-propagating pulses [35, 36] that lead to a loss of energy in the pulse due to the creation of a population grating in the interaction region if the number density of photons is higher than the number density of atoms and to a pulse breakup otherwise [36]. Furthermore, the availability of ever shorter pulses [37] and greater computational power has led to SIT being studied increasingly without applying slowly varying envelope or rotating wave approximations [38–40], which become invalid for very short pulses. It turned out, however, that differences to the more approximate theory occur only if the

pulses are shorter than an optical cycle [40] or very intense (areas of several π) and in the few-cycle regime [39]. In this regime of broadband pulses of high intensity ionisation and high harmonic generation occurs [41], rendering it non-physical to model the light-matter interaction by two-level systems. Thus the area theorem remains accurate for all realistic cases of the interaction between a two-level system and a coherent light pulse.

Perhaps the most useful aspect of SIT in recent years has, however, been its suitability as a test of numerical simulation codes incorporating the Maxwell-Bloch equations, since SIT provides analytic solutions to the associated nonlinear differential equations. It is because of this aspect of SIT that I came across it at first. While testing different simulation setups for three-level Maxwell-Bloch equations I encountered the phenomenon of soliton birth that will be discussed in Chapter 4 and that led me to search for physical systems, which could provide a robust and compact experimental realisation of SIT. Having such a realisation one could think of employing SIT solitons in optical computing schemes to slow down or store information entering the medium in the form of a light pulse [42, 43], or to engineer optical gates built upon the light-light interactions taking place between SIT solitons [35, 44, 45] because the superposition principle does not hold any more in nonlinear media.

A compact realisation of SIT relies on the existence of waveguides that confine light to small mode areas. As will be explained in this thesis it also relies on the possibility of almost constant mode profiles over an area of the waveguide where most of the electric field is confined. The emergence of nano-fabrication techniques has enabled the creation of waveguides with nanoscopic low-index gaps with greatly enhanced electric fields [46–48]. Not only do those waveguides allow for greatly enhanced nonlinear interactions [49], but they also provide a very flat mode profile of the electric field in the gap. Hence, it is those nanophotonic structures, which are identified as candidates for the realisation of compact SIT solitons in waveguide and found to be ideally suited [50].

1.2 Structure of the thesis

The focus of this thesis lies on the analysis of the propagation of intense light pulses through matter. Hence, it is paramount to understand, first, light propagation in general

and then the interaction between light and matter. Chapter 2 first brings the fundamental equations governing the propagation of light, i.e. Maxwell's equations into context. Applying these equations to structured matter with different dielectric constants in different areas, the principles of waveguiding are explained and linear (low-intensity) light propagation characteristics in the waveguiding structures employed in Chapter 6 are calculated. Next, the phenomenon of temporal optical solitons, stable, intense pulses in nonlinear waveguides, is discussed. In this context the mathematical foundation of analytical soliton theory, the method of the inverse scattering transform, is introduced to provide an understanding for pulse propagation in waveguides with a Kerr nonlinearity in particular and solitons in general.

The subsequent Chapter (Chapter 3) discusses the fundamentals of the resonant interaction of light with electronic matter. If a light field is resonant with the energy difference of electronic states, in, e.g., an atom or molecule, that have a different electric dipole moment, it can induce a electric dipole transition of the electronic configuration from one state to the other. The dynamics of this transition can be described by the Maxwell-Bloch equations, which are introduced in the first Section of Chapter 3. Section 3.2 explains the phenomenon of adiabatic population transfer of the electronic population of an atom from ground- to excited states using the Maxwell-Bloch equations previously introduced. This phenomenon plays an important role in the interaction of chirped pulses with a dense two-level medium studied in Chapter 5. In Section 3.3 the focal point of this thesis, self-induced transparency of an intense, coherent pulse in a resonantly absorbing medium, is discussed and derived from the Maxwell-Bloch equations.

The first results of this thesis are presented in Chapter 4, where the collision of counterpropagating simultons (SIT solitons in three-level systems) is investigated in a plane-wave approximation. While collision studies have previously been performed for a two-level medium [35, 36, 51], where a population grating is excited by the collision. Here, a V-type three-level medium with degenerate upper levels is studied, a situation often encountered in atomic transitions. The additional upper level provides a further degree of freedom in the collision parameters and introduces a cross-polarisation. This allows for additional effects in the interaction. Indeed, it is found that, dependent on the relative polarisation of the light pulses, either a population grating is created as in the two-level collisions or additional solitary waves can be created for high-enough group

velocities. This parameter-dependent soliton birth may be envisioned as the crucial light-light interaction for optical computing schemes if it could be realised in a compact geometry. However, such a realisation of SIT solitons is still to be proven experimentally.

In the next Chapter (Chapter 5) we investigate, still in the plane-wave approximation, the propagation of chirped pulses through a resonantly absorbing two-level medium. Chirped pulses are, for example, created when a transform-limited pulse propagates through a dispersive waveguide. For the understanding of pulse propagation through waveguides it is thus important to understand how dispersion (that has accumulated as chirp) influences the pulse's evolution in a resonant medium. If the chirp is lost in propagation, it is likely that dispersion can also be compensated directly. Indeed, we find that moderately chirped pulses reshape into unchirped solitary waves upon propagation through the absorber although some absorption happens at the entrance into the medium. The origin of this initial absorption can be understood by comparing the pulse parameters to the conditions of adiabatic rapid passage [52]. This comparison also suggests to look at chirped pulse propagation from another perspective, namely from the perspective of optimising the inversion in the initially absorbing medium. Using strongly chirped pulses, capable of completely transferring the population of sparse ensembles of absorbers, one could hope to also invert a large proportion of the denser medium by using even higher pulse intensities. However, in [53, 54] it was shown that this tactic is likely to fail. As we discuss in Section 5.4, this is because pulses capable of adiabatic rapid passage in sparse ensembles get quickly reshaped into transparent pulses in a dense ensemble of absorbers. Additional light intensity is transformed into solitary waves instead of inverting more of the absorbers. Thus, the dynamical reshaping process associated with self-induced transparency solitons fundamentally limits the achievable inversion in a dense ensemble of absorbers by coherent pumping with a chirped pulse.

Chapter 6 studies SIT solitons in nanophotonic waveguides. Since a waveguide restricts propagation to one dimension, nonlinear light propagation in waveguides is usually described with one-dimensional equations. Effects, such as dispersion and nonlinearities are expanded in Taylor series in time and electric field order, respectively, and the expansion coefficients are calculated from the mode profile at the center frequency of the pulse in linear approximation. For short pulses the approximation of a mode profile that does not change significantly with frequency may break down [55]. Conversely,

nonlinearities may saturate for intense pulses and as is shown in Section 6.1 the definition of effective nonlinearities then becomes an approximation. In the case of SIT, saturation is an integral part of the process and it leads to erroneous conclusions to resort to one-dimensional propagation equations unless the mode profile is flat over the region containing the resonant nonlinearities (demonstrated in [50]). Integrating the two-dimensional Maxwell-Bloch equations in a nanophotonic gap waveguide [46] it is shown in Section 6.2 that SIT becomes possible in such a compact geometry. If the absorber density is high enough to induce significant changes in the group velocity, 2π-pulses stay stable and effectively become solitary waves. Further Sections (6.3 and 6.4) investigate whether parameter-dependent soliton birth and optical memory schemes that have been discovered in a plane-wave approximation also exist in SIT of resonantly absorbing waveguides. The result suggests, that SIT in nano-gap waveguides is, apart from the modification of the group velocity due to waveguide dispersion, the same as SIT in the plane-wave approximation, as long as the absorber densities are high enough to have an appreciable impact on the group velocity of the pulses, i.e. an appreciable part of the pulse energy has to always be stored in the absorbing system. General conclusions of the presented studies are drawn in Section 6.5, while, finally, an outlook onto possible future research directions, building on the work performed in the context of this thesis, is given in Chapter 7.

To summarise, in this thesis the phenomenon of polarisation- and group velocity-dependent soliton birth in the collision of counterpropagating simultons is discovered [45]. Furthermore, a dynamic transition between adiabatic rapid passage and self-induced transparency is unveiled that consists of a reshaping of chirped pulses into unchirped pulses obeying the area theorem in a resonant absorber [56]. Finally, a compact realisation of SIT in nanophotonic gap waveguides is proposed [50] that could allow for an experimental exploitation of SIT effects such as a slow-down of light pulses, the afore-mentioned pulse collisions of simultons [45] or optical memories [42, 43].

Chapter 2

Light propagation

Optical solitons are a phenomenon of nonlinear light propagation through matter. If we want to understand optical solitons we therefore have to understand the rules of light propagation and light-matter interaction. In this chapter we focus on the effect matter has on light and disregard the effects of light on matter, apart from a possible change in refractive index. First we discuss (Sec. 2.1) the laws governing the dynamics of electromagnetic fields that give rise to light waves, i.e. Maxwell's equations. Maxwell's equations represent the influence of matter on a light field in terms of charges, currents and polarisations that can often be replaced by an effective refractive index that depends only on the frequency of the light field.

Using macroscopic Maxwell's equations the propagation of light in structured dielectric materials can be understood in terms of waveguiding. Waveguides are important tools in optical communications and most temporal optical solitons are realised in waveguiding structures. The fundamentals of waveguides are introduced in Sec. 2.2. In Sec. 2.3, we show how the Kerr effect - an intensity dependent refractive index - can give rise to optical solitons. Optical solitons are stable, dynamically unchanging solutions of nonlinear light propagation equations and Kerr solitons are their most prominent example. This last section is intended to provide an insight into fundamental properties of solitons, the SIT solitons this thesis is mainly concerned with are introduced in the following chapter.

2.1 The electromagnetic field

Quantum electro-dynamics (QED), the fundamental theory of light-matter interaction, introduces light in terms of photons, discrete units of light with an energy that is given by the light frequency ω multiplied by Planck's constant $\hbar$, the fundamental quantum mechanical unit of angular momentum; i.e. $E_{\mathrm{ph}} = \hbar\omega$. A sharply defined light frequency or equivalently a sharply defined photon energy only arises when an infinitely extended photon is considered. Despite this obvious idealisation these so-called free-space modes of the light field form a complete mathematical basis to describe real photons in vacuum. Using the principle of superposition any real, partially localised and multi-frequency, state of light can be expressed in the basis of free-space modes. Since photons do not directly interact with each other the principle of superposition is always applicable for a light field in vacuum. Sometimes the idealisation of a perfect cavity that traps light in a certain region of space is more appropriate to describe light fields. In so-called cavity-QED [57] the possible frequencies of light become discretised, the light field is partially localised and matter is implicitly assumed to be present in the form of a cavity.

When charged matter in form of electrons and protons is introduced into QED things quickly become much more complicated and only very few problems, such as the interaction between a monochromatic (single-frequency) light field and a single two-level atom can be calculated precisely [58]. Fortunately, a lot of relevant problems in light-matter interaction can be calculated within Maxwell's equations, the classical limit of QED, i.e. the limit of $\hbar \to 0$. As long as the light field is assumed to be coherent, a very good approximation for most laser generated fields although not for daylight, Maxwell's equations describe all phenomena but those associated with shot-noise.

The macroscopic Maxwell's equations for electric and magnetic fields in real space coordinates $\mathbf{r}$ are given by

$$\nabla \cdot \mathbf{D}(\mathbf{r},t) = \rho(\mathbf{r},t) \tag{2.1}$$

$$\nabla \cdot \mathbf{B}(\mathbf{r},t) = 0 \tag{2.2}$$

$$\nabla \times \mathbf{E}(\mathbf{r},t) = -\partial_t \mathbf{B}(\mathbf{r},t) \tag{2.3}$$

$$\nabla \times \mathbf{H}(\mathbf{r},t) = \partial_t \mathbf{D}(\mathbf{r},t) + \mathbf{J}(\mathbf{r},t)\,, \tag{2.4}$$

with the constitutive relations between the electric field $\mathbf{E}(\mathbf{r},t)$ and the dielectric displacement $\mathbf{D}(\mathbf{r},t)$

$$\mathbf{D}(\mathbf{r},t) = \epsilon_0\epsilon_b(\mathbf{r})\mathbf{E}(\mathbf{r},t) + \mathbf{P}(\mathbf{r},t)\,, \tag{2.5}$$

and between the magnetic induction $\mathbf{B}(\mathbf{r},t)$ and the magnetic field $\mathbf{H}(\mathbf{r},t)$

$$\mathbf{H}(\mathbf{r},t) = \frac{1}{\mu_0}\mathbf{B}(\mathbf{r},t) - \mathbf{M}(\mathbf{r},t)\,. \tag{2.6}$$

The response of a medium without free charges ρ or free currents $\mathbf{J}$ to a light field is contained in the electric polarisation $\mathbf{P}$ and the magnetic polarisation $\mathbf{M}$. All materials we will be dealing with are non-magnetic so that $\mathbf{H} = \mathbf{B}/\mu_0$. For the purposes of the studies presented here, the electric polarisation $\mathbf{P}(\mathbf{r},t)$ is divided into a static, linear part subsumed in the background permittivity $\epsilon_b(\mathbf{r})$ and a dynamic response, time- and amplitude dependent, that is calculated from partial differential equations, which are external to Maxwell's equations.

The finite-difference time-domain method (detailed in Appendix A) for the calculation of electric and magnetic fields employed throughout this thesis directly calculates Maxwell's curl equations and the features described by the wave equations emerge as a consequence. Maxwell's equations always need to be supplemented with appropriate boundary conditions to calculate a specific physical problem. In our case the boundary conditions are provided by absorbing boundary conditions in space (see A.5) and additionally a time series of incident electric and magnetic fields onto the simulation domain. To this end, the total-field/scattered field method (described in A.4) is used.

2.2 Waveguides

A waveguide consists of dielectric layers with differing refractive indices, the simplest geometry being the slab waveguide (see Figure 2.1) with a layer of high refractive index n_f sandwiched between two layers of low refractive indices $n_s < n_f$ of the substrate and $n_c \leq n_s$ of the cover [59, 60]. For slab waveguides it is assumed that these layers extend infinitely in the $y-z$-plane. The most intuitive explanation of waveguides makes use of the ray picture of light propagation and Snell's laws of refraction. A light ray that is uniform in the y-direction and propagates in the z-direction will be confined to the

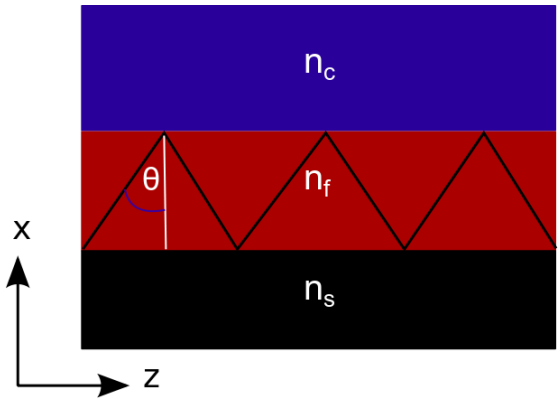


Figure 2.1: Schematic of a slab waveguide with a film of height h and refractive index n_f sandwiched between a substrate of index n_s and cover of index n_c. The angle θ denotes the angle between wavevector and waveguide normal x.

film layer with the high index n_f, if its angle of incidence θ upon the substrate is larger than the angle of total internal reflection θ_c given by $\sin(\theta_c) = n_s/n_f$. Hence, light will be guided inside the film layer if the angle of incidence into the waveguide is larger than the angle of total internal reflection.

In the ray picture, one can also calculate the number of guided modes and their respective phase velocities, if the rays are assumed to be the wave-normals of two superimposed plane-waves following a zig-zag path along the waveguide [59] (see Fig. 2.1). The phase velocities v_{ph} of the allowed modes are calculated from the corresponding angles of propagation θ as

$$v_{\mathrm{ph}} = \frac{\omega}{\beta} = \frac{c}{n_f \sin(\theta)}\,, \tag{2.7}$$

where β is the propagation constant of the mode. To find the allowed modes one has to calculate the angle- and polarisation-dependent phase shifts ϕ_c and ϕ_s experienced by the rays upon reflection from cover and substrate by using the Fresnel formulas [59]. The condition for a guided mode to occur at angle θ is, that the phase shifts incurred upon going from cover to substrate and back to the substrate have to add up to a multiple of 2π. This results in the transverse resonance condition

$$2kn_f h\cos(\theta) - 2\phi_c - 2\phi_s = 2\nu\pi\,, \tag{2.8}$$

where $k = \omega/c$ is the magnitude of the wavevector of the light of frequency ω, h is the height of the high-index film and ν is the mode number. Condition (2.8) determines the

dispersion of the waveguide modes, i.e. the dependence of the propagation constant β on frequency. The propagation constant determines the phase velocity of light, whereas its derivative with respect to frequency determines the group velocity of a pulse propagating through the waveguide. If group velocity dispersion is present, i.e. if the group velocity depends on frequency, the different frequency components in a pulse propagate with different speeds and thus the pulse becomes chirped and its duration increases.

For each mode there exists a cut-off frequency below which the mode does not exist. In the case of a symmetric guide ($n_s = n_c$) the cut-off of the fundamental mode is at $\omega = 0$, meaning that there always is at least one allowed propagation mode. Below the cut-off frequency of mode $\nu = 1$ the waveguide is a single-mode waveguide as only the fundamental guided mode exists. The number of guided modes in the waveguide can be approximately calculated as [59]

$$\nu = \frac{2h}{\lambda}\sqrt{n_f^2 - n_s^2}\,. \tag{2.9}$$

As we have seen, it is possible to obtain many important results about light propagation in waveguides by using the ray picture of light. If, however, one is interested in the electric and magnetic field distributions in the waveguides, the electromagnetic theory of waveguides has to be employed, which builds directly on Maxwell's equations for source-free fields.

$$\begin{aligned} \nabla \times \hat{\mathbf{E}}(t) &= -\frac{\partial \hat{\mathbf{B}}(t)}{\partial t} \\ \nabla \times \hat{\mathbf{H}}(t) &= \frac{\partial \hat{\mathbf{D}}(t)}{\partial t}\,. \end{aligned} \tag{2.10}$$

Since waveguide modes are defined for a specific frequency of light a periodic time dependence of electric and magnetic fields is assumed

$$\hat{\mathbf{E}}(t) = \mathbf{E}\exp\left(-i\omega t\right) + \mathbf{E}^*\exp\left(i\omega t\right). \tag{2.11}$$

Additionally, we treat the material constituting the waveguides as linear, homogeneous and isotropic dielectrics with constitutive relations

$$\mathbf{D}(\omega) = \epsilon(\omega)\mathbf{E}(\omega)\ ;\ \mathbf{B}(\omega) = \mu\mathbf{H}(\omega)\,, \tag{2.12}$$

which results in the frequency dependent Maxwell's equations

$$\begin{aligned} \nabla \times \mathbf{E} &= -i\omega\mu\mathbf{H} \\ \nabla \times \mathbf{H} &= i\omega\epsilon\mathbf{E}\,. \end{aligned} \tag{2.13}$$

The important missing ingredient for the calculation of waveguide modes are the boundary conditions on these equations at the surface between media of dielectric indices ϵ_1 and ϵ_2. Those are given by

$$\begin{aligned} \mathbf{e}_n \cdot (\mathbf{B}_1 - \mathbf{B}_2) &= 0 \\ \mathbf{e}_n \cdot (\mathbf{D}_1 - \mathbf{D}_2) &= 0 \\ \mathbf{e}_n \times (\mathbf{H}_1 - \mathbf{H}_2) &= 0 \\ \mathbf{e}_n \times (\mathbf{E}_1 - \mathbf{E}_2) &= 0\,, \end{aligned} \tag{2.14}$$

where $\mathbf{e}_n$ is a unit vector normal to the interface. All media discussed here have a magnetic permeability of $\mu = \mu_0$, so that $\mathbf{H}_1 = \mathbf{H}_2$ at the surface.

For the calculation of waveguide modes it is convenient to separate electric and magnetic fields into longitudinal fields (fields pointing in propagation direction, usually chosen as the z-direction) and transverse fields (fields orthogonal to the propagation direction). Using this separation different mode types can be defined, depending on whether both, one, or none of the fields consist only of transverse fields. If longitudinal components of electric and magnetic fields are zero the mode is called a TEM mode, if the longitudinal electric field component is zero one has a TE mode, and if the longitudinal magnetic field component is zero one has a TM mode.

In Chapter 6 the fundamental TM mode of the symmetric planar slab waveguide will be used for numerical simulations of pulse propagation in resonant waveguides. Let us now calculate the field profile of this mode in order to illustrate a mode calculation and to be able to refer to the profile later. For TM modes Maxwell's equations can be simplified considerably by setting $H_x = H_z = 0$ and $E_y = 0$. Also, in a planar slab waveguide that is infinitely extended in y-direction, all partial derivatives in y-direction vanish ($\partial_y = 0$), if the fields are assumed to also be infinitely extended and homogeneous.

Thus equations (2.13) reduce to

$$\begin{aligned} \partial_z E_x - \partial_x E_z &= -i\omega\mu H_y \\ -\partial_z H_y &= i\omega\epsilon E_x \\ \partial_x H_y &= i\omega\epsilon E_z \,, \end{aligned} \tag{2.15}$$

where we can replace the partial derivative in z-direction with the mode propagation constant β

$$\begin{aligned} i\beta E_x + \partial_x E_z &= i\omega\mu H_y \\ \beta H_y &= \omega\epsilon E_x \\ \partial_x H_y &= i\omega\epsilon E_z \,. \end{aligned} \tag{2.16}$$

Above equations result in a wave equation for the magnetic field component H_y given by

$$n^2(x)\partial_x\left(\frac{1}{n^2}\partial_x H_y\right) = (\beta^2 - n^2(x)k)H_y \,. \tag{2.17}$$

Additionally, the boundary conditions (2.14) on the TM mode of a symmetric slab waveguide with film height h and $n_c = n_s$ can be written as

$$\begin{aligned} E_x(x = h - \delta, z) &= \frac{n_c^2}{n_f^2} E_x(x = h + \delta, z) \\ E_z(x = h - \delta, z) &= E_z(x = h + \delta, z) \,, \end{aligned} \tag{2.18}$$

with $\delta > 0$ an infinitesimal displacement from the boundary, for the positive-x boundary. Conditions for the boundary at $x = 0$ are analogous.

To calculate the magnetic field distribution assuming homogeneous dielectric layers one makes the following Ansatz for the magnetic field [59]

$$H_y = \begin{cases} H_c \exp\left[-\gamma_c(x - h)\right], & x > h \\ H_f \cos\left(\kappa_f(x - h/2) - \Phi_c\right), & 0 \le x \le h \\ H_c \exp\left[\gamma_c x\right] & x < 0 \,, \end{cases} \tag{2.19}$$

which comprises exponentially decaying fields in the cladding and standing waves in

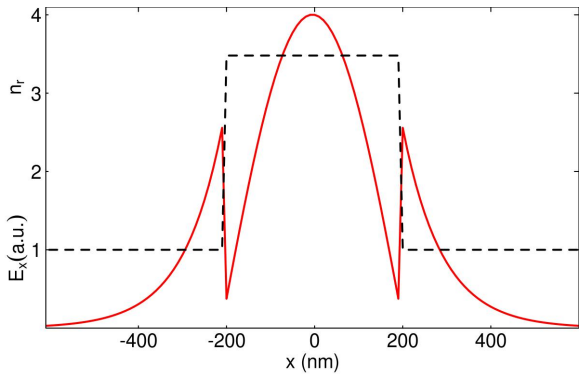


Figure 2.2: E_x profile (solid red line) of the fundamental TM mode and refractive index n_r (dashed black line) of the symmetric slab waveguide with a width of $h = 400\,\text{nm}$ at a wavelength of $\lambda = 1550\,\text{nm}$.

the high-index film. Herein, $\gamma_c^2 = \beta^2 - n_c^2 k^2$ is the decay constant in the cladding, $\kappa_f^2 = n_f^2 k^2 - \beta^2$ is the propagation constant in the high-index film, while boundary conditions provide $\tan(\Phi_c) = (n_f/n_c)^2 \gamma_c/\kappa_f$ and the dispersion relation $\kappa_f h - 2\Phi_c = 0$. Finally, a relation for the peak fields is obtained as $H_f^2(n_f^2 - n_{\text{eff}}^2)/n_f^2 = H_c^2(n_f^2 - n_c^2)q_c/n_c^2$ with $q_c = (n_{\text{eff}}^2/n_f)^2 + (n_{\text{eff}}^2/n_c)^2 - 1$. These relations quantify the mode profile uniquely and the result for the E_x-field is plotted in Figure 2.2.

Recently waveguides have emerged which are structured on the nanoscale [61, 62]. These waveguides can exhibit unusual properties, such as photonic bandgaps in so-called photonic crystals [63, 64] or high field enhancements [46–48, 65]. High field enhancements allow for strong nonlinearities with comparatively low pulse energies [66, 67] and for a confinement of the electric field to sub-wavelength mode areas. The most important property of these waveguides for the purpose of the present work, however, is the profile of its fundamental mode, which can exhibit a region of almost constant and very high electric fields. For a slab-based (infinitely extended) slot waveguide, the profile of the fundamental symmetric mode is given analytically as [46]

$$E_x = A \begin{cases} \frac{1}{n_s^2}\cosh(\gamma_s x)\,, & |x| > a \\ \frac{1}{n_h^2}\cosh(\gamma_s x)\cos[\kappa_h(|x|-a)] + \frac{\gamma_s}{n_s^2\kappa_h}\sinh[\kappa_h(|x|-a)]\,, & a < |x| < b \\ \frac{1}{n_c^2}\{\cosh(\gamma_s x)\cos[\kappa_h(b-a)] & \\ +\frac{n_h^2\gamma_s}{n_s^2\kappa_h}\sinh(\gamma_s x)\sin[\kappa_h(b-a)]\}\cdot\exp[-\gamma_c(|x|-b)]\,, & |x| < b \end{cases} \tag{2.20}$$

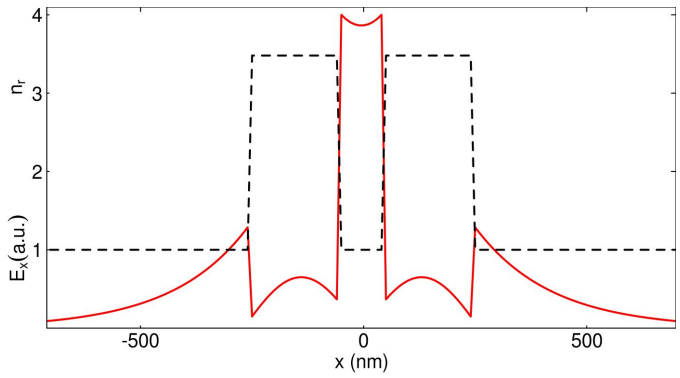


Figure 2.3: E_x profile (solid red line) of the fundamental TM mode and refractive index n_r (dashed black line) of the symmetric slab-based slot waveguide with a slot width of $w = 100\,\text{nm}$ at a wavelength of $\lambda = 1550\,\text{nm}$.

with κ_h as the transverse wave number in the high index slabs and γ_c (γ_s) the field decay coefficient in the cladding (slot), n_c and n_s the refractive indices of cladding and slot and n_h the refractive index of the high index slab. The electric field and refractive index profiles of the slot waveguide used in Chapter 6 are depicted in Fig. 2.3. The constant A depends on the transverse wavevector κ_h, the refractive index of the slabs n_h and the free-space propagation constant $k_0 = 2\pi/\lambda_0$ as

$$A = A_0 \frac{\sqrt{k_0^2 n_h^2 - \kappa_h^2}}{k_0}\,. \tag{2.21}$$

Determining relations for κ_h, γ_s and γ_c are given by

$$k_0 n_h^2 - \kappa h^2 = k_0 n_c^2 + \gamma_c^2 = k_0^2 n_s^2 \gamma_s^2 = \beta^2\,. \tag{2.22}$$

Here, β is the eigenmode propagation constant, which can be found from the transcendental equation

$$\tan\left[\kappa_h(b-a) - \arctan\left(\frac{\gamma_c n_h^2}{\kappa_c n_c^2}\right)\right] = \frac{\gamma_s n_h^2}{\kappa_h n_s^2}\tanh\left(\gamma_s a\right). \tag{2.23}$$

The propagation constant $\beta = \omega/c n_{\text{eff}}$, and consequently the effective refractive index n_{eff}, of a waveguide vary with the wavelength of the applied light field. The dependency of effective index on wavelength is the dispersion-relation and it determines the propagation behaviour of a light pulse inside the waveguide. The phase velocity of light is given

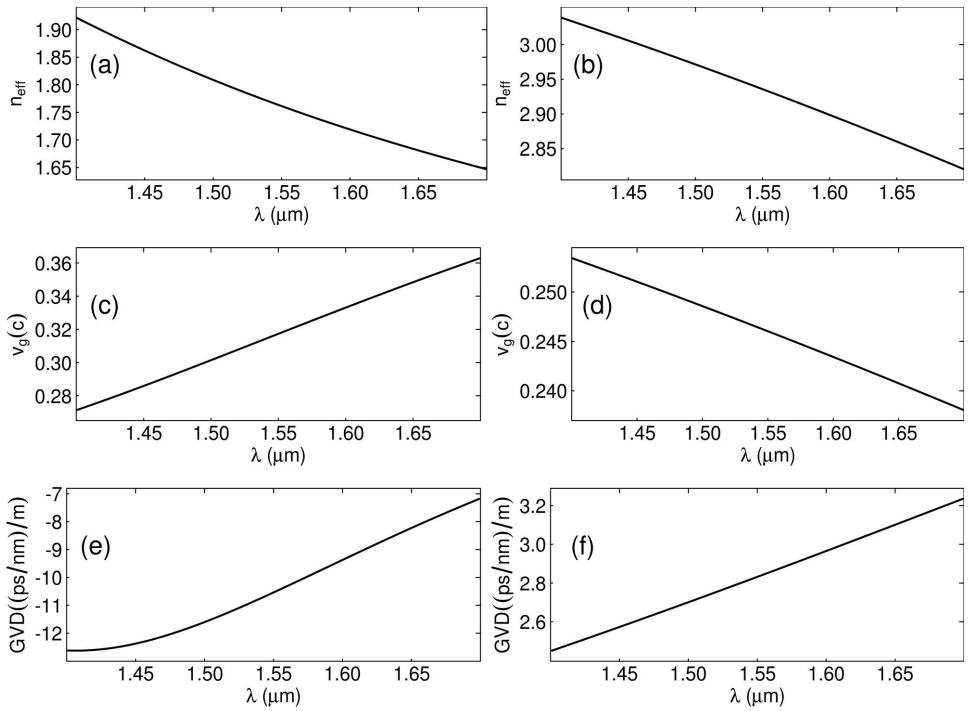


Figure 2.4: Wavelength dependence of (a)-(b) effective refractive index, (c)-(d) group velocity and (e)-(f) group velocity dispersion of $2D$ slot waveguide and slab waveguide respectively.

by $v_p = c/n_{\text{eff}}$, while the group velocity of a pulse is $v_g = c/(n_{\text{eff}} - \lambda \partial n_{\text{eff}}/\partial\lambda)$. Evidently, the group velocity is also a function of the wavelength, thus leading to a spreading of short pulses during propagation because of their broad frequency content. To first order this effect is quantified by the group velocity dispersion given as $D = -\frac{\lambda}{c}\frac{\partial^2 n_{\text{eff}}}{\partial\lambda^2}$. Effective refractive index, group velocity and group velocity dispersion are shown in Figure 2.4 for the planar slab and planar slot waveguides discussed here. Note that the intrinsic dispersions of the dielectric materials comprising the waveguide are ignored in these plots.

For high light intensities the propagation in the dielectric media comprising the waveguides becomes nonlinear and the propagation behaviour changes. Now it becomes possible that the nonlinearity counteracts the waveguide dispersion and the pulses stay stable. Stable pulses following a nonlinear propagation equation are called solitons and the canonical example of optical solitons, Kerr solitons obeying the nonlinear Schrödinger equation, is discussed in the following section.

2.3 Optical solitons

Optical solitons based on the Kerr effect were first proposed by Hasegawa and Tappert in 1973 [21, 22] and realised experimentally seven years later by Mollenauer *et.al.* [68]. The delay between theoretical proposal and experimental realisation can mainly be attributed to the lack of low-loss optical fibres before 1980 [69]. Since their discovery, optical Kerr solitons have been the subject of numerous studies and they have often been proposed as an efficient and fast way to transmit data over large distances.

Kerr solitons can be described by the nonlinear Schrödinger equation (NLSE). The derivation of this equation from the fundamental equations of light propagation given here is based mainly on the derivation in [70]. Let us start with the local response in the electric-dipole approximation given by

$$\begin{aligned} \mathbf{P}(\mathbf{r},t) &= \mathbf{P}_{\mathrm{L}}(\mathbf{r},t) + \mathbf{P}_{\mathrm{NL}}(\mathbf{r},t) \\ &= \epsilon_0 \int_{-\infty}^{\infty} \chi^{(1)}(t-t') \cdot \mathbf{E}(\mathbf{r},t')dt' + \\ &\quad \epsilon_0 \int\int\int_{-\infty}^{\infty} \chi^{(3)}(t-t_1, t-t_2, t-t_3) \\ &\quad \cdot \mathbf{E}(\mathbf{r},t_1)\mathbf{E}(\mathbf{r},t_2)\mathbf{E}(\mathbf{r},t_3)dt_1 dt_2 dt_3 \,, \end{aligned} \tag{2.24}$$

under the assumption of inversion symmetry of the medium (second order nonlinearity is non-existent). Assuming that the third-order nonlinearity is instantaneous allows one to replace

$$\mathbf{P}_{\mathrm{NL}}(\mathbf{r},t) = \epsilon_0 \chi^{(3)} \mathbf{E}(\mathbf{r},t)\mathbf{E}(\mathbf{r},t)\mathbf{E}(\mathbf{r},t) \,. \tag{2.25}$$

This approximation neglects the Raman effect and is valid as long as the considered pulse durations are much longer than the response time of the medium. The nonlinear polarisation is usually much smaller (six orders of magnitude) than the linear polarisation, which makes it possible to treat the nonlinear index as a perturbation to the linear index. Furthermore, the polarisation of the field is assumed to be maintained, i.e. non-birefringent materials are assumed. Slowly varying envelopes are defined for almost monochromatic fields with frequency ω_0

$$\mathbf{E}(\mathbf{r},t) = \frac{1}{2}\hat{x}[E(\mathbf{r},t)\exp(-i\omega_0 t) + c.c.] \tag{2.26}$$

with $\hat{x}$ the unit vector of the polarisation. Finally, the nonlinear polarisation contains terms oscillating at a frequency $3\omega_0$, which would need to be phase-matched to amount to a considerable contribution and can usually be neglected. Applying these approximations results in a scalar polarisation

$$P_{\mathrm{NL}} \approx \epsilon_0 \epsilon_{\mathrm{NL}} E(\mathbf{r}, t)\,, \tag{2.27}$$

with

$$\epsilon_{\mathrm{NL}} = \frac{3}{4}\chi^{(3)}_{xxxx}|E(\mathbf{r}, t)|^2\,. \tag{2.28}$$

Often this is expressed in terms of the refractive index as

$$n = n_0 + n_2 I\,, \tag{2.29}$$

with the linear refractive index n_0, the nonlinear index $n_2 = 3/(8n)Re(\chi^3_{xxxx})$ and the light intensity I.

If the electric field describes a pulse in a waveguide mode, it can be written as

$$E(\mathbf{r}, t) = A(z, t)\mathbf{F}(x, y)\exp\left(i\beta_0 z\right), \tag{2.30}$$

with the mode profile $\mathbf{F}(x, y)$, the envelope $A(z, t)$ and the propagation constant of the centre frequency β_0. In a waveguide one arrives at an equation for the Fourier transform of the envelope $\hat{A}(z, \omega)$

$$\frac{\partial \hat{A}}{\partial z} = i[\beta(\omega) + \frac{\phi_{\mathrm{NL}}}{L} - \beta_0]\,, \tag{2.31}$$

where ϕ_{NL} is the nonlinear phase shift acquired in propagation down the fibre length L given by

$$\phi_{\mathrm{NL}} = \frac{2\pi n_2}{\lambda}\frac{P}{A_{\mathrm{eff}}}L\,. \tag{2.32}$$

Here, A_{eff} is an effective nonlinear area of the waveguide whose value can be derived by calculating the nonlinear phase shift from an intensity-weighted average of the phase shift across the waveguide as

$$\phi_{\mathrm{NL}} = \frac{2\pi}{\lambda}L|A|^2\frac{\int\int_{-\infty}^{\infty} n_2(x, y)F^4(x, y)\mathrm{d}x\mathrm{d}y}{\int\int_{-\infty}^{\infty}|\mathbf{F}(x, y) \times \mathbf{G}(x, y)|\mathrm{d}x\mathrm{d}y}\,, \tag{2.33}$$

where $\mathbf{G}(x,y)$ is the magnetic field profile. Since $P = \int\int_{-\infty}^{\infty} |A(z,t)^2\mathbf{F}(x,y)\times\mathbf{G}(x,y)|\mathrm{d}x\mathrm{d}y$ the effective area A_{eff} for a Kerr-type nonlinearity must be given by

$$A_{\text{eff}} = \frac{\left[\int\int_{-\infty}^{\infty} \mathbf{F}(x,y)\times\mathbf{G}(x,y)\mathrm{d}x\mathrm{d}y\right]^2}{\int\int_{A_{\text{int}}} F^4(x,y)\mathrm{d}x\mathrm{d}y}\,, \tag{2.34}$$

where A_{int} denotes the region of $n_2(x,y) = n_2 \neq 0$.

A propagation equation for $A(z,t)$ can be found by transforming back to the time-domain. Hence, we have to find an expression for $\beta(\omega)$ in the time-domain. To this end a Taylor expansion of $\beta(\omega)$ around $\beta(\omega_0)$ is performed. Replacing $\omega - \omega_0$ by $i(\partial_t)$ and neglecting terms beyond second order we get

$$\frac{\partial A}{\partial z} + \beta_1\frac{\partial A}{\partial t} + \frac{i\beta_2}{2}\frac{\partial^2 A}{\partial t^2} = i\frac{2\pi n_2}{\lambda}\frac{|A|^2 A}{A_{\text{eff}}}\,, \tag{2.35}$$

whereby $\beta_m = \left(\frac{\mathrm{d}^m\beta}{\mathrm{d}\omega^m}\right)$ are the dispersion parameters ($\beta_1 = 1/v_g$ and $\beta_2 = -D\frac{\lambda^2}{2\pi c}$). A variable transformation leads to the nonlinear Schrödinger equation

$$i\frac{\partial u}{\partial z} - \frac{s}{2}\frac{\partial^2 u}{\partial t^2} \pm |u|^2 u = 0\,, \tag{2.36}$$

where $s = \mathrm{sgn}(\beta_2) = \pm 1$ is the sign of the group velocity dispersion parameter and the nonlinear term can be positive or negative depending on the material employed (it is positive for silica fibres). If β_2 is negative the waveguide has so-called anomalous dispersion and if β_2 is positive it exhibits normal dispersion. Note that it is usually assumed that the guided modes of the nonlinear waveguide are well approximated by the modes of the linear waveguide, i.e. the refractive index change induced by the nonlinearity is much smaller than the refractive index differences in the linear waveguide.

The fundamental soliton solution to this equation (for anomalous dispersion and positive nonlinear term) can be found by choosing an Ansatz-function [70], whereas for higher-order solitons the inverse scattering transform [71] needs to be applied. If the fundamental soliton is given by the function

$$u(z,t) = V(t)\exp\left[i\phi(z)\right], \tag{2.37}$$

with phase function $\phi(z) = Kz + \text{const.}$ and an amplitude $V(t)$ that is independent of

propagation distance z, one arrives at the differential equation for the amplitude function

$$\frac{d^2V}{dt^2} = 2V(K - V^2)\,. \tag{2.38}$$

This equation can be integrated to obtain the fundamental soliton as [70]

$$u(z,t) = a\,\mathrm{sech}(at)\exp\left(ia^2z/2\right). \tag{2.39}$$

One can see from this equation that the amplitude a and the duration of the pulse (determined by the argument of sech) obey a fixed relation, a so-called area theorem. Physically this relation is given as

$$N^2 = 2\pi\lambda n_2 A_{\mathrm{eff}} P_0 T_0^2/|\beta_2|\,, \tag{2.40}$$

where P_0 is the maximum power of the soliton, T_0 is its duration ($1.763T_0 = T_{\mathrm{FHWM}}$), and the soliton order $N = 1$ for the fundamental soliton. Pulses close to the soliton shape and amplitude ($0.5 < N < 1.5$) will evolve into the fundamental soliton, an evolution that can be understood as equivalent to the evolution of a pulse that is injected into a linear waveguide with a profile, which does not match the mode shape. In both cases, a fraction of the pulse energy will be coupled into the modes and another fraction forms dispersive waves (sometimes called radiation). In the case of the soliton the pulse is coupled into a temporal mode of a nonlinear equation [70].

As mentioned above, to determine the higher-order soliton solution of the NLSE the inverse scattering transform (IST) method [17, 71] has to be employed. This method can be understood as a nonlinear generalisation of the Fourier transform method that finds the eigenvalues of a nonlinear equation. The Fourier transform method, which was also applied to find the guided modes in Section 2.2, is only applicable if the superposition principle holds and can therefore not be used for nonlinear propagation equations. The nonlinear decomposition used by the IST is only possible for certain special nonlinear equations, which are called exactly integrable equations.

In essence, when applying the IST one maps the nonlinear differential equation onto a system of linear ordinary differential equations (LODE) that is then solved. Its solutions are transformed back to obtain the solution of the nonlinear equation [72]. A spectral

parameter λ and time t are parameters of the LODE, while the solution $u(x,t)$ of the nonlinear differential equation is a coefficient of the LODE and usually referred to as potential. One specific method to find a LODE for a nonlinear differential equations is the Lax method [73]. If an operator L acting on a Hilbert space fulfils

$$\frac{\mathrm{d}L}{\mathrm{d}t} = [L, P] \,, \tag{2.41}$$

its eigenvalues are independent of time. Here, P is another operator on the same Hilbert space that depends on L in a defined way. Hence, equation (2.41) is a nonlinear differential equation and at the same time it is the compatibility condition of a LODE. Since the spectrum of L is independent of time one has $\lambda(t) = \lambda(0)$ and for the eigenfunctions ψ one has $\partial\psi/\partial_t = P\psi$. Assuming an initial value $u(x, t = 0)$ for the potential one can then define $P(t = 0)$ and arrive at the scattering data for all times. Out of those scattering data it is possible to determine $u(x,t)$ as a solution of the original nonlinear differential equation. The solution that corresponds to reflection-less potentials are the soliton solutions.

For the nonlinear Schrödinger equation (2.36) the Lax pair is [72]

$$L = i \cdot \begin{bmatrix} 1 & 0 \\ 0 & -1 \end{bmatrix} \partial_x - i \begin{bmatrix} 0 & u(x,t) \\ \overline{u(x,t)} & 0 \,, \end{bmatrix} \tag{2.42}$$

and

$$P = 2i \cdot \begin{bmatrix} 1 & 0 \\ 0 & -1 \end{bmatrix} \partial_x^2 - 2i \begin{bmatrix} 0 & u \\ \overline{u} & 0 \,, \end{bmatrix} \partial_x - i \begin{bmatrix} |u|^2 & u_x \\ \overline{u_x} & |u|^2 \,. \end{bmatrix} \tag{2.43}$$

Using this Lax pair the IST can be performed to obtain the soliton solutions of the nonlinear Schrödinger equation.

Self-induced transparency, the subject of this thesis, is related to the so-called sine-Gordon equation

$$\partial_t^2\phi - \partial_x^2\phi + \sin(\phi) = 0 \,, \tag{2.44}$$

or equivalently

$$\partial_t\partial_x\phi - \sin(\phi) = 0 \,, \tag{2.45}$$

which can be obtained as an approximation to the physical problem of resonant dipole

interaction between light and quantum mechanical two-level systems. The sine-Gordon equation belongs to the integrable nonlinear differential equations and its Lax pair is given as [74]

$$L = \begin{bmatrix} i\lambda & -\frac{1}{2}u_x \\ \frac{1}{2}u_x & -i\lambda \end{bmatrix}, \tag{2.46}$$

and

$$P = \begin{bmatrix} -\frac{i}{4}\cos(u) & -\frac{i}{4}\sin(u) \\ -\frac{i}{4}\sin(u) & \frac{i}{4}\cos(u). \end{bmatrix} \tag{2.47}$$

A discussion of the fundamental soliton solution, the so-called 2π-pulse is provided in Section 3.3.

Chapter 3

Resonant light-matter interaction: the Maxwell-Bloch equations

In the previous chapter only two possible responses of matter to light were discussed. The first is the linear response with a linear susceptibility χ that gives rise to the following polarisation

$$P(t) = \int_{-\infty}^{\infty} \mathrm{d}\tau \chi(t-\tau) E(\tau) \tag{3.1}$$

and the second is the instantaneous Kerr response

$$P(t) = \chi_3 E(t)^3 \tag{3.2}$$

which produces an intensity dependent refractive index change. Neither model is appropriate for the description of resonant light-matter interaction. In resonant light-matter interaction the frequency of the exciting light field corresponds to the energy difference between two possible electronic configurations in the medium, configuration 1 and configuration 2 ($\hbar\omega = E_2 - E_1$). Here, the light field can stimulate a transition from electronic configuration (state) 1 to state 2 and a quantum mechanical model is necessary to describe the medium and its response. The quantum nature of the electromagnetic field is neglected throughout this thesis as the classical picture is a good approximation for the intense, coherent light pulses considered here.

In this chapter first the semi-classical model for an electric dipole transition between different electronic states driven by an electromagnetic field, the optical Bloch equations

are introduced (see Sec. 3.1). The same section also discusses Rabi oscillations, an analytic solution of the Bloch equations that is especially important for the phenomenon of self-induced transparency. Next, the theory behind robust complete population transfer via adiabatic rapid passage, another consequence of the Bloch equations is introduced in Sec. 3.2. Finally, SIT is explained in terms of the Maxwell-Bloch equations and the significance of the necessary approximations is discussed in Sec. 3.3

3.1 The optical Bloch equations

Optical dipole transitions in electronic media can be described most efficiently by the so-called Bloch equations, which are Liouville equations for the density matrix of the electronic states augmented by phenomenological relaxation and dephasing rates to include coupling to a dissipative environment. These equations thus constitute the fundamental equations for the absorption and stimulated emission of light as long as the dipolar approximation is applicable. Since electrons bound in an atom or molecule are confined to a length scale much smaller than the wavelength of light that is resonant with the transition energies, the dipole approximation is almost always applicable in the description of atomic and molecular transitions.

The semi-classical Hamiltonian of light-matter interaction in electric dipole approximation is written as

$$\hat{H} = \sum_i \hbar\omega_i \rho_{ii} - \sum_{i,j\neq i} \mathbf{E}\boldsymbol{\mu}_{ij}\rho_{ji}\,. \tag{3.3}$$

Here, $\hbar\omega_i$ is the energy of the i^{th} electronic eigenstate, ρ_{ii} is its occupation density, ρ_{ij} is the coherence between states i and j, $\boldsymbol{\mu}_{ij}$ is the dipole strength between state i and j, while $\mathbf{E}$ is the electric field vector. Combining this with the Liouville equation

$$i\hbar\frac{\partial}{\partial t}\hat{\rho} = [\hat{H}, \hat{\rho}]\,, \tag{3.4}$$

then leads to the semi-classical evolution equations of a general multi-level electronic system driven by a classical electromagnetic field. With the addition of relaxation and dephasing rates one gets the Bloch equations of a multi-level electronic system in the presence of dissipation. In order to arrive at the Maxwell-Bloch equations it is necessary to specify how the electronic system influences the exciting electromagnetic field via its

polarisation. The polarisation $\mathbf{P}$ of a multi-level system is calculated from the coherences ρ_{ij}

$$\mathbf{P}(t) = \sum_{i,j\neq i} \rho_{ij}(t) N \boldsymbol{\mu}_{ij} \,, \tag{3.5}$$

where N is the number density of electronic systems.

3.1.1 Two-level systems

The complexity of the Hamiltonian (3.3) strongly depends on the number of transitions that are assumed to be excitable by the given light field. If many transitions are considered the integration of the resulting Liouville equations quickly becomes prohibitively complicated. Laser light, however, is usually almost monochromatic in which case it is safe to assume that the light is resonant with only a few, or sometimes even only one, transition in the atom or molecule. A canonical example for which the two-level approximation is often appropriate is rare earth ions. Their resonance frequency coincides with the low loss window in typical transmission fibres, they have a large dipole moment and are easily integrated into optical fibres via doping. For these reasons rare earth ions are widely employed to produce fibre amplifiers or lasers for optical telecommunication purposes [75]. All the off-resonant contributions to the light-matter interaction can then be summarised with a (possibly frequency-dependent) dielectric constant and only the resonant contributions are integrated explicitly.

Here, we first explore the semi-classical Bloch equations under the assumption that the exciting light field is resonant with only one electronic dipole transition of the atom or molecule. The Hamiltonian (3.3) then reduces to

$$\hat{H}_2 = \hbar(\omega_1\rho_{11} + \omega_2\rho_{22}) - (\mathbf{E}\boldsymbol{\mu}_{12}\rho_{21} + \mathbf{E}\boldsymbol{\mu}_{21}\rho_{12}) \,, \tag{3.6}$$

and the Liouville equation results in the differential equations for the density matrix elements

$$\begin{aligned}
\frac{\partial}{\partial t}\rho_{12} &= i[\rho_{12}(\omega_1 - \omega_2) + \Omega_{12}(\rho_{11} - \rho_{22})] \\
\frac{\partial}{\partial t}\rho_{11} &= -2\mathbf{Im}(\Omega_{12}\rho_{12}) \\
\frac{\partial}{\partial t}\rho_{22} &= 2\mathbf{Im}(\Omega_{12}\rho_{12}) \,,
\end{aligned} \tag{3.7}$$

with $\Omega_{12} = \boldsymbol{\mu}_{12}\mathbf{E}/\hbar$ the Rabi frequency of the transition. One important conserved quantity of these equations is the length of the so-called Bloch vector (2Re(ρ_{12}),2Im(ρ_{12}),$\rho_{22}-\rho_{11}$).

In these equations it is assumed that the two levels of the electronic system are isolated from their environment. This is a good approximation if the interaction with the environment takes place on much longer time-scales than the duration of the exciting light pulse. If this is not the case, the dissipative interaction with the environment must be included in the equations (3.7) by the introduction of phenomenological dephasing and relaxation rates. As a result one gets the Bloch equations for a two-level system that were originally developed by Felix Bloch to describe nuclear magnetic resonance phenomena [76] and are equally valid for optical transitions [77]

$$\begin{aligned}
\frac{\partial}{\partial t}\rho_{12} &= i[\rho_{12}(\omega_1-\omega_2)+\Omega_{12}(\rho_{11}-\rho_{22})]-\gamma_p\rho_{12} \\
\frac{\partial}{\partial t}\rho_{11} &= -2\mathbf{Im}(\Omega_{12}\rho_{12})+\gamma_r(\rho_{22}-\rho_{22}^{\mathrm{eq}}) \\
\frac{\partial}{\partial t}\rho_{22} &= 2\mathbf{Im}(\Omega_{12}\rho_{12})-\gamma_r(\rho_{22}-\rho_{22}^{\mathrm{eq}})\,.
\end{aligned} \tag{3.8}$$

ρ_{22}^{eq} is the thermodynamic equilibrium value of the upper state population and is given by 0 for optical transitions. Note that the addition of dephasing rates and relaxation rates leads to non-conservation of the length of the Bloch vector.

Let us for the moment assume that relaxation and dephasing can be neglected and analyse equations (3.7) in more detail. If we transform equations (3.7) to a coordinate system rotating at the resonance frequency $\omega_2-\omega_1$ and apply the rotating wave approximation (RWA), neglecting terms oscillating in the new coordinate frame with a frequency $\omega \approx 2(\omega_2-\omega_1)$, we arrive at the following system of equations

$$\frac{\partial}{\partial t}\begin{bmatrix} u \\ v \\ w \end{bmatrix} = \begin{bmatrix} 0 & -\delta & 0 \\ \delta & 0 & \Omega_{12} \\ 0 & -\Omega_{12} & 0 \end{bmatrix}\begin{bmatrix} u \\ v \\ w \end{bmatrix}\,. \tag{3.9}$$

Here, δ is the detuning between the frequency of the light field ω and the resonance frequency of the transition $\omega_0 = \omega_2-\omega_1$. If we assume perfect resonance $\delta = 0$ the equations for the Bloch vector in RWA correspond to a simple rotation of the vector

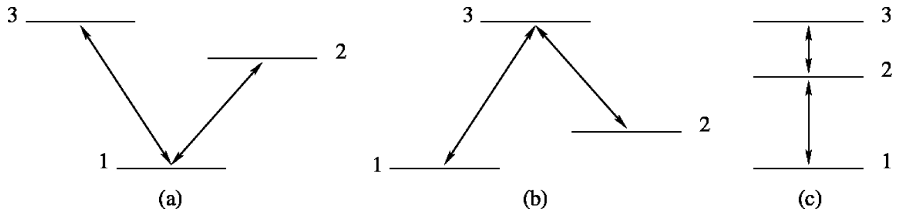


Figure 3.1: Possible three-level configurations: (a) V-scheme, (b) Λ-scheme and (c) cascade.

around the u-axis with the Rabi-frequency as the frequency of rotation. Therefore, if we assume that the system is initially in its ground-state 1, the solution of the on-resonance Bloch equation is

$$\begin{bmatrix} u(t) \\ v(t) \\ w(t) \end{bmatrix} = \begin{bmatrix} 0 \\ \sin\left(\int_{t_0}^{t_1} \Omega_{12}(t)\right) \\ -\cos\left(\int_{t_0}^{t_1} \Omega_{12}(t)\right) \end{bmatrix} . \tag{3.10}$$

w is simply the inversion $\rho_{22} - \rho_{11}$ and v is the in-quadrature component of the polarisation. These solutions imply that the inversion of the two-level system oscillates with the Rabi-frequency from the ground-state value $w = -1$ to the excited state value $w = 1$, a phenomenon termed Rabi-oscillations [78]. A light pulse that inverts the system to $w = 1$ is called a π-pulse due to the integral over its Rabi-frequency, whereas a pulse that rotates the system from ground-state via excited state back to ground-state is called a 2π-pulse for obvious reasons. The introduction of a dephasing rate into equations (3.9) leads to damped Rabi-oscillations where the Bloch vector decreases in magnitude, while a relaxation rate continuously drives the inversion back to its equilibrium value. The interaction between light and an atomic or molecular two-level system is termed coherent if the latter effects can be neglected. In this thesis we will mostly be concerned with such coherent effects, but sometimes dephasing rates will be introduced to estimate their impact on the coherent dynamics.

3.1.2 Three-level systems

The simplest extension of the two-level system is the three-level system in which one additional electric dipole transition is added. Possible configurations of three-level systems with two optical transitions are shown in Fig. 3.1. A three-level system is a good model

for a number of atoms and molecules if the exciting light fields are resonant with two transitions in the system which have one level in common and it is the minimal model for a laser gain material.

The state of the electron is given by a 3×3 density matrix $\hat{\rho}$ and its time evolution can be described by a 3×3 Hamiltonian $\hat{H}$ via the Liouville equation (3.4). For a three-level system in electric dipole approximation the Hamiltonian can be written as

$$\hat{H} = \hat{H}_0 - \mathbf{E}\boldsymbol{\mu} = \begin{bmatrix} \hbar\omega_1 & -\boldsymbol{\mu}_{12}\mathbf{E} & -\boldsymbol{\mu}_{13}\mathbf{E} \\ -\boldsymbol{\mu}_{12}^*\mathbf{E} & \hbar\omega_2 & -\boldsymbol{\mu}_{23}\mathbf{E} \\ -\boldsymbol{\mu}_{13}^*\mathbf{E} & -\boldsymbol{\mu}_{23}^*\mathbf{E} & \hbar\omega_3 \end{bmatrix}, \tag{3.11}$$

with $\mathbf{E} = E_x\mathbf{e}_x + E_y\mathbf{e}_y + E_z\mathbf{e}_z$ denoting the electric field, $\boldsymbol{\mu}_{jk} = \mu_{jk}^x\mathbf{e}_x + \mu_{jk}^y\mathbf{e}_y + \mu_{jk}^z\mathbf{e}_z$ the dipole matrix element between state j and k, and $\hbar\omega_i$ the energy of level i.

The Liouville equation (3.4) together with the Hamiltonian (3.11) result in the equations of motion for the dynamics of a three-level system in dipole approximation excited by a light field

$$\begin{aligned}
\frac{\partial}{\partial t}\rho_{12} &= i[\rho_{12}(\omega_1 - \omega_2) + \Omega_{12}(\rho_{11} - \rho_{22}) + \Omega_{23}^*\rho_{13} - \Omega_{13}\rho_{23}^*] \\
&\quad -\gamma_{12}^p\rho_{12} \\
\frac{\partial}{\partial t}\rho_{13} &= i[\rho_{13}(\omega_1 - \omega_3) + \Omega_{13}(\rho_{11} - \rho_{33}) + \Omega_{23}\rho_{12} - \Omega_{12}\rho_{23}] \\
&\quad -\gamma_{13}^p\rho_{13} \\
\frac{\partial}{\partial t}\rho_{23} &= i[\rho_{23}(\omega_2 - \omega_3) + \Omega_{23}(\rho_{22} - \rho_{33}) + \Omega_{13}\rho_{12}^* - \Omega_{12}^*\rho_{13}] \\
&\quad -\gamma_{23}^p\rho_{23} \\
\frac{\partial}{\partial t}\rho_{11} &= -2\mathbf{Im}(\Omega_{12}\rho_{12}) - 2\mathbf{Im}(\Omega_{13}\rho_{13}) + \gamma_{12}^r\rho_{22} + \gamma_{13}^r\rho_{33} \\
\frac{\partial}{\partial t}\rho_{22} &= 2\mathbf{Im}(\Omega_{12}\rho_{12}) - 2\mathbf{Im}(\Omega_{23}\rho_{23}) - \gamma_{12}^r\rho_{22} + \gamma_{23}^r\rho_{33} \\
\frac{\partial}{\partial t}\rho_{33} &= 2\mathbf{Im}(\Omega_{13}\rho_{13}) + 2\mathbf{Im}(\Omega_{23}\rho_{23}) - (\gamma_{13}^r + \gamma_{23}^r)\rho_{33}\,,
\end{aligned} \tag{3.12}$$

with $\Omega_{ij} = \boldsymbol{\mu}_{ij}^*\mathbf{E}/\hbar$ and polarisation dephasings γ^p and population relaxation terms γ^r.

The coherences of the optical transitions contribute a polarisation, so that the electric field is calculated from the electric displacement $\mathbf{D}$ as

$$\mathbf{E}(t) = \frac{1}{\epsilon}(\mathbf{D}(t) - \mathbf{P}(t))\,, \tag{3.13}$$

with

$$\mathbf{P}(t) = N \cdot \mathrm{tr}(\hat{\rho}(t)\hat{\boldsymbol{\mu}}) = 2N \sum_{i \neq j} \mathbf{Re}(\boldsymbol{\mu}_{ij}\rho_{ij}(t)) \,. \tag{3.14}$$

3.1.3 Local Field Effect and the effect of a Dielectric

The model above assumes an ensemble of non-interacting atoms. For dense media the direct interaction between atoms via induced dipoles becomes more important with increasing interaction time [79]. In a very good approximation the dipole-dipole interaction between the atoms can be accounted for by introducing the microscopic (local) field felt by an atom in a certain local neighbourhood, which differs from the macroscopic electric field. The local field acting on the atom is [80]

$$\mathbf{E}_{loc} = \mathbf{E} + \frac{\mathbf{P}}{3} \,. \tag{3.15}$$

If a dipole is embedded in a dielectric, the atoms of the dielectric act on the dipole. The influence of a dielectric on an embedded dipole can be represented by amplifying the local electric field by a factor $l = (\epsilon + 2)/3$. Therefore a dipole embedded in a dielectric feels a field of [80]

$$\mathbf{E}_{loc} = \frac{\epsilon + 2}{3}(\mathbf{E} + \frac{P}{3}) \,. \tag{3.16}$$

3.2 Atomic excitations via adiabatic rapid passage

In the previous sections we have seen that an intense, coherent light pulse, which resonantly excites an electronic transition can induce Rabi oscillations in the occupation densities of the electronic states. Furthermore, Rabi oscillations are suppressed if the dephasing rate of the transition is larger than the Rabi frequency; in this case the transition saturates. However, Rabi oscillations and saturation are not the only two possible outcomes of the interaction between a resonant light-pulse and an absorbing two-level system.

When a chirped pulse, i.e. a pulse with a time-dependent instantaneous frequency, interacts with a two-level system, the phenomenon of adiabatic rapid passage (ARP) [52, 81, 82] can occur, in which the population is transferred completely to the upper state of the two-level system. The crucial difference to a π-pulse excitation is, that

no exact resonance condition is required and the amplitude of the exciting pulse can be varied considerably without effecting the final inversion. Hence, adiabatic rapid passage can be used to transfer the population in inhomogeneously broadened atomic or molecular ensembles and along a transverse pulse profile. ARP is best understood in terms of the semi-classical Schrödinger equations in the RWA, where the Hamiltonian is written in the interaction picture and the fast oscillating parts of the light-matter interaction are neglected

$$\hat{H} = \hat{H}_0 - \hat{\mu} \cdot \varepsilon = \hbar \begin{bmatrix} 0 & \Omega(t)/2 \\ \Omega(t)/2 & \triangle(t) \end{bmatrix} . \tag{3.17}$$

Here, a real Rabi frequency $\Omega = \varepsilon\hat{\mu}/\hbar$ is assumed, $\triangle$ is the instantaneous detuning between light field and transition resonance and ε is the electric field envelope.

For the time-dependent Hamiltonian (3.17) new time-dependent eigenstates $\Phi_\pm$ of the complete system can be found that do not coincide with the eigenstates ψ_i of the unperturbed electronic system. These adiabatic states are given in terms of the unperturbed (diabatic) states as [82]

$$\begin{aligned} \Phi_+ &= \psi_1 \sin\theta(t) + \psi_2 \cos\theta(t) \\ \Phi_- &= \psi_1 \cos\theta(t) - \psi_2 \sin\theta(t) . \end{aligned} \tag{3.18}$$

The mixing angle θ is then given by

$$\theta = \frac{1}{2} \arctan\left[\frac{\Omega(t)}{\triangle(t)}\right], \tag{3.19}$$

and the eigenenergies by

$$\hbar\epsilon_\pm(t) = \frac{1}{2}\hbar\left[\triangle(t) \pm \sqrt{\triangle^2(t) + \Omega^2(t)}\right] . \tag{3.20}$$

In Fig. 3.2(a) the evolution of the adiabatic energies is shown by the solid lines for a positively chirped Gaussian pulse.

The concept of adiabatic following implies that the system stays in a specific adiabatic state if it has been prepared in that state [83]. An adiabaticity condition can be formulated for the Hamiltonian (3.17) that ensures a negligible probability for the

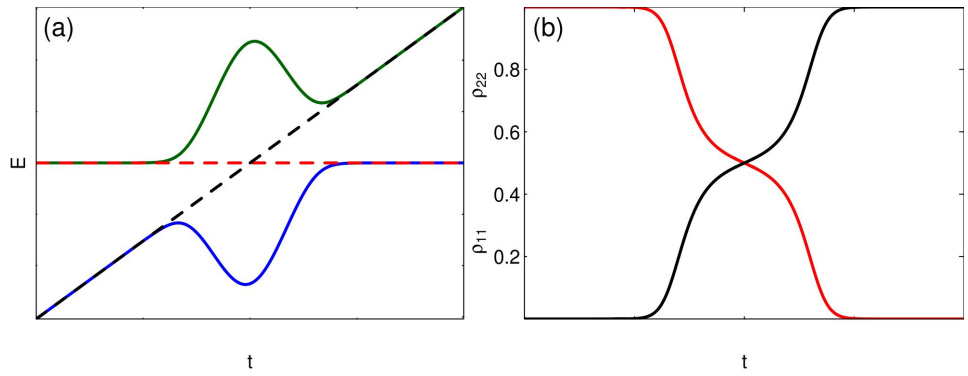


Figure 3.2: (a) Evolution of energies E of adiabatic (solid lines) and diabatic states (dashed lines) in the rotating wave approximation for a positively chirped Gaussian pulse. (b) Evolution of occupation densities in the diabatic basis for a system initially in the ground state (red) and following the adiabatic state Φ_+ [solid green line in (a)].

system leaving the adiabatic state

$$\frac{1}{2}\left|\dot{\Omega}\triangle - \Omega\dot{\triangle}\right| \ll (\Omega^2 + \triangle^2)^{3/2}\,. \tag{3.21}$$

This condition means that the pulse must be smooth ($\dot{\Omega}$ small), the chirp (equivalent to $\dot{\triangle}$) must not be too large and a large Rabi frequency and/or detuning must be present at all times. These requirements lead to the intuitive notion that a long pulse should be used, but, in fact, the adiabaticity condition relates to the pulse area. In the limits of practicality, short pulse lengths can be counterbalanced by large pulse intensities. The energies of the adiabatic states, depicted in Fig. 3.2(a) show an avoided crossing, so that an adiabatic evolution leads to an inversion of the system in the diabatic basis. This population evolution is shown in Fig. 3.2(b).

A second constraint on system parameters for the success of ARP is related to the approximation employed when deriving the interaction Hamiltonian. The electronic two-level system has been assumed to be free of dephasing or relaxation processes. Such an approximation is only valid when the interaction time is much shorter than the dephasing or relaxation times, so that ARP also requires slow dephasing and relaxation and/or short pulses. This is the origin of the term "rapid" in adiabatic rapid passage.

Consider a positively chirped pulse with large negative detuning at the beginning of the pulse and large positive detuning at the end of the pulse acting on a two-level system initially in the ground-state Ψ_1. Adiabatic evolution will lead the population along a

path towards the upper state Ψ_2 defined by the time-dependence of the mixing angle θ. The same happens, if the pulse is negatively chirped instead.

The technique of ARP can be used to control the state of an electronic system by illumination with a suitable light pulse [84, 85] in applications as diverse as nuclear magnetic resonance [86], magnetic resonance imaging, femtochemistry [87], single photon generation [88] and quantum computing [89]. In the case of molecules this technique can excite a specific transition between several closely spaced transitions or a number of transitions that are slightly detuned from each other because of, e.g., vibrational sublevels or Doppler broadening. Recently, it has also been successfully employed to achieve very efficient excitations in semiconductor quantum dots [90, 91].

For the efficient excitation of two-level systems the sign of the chirp is not important, whereas in multi-level systems relaxations and thermalisations (pump-dump effects) can lead to large differences between the excitation efficiencies of negatively and positively chirped pulses [85, 92, 93]. For a coherent two-level system in free-space, which is resonantly excited by a linearly chirped Gaussian pulse with at least a few cycles duration, it has been shown that the achieved population inversion depends only on two parameters [52], the pulse area and the magnitude of the chirp. Both parameters can be expressed as dimensionless values and adiabatic rapid passage using linearly chirped Gaussian pulses reaches more than 99% efficiency if the pulse area is much larger than π and the chirp is larger than 4 (compare Figure 4 of [52]).

3.3 Self-induced transparency

This section introduces self-induced transparency [14], a nonlinear effect that arises in the resonant interaction between a light field and an electronic dipole transition. Previous sections have focused on the impact of light on the resonantly excited electronic system neglecting the impact of the polarisation of the electronic system on light propagation. Let us now take a step back and add the propagation equations for the light field, Maxwell's equations, to the two-level Bloch equations in order to understand light propagation through resonant media. The result are the Maxwell-Bloch equations, completely general semi-classical equations for the interaction of a light field with a single electric dipole transition. Therein, the electric dipole transition is described quantum

mechanically, whereas the light field is described classically. We write these Maxwell-Bloch equations as wave equations for the electric field since we assume non-magnetic materials

$$\begin{aligned}
\frac{\epsilon_b}{c^2}\partial_t^2\mathbf{E}(\mathbf{r},t) &= -\nabla\cdot(\nabla\cdot\mathbf{E}(\mathbf{r},t)) + \nabla^2\mathbf{E}(\mathbf{r},t) - \frac{1}{\epsilon_0 c^2}\partial_t^2\mathbf{P}(\mathbf{r},t) \qquad (3.22)\\
\frac{\partial}{\partial t}\rho_{12}(\mathbf{r},t,\omega_0) &= i[-\rho_{12}(\mathbf{r},t)\omega_0 + \Omega_{12}(\rho_{11}(\mathbf{r},t) - \rho_{22}(\mathbf{r},t))] - \gamma_p\rho_{12}(\mathbf{r},t)\\
\frac{\partial}{\partial t}\rho_{11}(\mathbf{r},t,\omega_0) &= -2\mathbf{Im}(\Omega_{12}(\mathbf{r},t)\rho_{12}(\mathbf{r},t)) + \gamma_r\rho_{22}(\mathbf{r},t)\\
\frac{\partial}{\partial t}\rho_{22}(\mathbf{r},t,\omega_0) &= 2\mathbf{Im}(\Omega_{12}(\mathbf{r},t)\rho_{12}(\mathbf{r},t)) - \gamma_r\rho_{22}(\mathbf{r},t)\\
\mathbf{P}(\mathbf{r},t) &= 2\int_{\omega_0}\mathrm{Re}\left(\boldsymbol{\mu}_{12}\rho_{12}(t,\mathbf{r},\omega_0)\right)N(\mathbf{r})\,.
\end{aligned}$$

Here, ω_0 is the transition frequency of the two-level system and the states of two-level systems with the same resonance frequency are summarised in density matrices. Variations in transition frequency are termed inhomogeneous broadening and can arise for example because of the Doppler effect, differences in local electric environments or, in a molecule, several vibrational sub-states more closely spaced than the broadness of the exciting light field.

In order to understand the meaning of self-induced transparency and what makes it special, we first have to consider the ordinary case of light propagating through a two-level system. Since the energetic difference between two electronic states with an optical dipole transition is much higher than the thermal energy available at room temperature such systems are usually in their ground-state. When light resonant with the transition impinges on these two-level systems, it can stimulate a transition from the ground-state to the upper state and, as a consequence, a portion of energy $E = \hbar\omega$ is lost from the light field. As long as the light field is weak most two-level systems remain in their ground-state and, for the system above, one recovers a Lorentzian absorption line-shape provided inhomogeneous broadening is absent. Every frequency contained in the weak light pulse propagating through these two-level systems attenuates with a constant attenuation rate per propagation distance that is given by the absorption line. This is known as Beer's law of absorption and is routinely used to measure the density/abundance of specific substances which are known to absorb at the particular frequency applied.

Self-induced transparency in the strict sense that no energy is absorbed by the two-

level system requires several conditions on light field, two-level system, and geometry [14]. The first and most important is that light propagation has to be constrained to one direction and the Rabi frequency has to be constant across the transverse dimensions of the light pulse. These conditions are fulfilled in plane-waves for which the first of equations (3.22) simplifies to

$$\frac{\epsilon_b}{c^2}\partial_t^2\mathbf{E}(z,t) - \partial_z^2\mathbf{E}(z,t) = -\frac{1}{\epsilon_0 c^2}\partial_t^2\mathbf{P}(z,t)\,, \tag{3.23}$$

where z is the propagation direction and the light field and polarisation are completely homogeneous along the transverse dimensions x and y. A further necessary assumption is, that dephasing times $1/\gamma_p$ and relaxation times $1/\gamma_r$ are much longer than the duration of the light pulse τ. In this case γ_p and γ_r can be neglected. Additionally, it is assumed that the light pulse has a slowly varying envelope ε in the sense that, if the electric field is written as

$$\varepsilon = \varepsilon \exp[-i(\omega t - kz - \phi(z))] + c.c.\,, \tag{3.24}$$

the conditions

$$\left|\frac{\partial\varepsilon}{\partial z}\right| \ll \left|\frac{\varepsilon}{\lambda}\right| \qquad , \qquad \left|\frac{\partial\varepsilon}{\partial t}\right| \ll \omega\,|\varepsilon|\,, \tag{3.25}$$

are fulfilled. As a consequence the polarisation varies slowly and because we assume that the light pulse and the two-level system are near resonance, we apply the RWA to the Bloch equations. These conditions allow us to write equation (3.23) as a first-order differential equation for the field propagating in, e.g., positive z-direction augmented by the Bloch equations in RWA

$$\begin{aligned}
\frac{\partial\varepsilon}{\partial z} &= -\frac{n\partial\varepsilon}{\partial t} - \frac{\omega}{2nc}\int_{-\infty}^{\infty} v(\triangle\omega, z, t)g(\triangle\omega)\mathrm{d}(\triangle\omega) \\
\frac{\partial\phi}{\partial z} &= \frac{\omega}{2nc}\int_{-\infty}^{\infty} u(\triangle\omega, z, t)g(\triangle\omega)\mathrm{d}(\triangle\omega) \\
\frac{\partial u}{\partial t} &= v\triangle\omega \\
\frac{\partial v}{\partial t} &= -u\triangle\omega - \frac{\kappa^2}{\omega}\varepsilon w \\
\frac{\partial w}{\partial t} &= v\varepsilon\omega\,.
\end{aligned} \tag{3.26}$$

Here, $v(\triangle\omega, z, t)$ is the component of the Bloch vector introduced in Sec. 3.1.1, $g(\triangle\omega)$ is an even distribution function of the transition frequencies centred around the frequency of the light pulse, and $\kappa = 2\mu/\hbar$ is the coupling strength between the electric field and the dipole with μ being the component of the dipole matrix element of the transition, which is parallel to the applied electric field.

In the derivation of the SIT solution to equations (3.26), we will follow the derivation by McCall and Hahn in [14]. For two-level systems exactly on resonance ($\triangle\omega = 0$), an explicit solution of the Bloch equations can be found that depends only on the electric field envelope

$$\begin{aligned} u(0,z,t) &= 0 \\ v(0,z,t) &= \frac{N}{2\hbar}\kappa \sin(\varphi(z,t)) \\ w(0,z,t) &= w(0,z,0)\cos(\varphi(z,t))\,, \end{aligned} \tag{3.27}$$

where

$$\varphi(z,t) = \kappa \int_{-\infty}^{t} \varepsilon(z,t')\mathrm{d}t'\,, \tag{3.28}$$

is the angle of rotation of the Bloch vector or the pulse area up to time t. Note that, since – in this coherent limit – the polarisation depends on the sine of the pulse area it is not only nonlinear, but its nonlinearity contains all odd orders and any truncation scheme for the order of nonlinearity must inevitably neglect important contributions.

McCall and Hahn now go on to define the total tipping angle θ of the polarisation by

$$\tan(\theta(z)) = \frac{\omega v(0,z,\infty)}{\kappa w(0,z,\infty)} \tag{3.29}$$

and proceed to integrate the first of equations (3.26) over time to reach an equation for the evolution of the tipping angle θ (pulse area)

$$\frac{\partial\theta(z)}{\partial z} = -\frac{\omega\kappa}{2nc}\int_{-\infty}^{\infty}\int_{-\infty}^{t=T\to\infty} g(\triangle\omega)v(\triangle\omega,z,t)\mathrm{d}t\mathrm{d}(\triangle\omega)\,. \tag{3.30}$$

Here, the time integration reaches up to a time where the macroscopic electric field has disappeared, which does not necessarily imply that the polarisations are zero individually, but that they are sufficiently out of phase to interfere destructively. By replacing v

with $(\partial u/\partial t)/\omega$ and performing the time integration, one obtains the following equation for the on-resonance pulse area θ

$$\frac{\partial\theta(z)}{\partial z} = -\frac{\omega\kappa}{2nc}\int_{-\infty}^{\infty}\frac{g(\triangle\omega)}{\triangle\omega}[u(\triangle\omega, z, T_0)\cos(\triangle\omega t')+ v((\triangle\omega, z, T_0)\sin(\triangle\omega t')]\mathrm{d}(\triangle\omega)\,, \quad (3.31)$$

with T_0 being a time where the electric field is negligibly small. The contribution from u vanishes for long times t', whereas the contribution for v tends to a δ-function.

It is now possible to combine all the above results in the area theorem

$$\frac{\mathrm{d}\theta(z)}{\mathrm{d}z} = -\frac{\alpha}{2}\sin(\theta(z))\,, \quad (3.32)$$

where $\alpha = \frac{2\pi\mu^2 N\omega g(0)}{n\hbar c}$ is the linear absorption coefficient of the two-level system. This theorem contains the phenomenon of self-induced transparency. For a pulse with an area that is an integer multiple of 2π the pulse area will not change with propagation distance. Furthermore, the area of any pulse propagating through a coherent resonant absorber tends to such an integer multiple of 2π.

It is also possible to establish the shape attained by the pulses propagating through an absorber. In fact, there is a unique solitary solution to equations (3.26); a 2π-pulse with a sech-shaped envelope. Pulses with higher area split into those elementary solitons. Since some of the energy of the electromagnetic field is always stored intermittently in the absorbing medium, the pulse travels slower than in an ordinary dielectric. The time and space dependence of the pulse envelope that constitutes a soliton solution to equations (3.26) can be found as

$$\varepsilon(z,t) = \frac{\hbar}{\mu\tau}\mathrm{sech}[(t - z/V)/\tau]\,, \quad (3.33)$$

with the group velocity V of the pulse given as

$$\frac{1}{V} = \frac{\omega\mu^2 N\tau^2}{\hbar n\epsilon_0} + \frac{n}{c}\,, \quad (3.34)$$

which can be rewritten as

$$\frac{1}{V} = \frac{E_{\mathrm{twolvl}}}{E_{\mathrm{e.m.}}} + \frac{n}{c}\,. \quad (3.35)$$

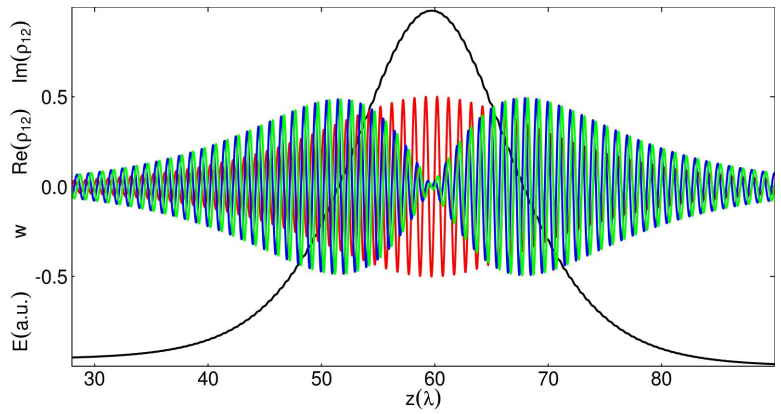


Figure 3.3: Snapshot of electric field (red), inversion (black), real part of polarisation (blue) and imaginary part of polarisation (green) of a 2π-pulse shown versus propagation distance for a sech-shaped pulse with $\tau = 20$cycles.

Essentially, the pulse is slowed down by the storage of energy in the medium.

Bullough *et al.* have shown in 1974 [94] that the analysis of SIT can also be performed using the inverse scattering transform [17, 71], a technique that was developed shortly after the work by McCall and Hahn was published. Equations (3.26) can be mapped onto the sine-Gordon equation [20] (named for its similarity to the Klein-Gordon equation)

$$\partial_t^2\varphi - \partial_z^2\varphi + \sin(\varphi) = 0\,, \tag{3.36}$$

where φ is the momentaneous tipping angle defined in equation (3.28). The sine-Gordon equation is integrable and has therefore soliton solutions describing the SIT solutions.

The fundamental 2π-pulse soliton solution of SIT is illustrated in Fig. 3.3, where all quantities are expressed in their full time-domain form. It can be seen how the leading edge of the pulse encounters a two-level system in its ground-state, then slowly lifts the population up to the upper state by stimulating a strong coherence that saturates at a value of 0.5 and switches phase abruptly when the pulse reaches its maximum and the system has been completely inverted. From this point on, the pulse gains energy by stimulated emission through the coherence until the population is completely returned to the ground-state and no net absorption has taken place. In other words, the system is rendered transparent by the strong light pulse impinging on it.

Let us now discuss the consequences of the approximations made to the Maxwell-Bloch equations in order to arrive at the integrable model. The neglect of dephasing

and relaxation restricts the applicability of these equations to pulse durations much shorter than those time-scales. Because of the area theorem, this implies the need for high pulse intensities or, alternatively, low temperatures to achieve long dephasing times. The fulfilment of this condition is, however, much easier than the realisation of a restriction to one-dimensional plane-wave propagation. In free-space the plane-wave approximation often breaks down because of diffraction or self-focusing, especially when strong nonlinearities are involved. Self-focusing of pulses in coherent resonant absorbers is a consequence of the area theorem and the dependence of the group velocity on pulse intensity [95, 96]. The intensity profile of the pulse leads to an increased pulse duration at points of lower intensity, an energy flow towards the higher intensities and finally to pulse breakup, a process well illustrated by numerical simulations [97, 98] and in accordance with experimental results [97, 99]. It has been found that there exists a mathematical soliton solution in a full $3D$-system, a SIT light bullet [23], provided the assumptions on slowly varying envelopes are fulfilled. However, nothing is known about the convergence of an arbitrary light pulse towards this rather complicated spatio-temporal pulse shape and no experimental realisation of this light bullet has been achieved. In a waveguide one-dimensional propagation can be maintained, but this happens at the cost of dispersion and through the imposition of a field profile. Whether SIT solitary waves are possible in the presence of dispersion is part of the investigation presented in Chapters 5 and 6. The problem of a non-constant transverse field profile could be solved at the cost of the strength of the nonlinearity by using a very narrow distribution of the absorbing material, thus ensuring that the field is essentially constant over the absorbing material [26, 27]. A second, more promising solution, the usage of a waveguide with a nanoscopic low-index gap, is presented in Chapter 6.

The assumption that the envelope of the field is slowly varying can be violated either if the pulse has a duration of only a few optical cycles.It has indeed been found that the area theorem is inaccurate for high pulse areas and very short pulses [39]. This result is, however, almost completely academical since any pulse that is short enough to violate the area theorem is certainly broad enough to excite more than one transition in any real atomic or molecular system. Furthermore, if its area is on the order of several π other nonlinear effects, such as high-harmonic generation, may dominate over the dipolar transition. For the purposes of the present thesis, it can safely be assumed that

the duration of the pulse can be as short as is reasonable for the two-level approximation to apply without worrying about the validity of the area theorem.

Thus the theory of SIT predicts the phenomenon of vanishing absorption for specific pulse areas and area-dependent pulse breakup for plane-waves propagating through an absorbing two-level system. These phenomena have been observed in various experiments [10, 100, 101], where a gas-cell was illuminated by a coherent light pulse and strong absorption reduction and pulse breakup were measured. Unequivocal experimental demonstration of SIT can be tricky because absorption saturation and anomalous classical absorption [12] can easily be confused with SIT [102]. Line-width narrowing as sole origin of absorption reduction can be excluded by measuring the spectrum of the transmitted pulses as well as their temporal shape as will be argued in chapter 5 and was mentioned in [102]. Nonetheless most experimental claims of the presence of SIT were not backed by spectral data.

Chapter 4

Collisions of counterpropagating self-induced transparency solitons in three-level systems

In this chapter the collision of counterpropagating simultons [13, 103], SIT solitary waves in three-level media (Figure 4.1) is investigated. Simultons have been found to be similar to SIT solitons in two-level systems [34, 104], but they offer an additional degree of freedom due to the possibility of distributing the excitation between two transitions. Previous numerical studies have been conducted on collisions of solitons in two- and three-level media [35, 36, 51, 105]. Because of the inherent bi-directionality of the method and because no approximations on pulse shape are made, the auxiliary-differential-equation finite-difference time-domain approach to the Maxwell-Bloch equations (see A.3) is ideally suited to treat the problem of counterpropagating simultons.

Using this method it will be shown here that, with the appropriate choice of input parameters, new (secondary) solitary waves are born in the collision process of primary solitary waves in three-level media; an outcome that is not achievable in two-level systems. When a V-type three-level system is used, in which the two transitions are distinguished by the directionality of the dipole matrix elements it is possible to engineer a symmetric input situation. Symmetry here refers to opposing input pulses having the same energy and group velocity but possibly a different polarisation. In this symmetric case the outcome of the collision depends solely on the relative polarisations and group

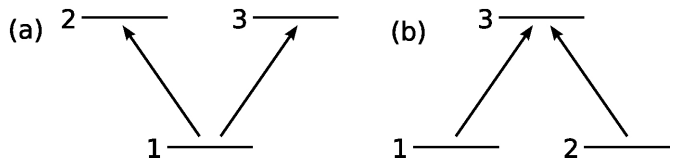


Figure 4.1: Schematics of a (a) V-type and (b) Λ-type degenerate three-level medium.

velocities of the initial pulses.

Before we delve into the numerical results, let us first consider the impact of the relative initial polarisations on the description of the three-level system. Suppose the three-level systems have one dipole matrix element for the transition from ground-state $|1\rangle$ to upper state $|2\rangle$ given by $\boldsymbol{\mu}_{12} = \mu_x$ and the other dipole matrix element given by $\boldsymbol{\mu}_{13} = \mu_y$, so that the dipole matrix elements are orthogonal to each other and of the same magnitude. This is in fact a generic model for a two-fold degenerate transition from a state with total angular momentum $J = 0$ to a state with total angular momentum $J = 1$ since a redefinition of the upper states as superpositions of $|2\rangle$ and $|3\rangle$ can produce any directionality of the two dipole matrix elements in the xy-plane. If we now consider excitation by two pulses with the same polarisation, e.g., both are left-circularly polarised, then they will both interact with the same superposition $|\psi\rangle$ of the upper state and the orthogonal superposition $|\phi\rangle$ of the upper states can be discarded from the analysis [34]. The two simultons should behave as if they were colliding in a two-level system because they do not interact with the third state. If, however, one of the pulses is left-circularly polarised and the other is right-circularly polarised, they will interact with orthogonal superpositions of the upper states and the interaction will have the character of a three-level collision.

The content of this chapter, the bulk of which has been published in [45], is divided as follows: We first study the collision of counterpropagating simultons with parallel relative polarisation in Sec. 4.1 and show that this scenario is indeed equivalent to the collision of simultons in two-level media [36, 51]. Next, simultons with orthogonal polarisations collide in Sec. 4.2 and the parameter space of soliton birth is investigated. The behaviour for arbitrary relative polarisations is studied in Sec. 4.3. The findings are summarised in Sec. 4.4.

4.1 Parallel polarisation

We have established that the collision of simultons with parallel polarisations in a degenerate V-type medium are equivalent to the collision of SIT solitons in a two-level system. Several studies have been devoted to this problem [35, 36, 105]. In [35] Afanas'ev *et al.* study the collision of two identical counterpropagating SIT solitons in the limit of a coherent medium and slowly varying pulse envelopes. The impact of a diffusion of atomic excitation on the collision outcome is also investigated and all results are analysed via the electric field and the language of soliton scattering problems; the atomic parameters are invoked only implicitly. By investigating the dependence of pulse power after collision on the pulse power before collision, Afanas'ev *et al.* found that counterpropagating solitons collide inelastically (energy is lost) and annihilate each other below a critical pulse power, or equivalently group velocity.

Shaw and Shore [36] included a dephasing rate into the Maxwell-Bloch equations and studied the problem of pulse collisions by eliminating the rapid spatial variation in polarisation and inversion with an expansion in powers of $\exp(ikz)$. In their analysis, it becomes clear that the loss of energy in the solitons is partially due to absorption in the interaction region of the colliding pulses but also due to radiation losses. Parametrising the initial conditions on the ratio between the number density of atoms and the number density of photons, they find that, when the density of atoms is 4 times higher (for a 2π-pulse) than the photon density, the pulses annihilate each other in collision and when it is smaller the pulses lose energy but stay solitary waves.

In a recent publication [105] Novitsky investigates the propagation behaviour of few-cycle solitons in a two-level medium using the full Maxwell-Bloch equations. Therein the spectral content of 2π-pulses after collision is analysed with the result that precursor and trailing radiation part leaving the medium are off-resonant and only the main 2π-pulse is resonant. He also studies asymmetric collisions, in which one input pulse is more intense than the other, and finds that the existence of an output pulse in one direction and its parameters can be controlled by the parameters of a counterpropagating pulse as well as by the parameters of the original pulse. Thereby a logic gate could be envisioned; the details of which are not yet discussed in this publication. Note that [105] has been published after the work presented in this chapter was performed and published.

We begin our investigations of the collision of counterpropagating simultons by asserting that the collision of parallel polarised, sech-shaped 2π-pulses is indeed equivalent to the collision of 2π-pulses in a two-level system, thereby also testing the numerical implementation. We used the group velocity, which has already been found in [35] to parametrise the collision regimes, as fundamental parameter describing the input pulse. Dephasing and relaxation rates were neglected on the short time-scales investigated and group velocities were extracted using the method described in the Appendix (A.6). In this limit, the parametrisation in terms of group velocity is accurate down to a few optical cycles, i.e. 2π-pulses of different length in an absorber with different dipole strength show the same collision behaviour if the group velocity is the same. Recall that the group velocity is determined solely by the relation between electromagnetic energy in the pulse and energy deposited in the medium (see equation 3.34) and can be chosen by adjusting the pulse duration while keeping the pulse area constant.

In Fig. 4.2 the results of collisions between pulses with parallel polarisations for two different group velocities are shown. Figure 4.2(a) has been obtained by taking both pulses to be resonant with the same transition in the three-level system, while Fig. 4.2(b) shows the result of a collision between simultons that act on the same coherent superposition of the upper states of the V-type level system. In both cases the initial group velocity is $v_0 = 0.75\,\mathrm{c}$. It can be clearly seen that the resulting pulses are the same in both cases, as expected from the analysis above. The only difference is observed in the occupation densities excited by the pulses; the pulses resonant with the $|1\rangle \leftrightarrow |2\rangle$ transition excite the system to state $|2\rangle$ so that the occupation density $\rho_{22} = 1$ at the maximum of the pulse, whereas the pulses resonant with a coherent superposition of $|2\rangle$ and $|3\rangle$ excite ρ_{22} only to a value of 0.5 since half of the population is excited into state $|3\rangle$. Both collisions result in a population grating in the interaction region, a consequence of the fast variation of local pulse area due to interference of the two pulses that switches inside half a wavelength from constructive to destructive interference. This population grating, and some radiation, subtract energy from the 2π-pulses, so that the group velocities are reduced.

Figure 4.2(c) shows the collision outcome when a lower group velocity of $0.35c$ is used. In accordance with the results of [35, 36] the collision now annihilates the 2π-pulses and only radiation is left. As a greater proportion of the energy of the slow

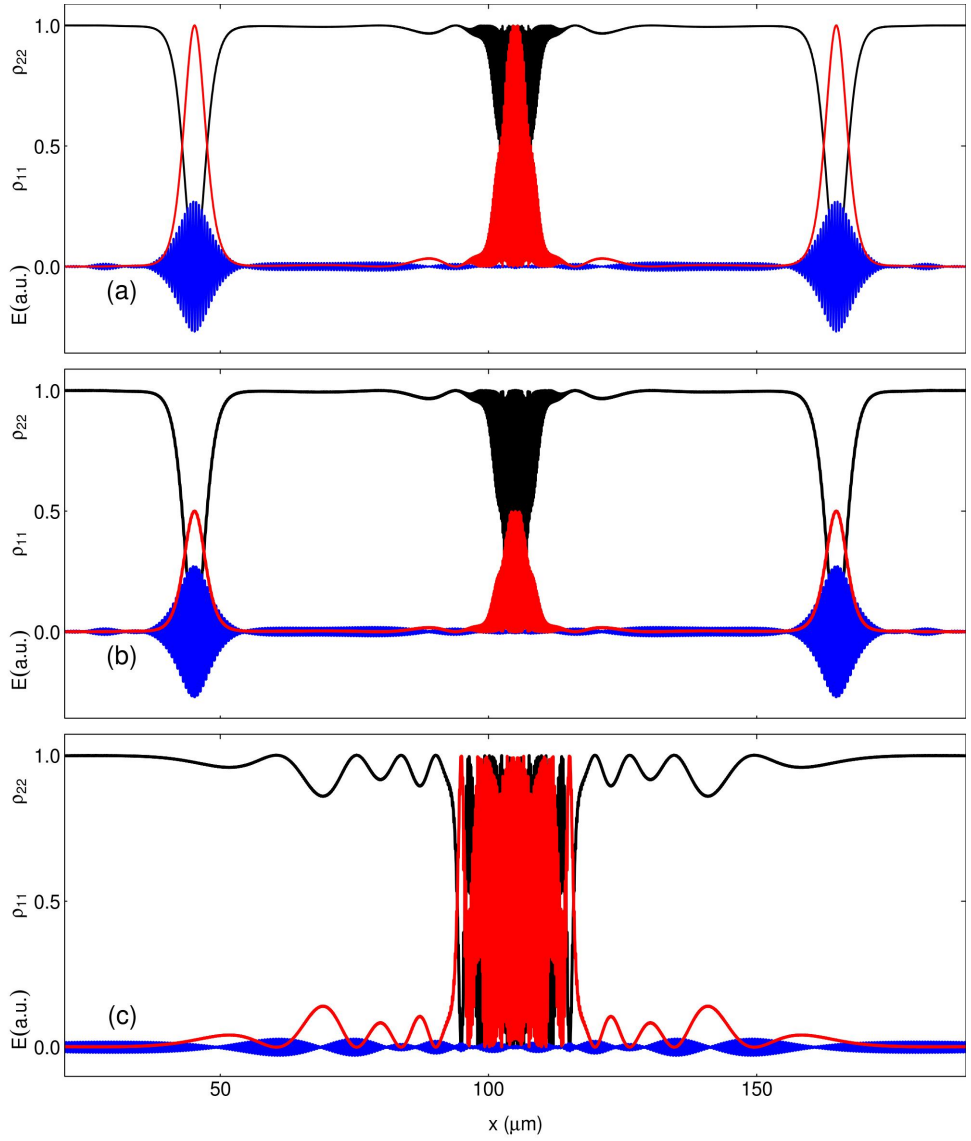


Figure 4.2: ρ_{11} (black line), ρ_{22} (red line) and E (blue line) after the collision of two counterpropagating simultons against distance x for group velocities (a) $v_0 = 0.75\,\mathrm{c}$ and circularly polarised light, (b) $v_0 = 0.75\,\mathrm{c}$ and linearly polarised light and (c) $v_0 = 0.35\,\mathrm{c}$ and circularly polarised light. The material parameters are $\mu = 1.19 \times 10^{-29}\,\mathrm{Cm}$, $n = 8.64 \times 10^{24}\,\mathrm{m}^{-3}$ and $\omega = 3.59 \times 10^{15}\,\mathrm{s}^{-1}$. The basis chosen for the material is circularly polarised.

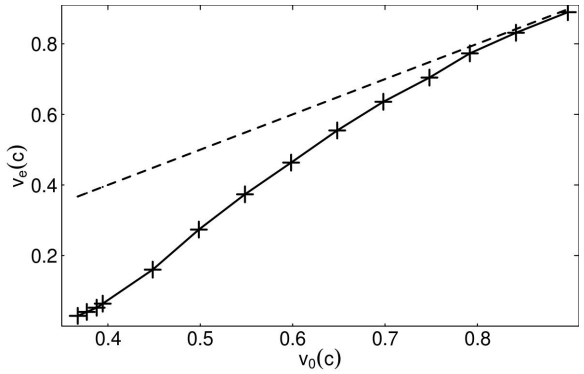


Figure 4.3: Group velocity v_0 before collision versus group velocity v_e after collision. The dashed line ($v_e = v_0$) serves as guide to the eye. Medium parameters are chosen as in Figure 4.2.

2π-pulse is stored in the absorber, the absorber acts more strongly on the light field and the interaction between the pulses, mediated by the two-level system, is much stronger. Although the initial pulses for the slower 2π-pulse are less energetic, the population grating now extends over a larger region; a consequence of the stronger interaction.

We also checked the parametric dependence of the collision outcome on the initial group velocities in terms of the final group velocities (see Fig. 4.3). The critical group velocity, below which the 2π-pulses are annihilated, is given by $v_c = 0.36$. For slightly higher initial group velocities the pulses' group velocities are drastically reduced compared to the initial pulses. With increasing initial group velocity, the impact of the collision on the 2π-pulses decreases until the final group velocity asymptotically reaches the initial group velocity.

In this section we have thus recovered the results of earlier, more approximate studies, proving that parallel polarisation reduces the degenerate V-type three-level system in its interaction with the light field to an effective two-level system. Additionally, we have been able to illustrate more clearly the origin of the energy loss in the two-level collisions in terms of an induced population grating and the creation of off-resonant radiation.

4.2 Orthogonal polarisation

In the previous section it was shown that simultons with parallel polarisations, acting on the same transition in a degenerate V-type three-level system, show the collision behaviour of solitons in a two-level system. If we now consider collisions of counter-

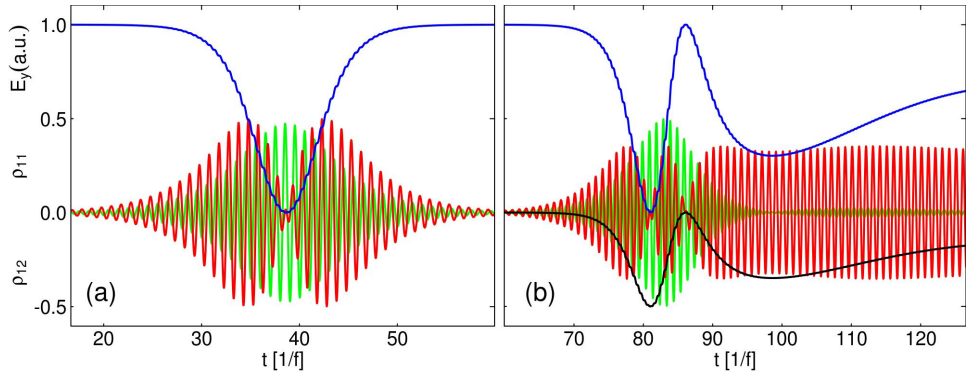


Figure 4.4: (a) Time evolution of $\mathrm{Re}(\rho_{12})(z_0)$ (red line), $\rho_{11}(z_0)$ (blue line) and $E_x(z_0)$ (green line) for an undisturbed simulton of group velocity $v_0 = 0.75\,\mathrm{c}$ in a three-level system. (b) Time evolution of $\mathrm{Re}(\rho_{12})$ (red line), ρ_{11} (blue line), E_y (green line) and $\mathrm{Re}(\rho_{23})$ (black line) at the symmetry point of a collision between two counterpropagating simultons of group velocity $v_0 = 0.75\,\mathrm{c}$, one resonant with the $|1\rangle \leftrightarrow |2\rangle$ transition (E_x), the other resonant with the $|1\rangle \leftrightarrow |3\rangle$ transition (E_y).

propagating simultons with orthogonal polarisations, we expect that the outcome of the collisions is different. Before looking at numerical results, let us first analyse the three-level Maxwell-Bloch equations (equations (3.12)) to understand where the interaction between pulses with orthogonal polarisations differs from the interaction between pulses with parallel polarisations.

We start by assuming two counterpropagating light pulses $E_x^+(z,t)$ and $E_y^-(z,t)$ with orthogonal polarisations and area 2π following a, initially independent, wave equation

$$\frac{\partial^2 E_x^+}{\partial z^2} - \frac{1}{c^2}\frac{\partial^2 E_x^+}{\partial t^2} = \frac{2n\mu}{\epsilon_0 c^2}\frac{\partial^2 \mathrm{Re}(\rho_{12})}{\partial t^2} \tag{4.1}$$

$$\frac{\partial^2 E_y^-}{\partial x^2} - \frac{1}{c^2}\frac{\partial^2 E_y^-}{\partial t^2} = \frac{2n\mu}{\epsilon_0 c^2}\frac{\partial^2 \mathrm{Re}(\rho_{13})}{\partial t^2}\,. \tag{4.2}$$

Here, the homogeneous three-level system is defined so that the dipole moment of the transition $|1\rangle \leftrightarrow |2\rangle$ points in the x-direction and the dipole moment of the transition $|1\rangle \leftrightarrow |3\rangle$ points in the y-direction. As long as the pulses do not overlap and backscattering and dephasing are negligible, they will propagate as undisturbed solitary waves.

When the pulses overlap, the polarisations $\mathrm{Re}(\rho_{12})$ and $\mathrm{Re}(\rho_{13})$ differ from the values they attain for a single 2π-pulse giving rise to all light-light interaction phenomena. Figure 4.4 illustrates the influence of the solitary wave collision on the polarisations. In Fig. 4.4(a) the occupation density ρ_{11} of the ground-state $|1\rangle$ is plotted along with

the polarisation $\mathrm{Re}(\rho_{12})$ and the electric field E_x^+ for an undisturbed solitary 2π-pulse. All quantities are symmetric in time. Crucially the occupation density ρ_{11} returns to its original value of 1, meaning that the system has returned to its ground-state. The polarisation reaches a maximum value when $\rho_{11} = 0.5$ and inverts its phase when $\rho_{11} = 0$, thereby switching from absorption to re-emission. If we now look at Fig. 4.4(b), huge differences are obvious as neither polarisation nor occupation densities are symmetric any more. The presence of the second pulse, E_y^-, exciting the transition $|1\rangle \leftrightarrow |3\rangle$ disturbs the polarisation ρ_{12}, thereby altering the dynamics of E_x^+. The interaction between the pulses takes place via the cross-polarisation ρ_{23} [black dashed line in Fig. 4.4(b)] and also via the occupation density ρ_{11} that is now excited to states $|2\rangle$ and $|3\rangle$ instead of only to state $|2\rangle$. A consequence of the interaction is that a long-lived polarisation, $\mathrm{Re}(\rho_{12})$, is present after the original pulses have passed the interaction region. As we will see below, this long-lived polarisation gives rise to a secondary 2π-pulse.

Let us understand the above by looking at the additional terms that appear in the second derivative of $\mathrm{Re}(\rho_{12})$ due to the interaction. To this end, we replace the derivatives on the RHS of equation 4.1 by inserting equations (3.12)

$$\begin{aligned}\frac{\partial^2 \mathrm{Re}(\rho_{12})}{\partial t^2} &= \frac{\partial}{\partial t}(\mathrm{Im}(\rho_{12})\omega - \Omega_y^- \mathrm{Im}(\rho_{23})) \\ &= -(\omega^2 + (\Omega_y^-)^2)\mathrm{Re}(\rho_{12}) + \omega\Omega_x^+(\rho_{11} - \rho_{22}) - \omega\Omega_y^- \mathrm{Re}(\rho_{23}) \\ &\quad - \frac{\partial \Omega_y^-}{\partial t}\mathrm{Im}(\rho_{23}) + \Omega_y^-\Omega_x^+ \mathrm{Re}(\rho_{13})\,. \quad (4.3)\end{aligned}$$

Here, we already see the presence of several terms which are only due to interaction. Firstly, the resonance frequency of $\mathrm{Re}(\rho_{12})$ is shifted due to the Rabi frequency of the $|1\rangle \leftrightarrow |3\rangle$ transition Ω_y^-. Secondly, several driving terms are introduced which depend on Ω_y^- and the cross-polarisation ρ_{23} or the product of both Rabi-frequencies and the polarisation of the second optical transition.

Additionally, the densities ρ_{11} and ρ_{22} are now driven differently than in the undisturbed case. We can write these terms down in their integral form together with the cross-polarisation ρ_{23}. It is then possible to identify further terms which are due to the interaction of two counterpropagating pulses and those which are present in the case of a single pulse tuned to only one transition. The latter terms are the ones giving rise to

self-induced transparency and the former are the ones responsible for the pulse breakup

$$\rho_{11}(z,t) = 1 - \int_0^t 2\Omega_x^+(z,t')\mathrm{Im}(\rho_{12}(z,t'))dt' - \int_0^t 2\Omega_y^-(z,t')\mathrm{Im}(\rho_{13}(z,t'))dt' \tag{4.4}$$

$$\rho_{22}(z,t) = \int_0^t 2\Omega_x^+(z,t')\mathrm{Im}(\rho_{12}(z,t'))dt' \tag{4.5}$$

$$\mathrm{Re}(\rho_{23}(z,t)) = \int_0^t (\Omega_y^-(z,t')\mathrm{Im}(\rho_{12}(z,t')) + \Omega_x^+(z,t')\mathrm{Im}(\rho_{13}(z,t')))dt' \tag{4.6}$$

$$\mathrm{Im}(\rho_{23}(z,t)) = \int_0^t (\Omega_y^-(z,t')\mathrm{Re}(\rho_{12}(z,t')) - \Omega_x^+(z,t')\mathrm{Re}(\rho_{13}(z,t')))dt' \,. \tag{4.7}$$

As we can see there are a lot of terms that are only present in the interaction case, which are all of a similar magnitude, so that it is impossible to pin the interaction down to a particular term. In the two-level case, however, no cross-polarisations exist and the pulse annihilation can be attributed to an interaction via the occupation densities ρ_{11} and ρ_{22}. For orthogonal pulses, interaction via the occupation densities is present but not as strong, since the densities are driven into different upper states.

Because of the complexity of the interaction terms, the pulse interaction in the Maxwell-Bloch equations cannot be understood analytically. Therefore we have to resort to numerical simulations for the three-level collisions. In this section, we only consider symmetrical situations, in which the pulse velocities of leftward propagating and rightward propagating pulses are identical. Note that the results presented can also be obtained in a Λ-type three-level system, if the initial occupation density is evenly distributed between the degenerate lower states. The most important result of the numerical simulations is the existence of two distinct regimes in the collision of orthogonal simultons that are parametrised by the group velocities of the initial pulses. For high initial group velocities additional 2π-pulses are born in the collision, whereas for low group velocities the pulse splits into breathers; pulses that are unable to invert the medium completely although they propagate with a similar group velocity as 2π-pulses of the same amplitude. The critical group velocity above which new solitary waves are born is given by $v_c \approx 0.62\,\mathrm{c}$.

Figure 4.5 presents the spatio-temporal dynamics of pulse collisions for four different initial group velocities in terms of the occupation density ρ_{11} of the ground-state of the three-level system. From Fig. 4.5(a) we see how two counterpropagating simultons

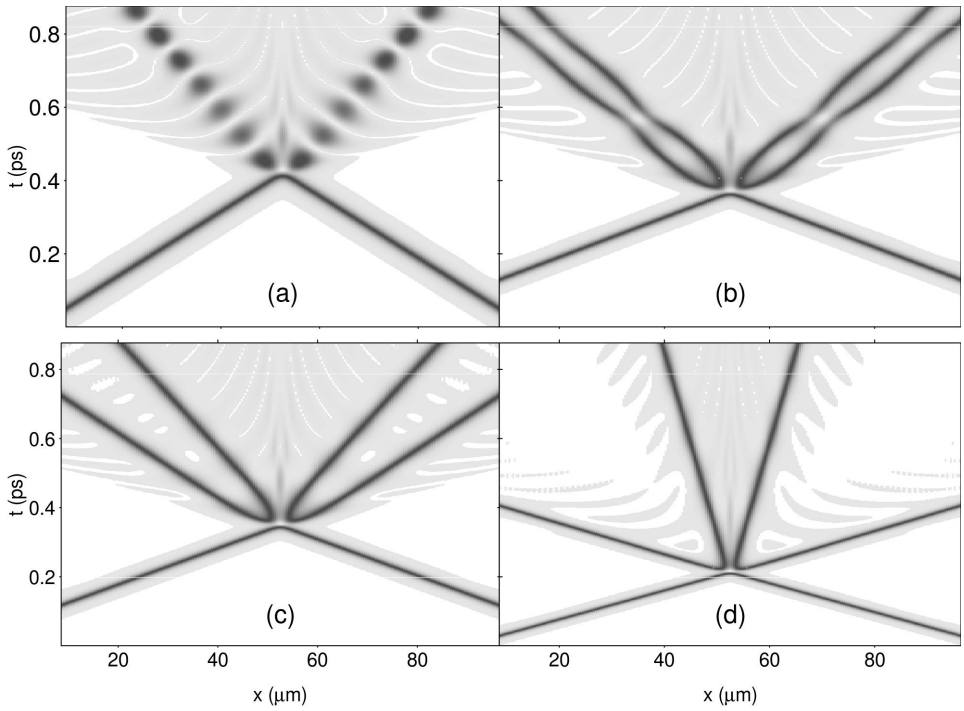


Figure 4.5: Linear grey-scale plot of the occupancy of the lowest level ρ_{11} during the collision of circularly polarised pulses with group velocities of (a) $v_0 = 0.4\,\mathrm{c}$, (b) $v_0 = 0.62\,\mathrm{c}$, (c) $v_0 = 0.64\,\mathrm{c}$ and (d) $v_0 = 0.8\,\mathrm{c}$. Black corresponds to $\rho_{11} = 0$ and white to $\rho_{11} = 1$. The material parameters are $\mu = 2.38 \times 10^{-29}\,\mathrm{Cm}$, $\rho = 8.64 \times 10^{24}\,\mathrm{m}^{-3}$ and $\omega = 3.59 \times 10^{15}\,\mathrm{s}^{-1}$.

with initial group velocity $v_0 = 0.4\,\mathrm{c}$ collide and disperse into breathers. This stands in contrast to the collisions in two-level systems in which the initial 2π-pulses are reshaped down to group velocities of $v_0 = 0.36\,\mathrm{c}$ and only below this group velocity do they annihilate each other. The other important difference to the two-level case is, that no population grating is left in the interaction region. All the pulse energy remains in the light field.

From a group velocity of $v_0 \approx 0.62\,\mathrm{c}$ upwards [see Fig. 4.5(b)], we observe the birth of secondary solitary waves. For the initial group velocity of $v_0 = 0.62\,\mathrm{c}$ the pulses after collision initially struggle to separate, but their group velocities are different enough for them to finally stay apart. In this case, close to the critical velocity the energy of the initial pulse is almost equally distributed between the two collision products with some energy dissipated as radiation (the interaction between the solitary waves is not completely elastic). In fact, it is reasonable to assume that the equidistribution of energy between the collision products is the reason for the creation of breathers below a group velocity of $v_0 \approx 0.62\,\mathrm{c}$. The collision products are unable to separate in space, since the group velocity in a given medium is a function of only the pulse energy and, with degenerate pulse energies of the copropagating collision products, a breather is formed.

In Figs. 4.5(c) and 4.5(d) more energetic and, consequently, faster initial pulses are injected into the three-level medium. Now, the collision allows for a clear separation between the collision products and we see that the faster the initial pulses, the faster the first collision product and the slower the new, secondary solitary wave. This is a manifestation of a decreasing interaction strength between the counterpropagating pulses, when the pulse intensity is increased. The higher the initial pulse energy the less energy is separated from it in the collision process. Therefore, the less energy is available to form the new, secondary solitary waves. One can understand this by remembering that the impact of the material polarisation on the electric field is reduced considerably if the field is more intense, since the polarisation is limited to a maximum value of $\mu N/2$.

The dependencies of the group velocities v_1 and v_2 of the two collision products on the initial group velocity are shown in Fig. 4.6. For pulses that are very close in group velocity, it gets progressively more difficult to decide if they form two pulses or one pulse. It also becomes more difficult to extract the group velocity in the presence of considerable radiation, so that the dependencies are not continued down to an initial

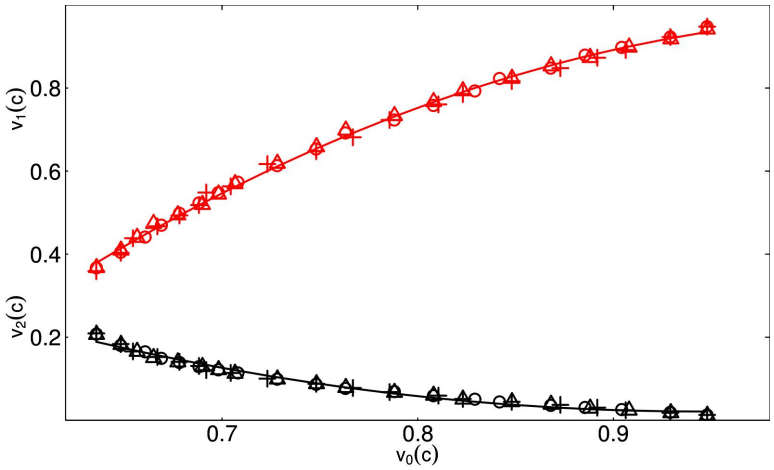


Figure 4.6: Group velocities of v_1 (red) of primary pulses and v_2 (black) of secondary pulses after collision as a function of the group velocity of the initial pulses. Different symbol stand for different values of dipole moment μ and medium density n and the lines represent polynomial fits of second order to the data.

group velocity of $v_0 = 0.62\,\mathrm{c}$. Likewise, a very slow solitary wave is very narrow in real space. As a consequence, a very slow pulse encounters appreciable backscattering from a sudden change in the refractive index due to a sudden change in occupation densities and it is not stable. Therefore, very slow solitary waves could not be measured and the analysis of the collisions has only been performed up to initial group velocities of $0.95\,\mathrm{c}$.

As a first result, we can deduce that the initial group velocities are indeed the only parameters that determine the outcome of the collision, since a variation in medium parameters does not matter as long as the group velocities are the same. Consequently, it is to be expected that the results presented here are not only valid for the femtosecond pulses studied but also for much longer pulses, as long as the pulse duration is much shorter than relaxation and dephasing times of the medium. The slight deviations between the different parameter sets are probably due to inaccuracies in the extraction process.

Secondly, we see from the accuracy of a polynomial fit of second order that the dependencies of the final group velocities on the initial group velocities are nearly parabolic with a better matching for the fast than for the slow pulses. For the fast pulses the dependency of the final group velocity on the initial group velocity can be approximately expressed as $v_1 = -3.33\,v_0^2 + 7.06\,v_0 - 2.76$, whereas for the slower pulse the polynomial fit results in $v_2 = 1.755\,v_0^2 - 3.32\,v_0 + 1.59$ (here all velocities are given as fraction of the

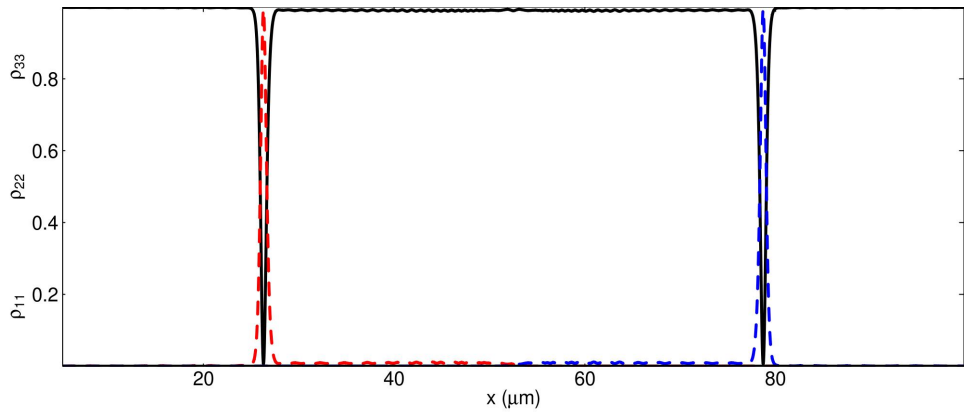


Figure 4.7: Occupancies ρ_{11} (solid black line), ρ_{22} (dashed red line) and ρ_{33} (dashed blue line) of a three-level medium with dephasing long after the collision of two simultons with orthogonal polarisation. Parameters used: $\lambda = 525\,\mathrm{nm}$, $\mu = 2.8 \times 10^{-29}\,\mathrm{C\,m}$, $n = 1.87 \times 10^{24}\,\mathrm{m}^{-3}$, $\tau = 2.66 \times 10^{-15}\,\mathrm{s}$ (4 cycle pulse) and $\gamma_{12} = \gamma_{13} = 57\,\mathrm{ns}^{-1}$, resulting in a primary pulse velocity of $v_0 = 0.863\,\mathrm{c}$.

speed of light). Extending these formulas into the regime where considerable radiation and a continued interaction between the pulses make extraction of the group velocities impossible, one finds a crossover point at $v_0 = 0.59\,\mathrm{c}$. The fit is, however, not very good any more in this regime. Indeed, when approaching the critical velocity ($v_c \approx 0.62\,\mathrm{c}$), the difference between fit and measured result increases drastically. On the other end of the parameter space, when the initial group velocity approaches the speed of light, the interaction becomes almost negligible. Only very slow pulses with low energies are separated from the main pulses and the main pulses are almost unperturbed.

The results presented until now have been obtained in the absence of dephasing. When a small dephasing rate – a dephasing time much longer than the pulse duration – is added, it is usually assumed that the light propagation is not affected. The same is true for the collision processes investigated here but with a caveat. As we see from Fig. 4.6, collisions of pulses with very short duration (high group velocity) give rise to long pulses (small group velocity). Therefore it is not guaranteed that, when the duration of the initial pulse is much smaller than the dephasing time, the same will be true for the secondary 2π-pulses born in the collision process.

Figure 4.7 presents an example of the collision of very fast 2π-pulses that gives rise to long 2π-pulses, for which dephasing cannot be neglected any more. These secondary pulses are then quickly absorbed inside the medium and thereby they leave an electronic

excitation behind that is confined to a very small region. The possibility of achieving such selective excitations has been studied for three-level Λ-media [42, 104], but no such scheme has been devised for a V-type medium.

To summarise this section, we remark that the collision of solitary waves with orthogonal polarisation inside a degenerate three-level medium is qualitatively different from the collision of solitary waves with parallel polarisation. In the latter process, the new phenomenon of birth of SIT solitary waves has been observed numerically for high initial group velocities. Interestingly, the group velocities of the collision products depend only on the initial group velocities of the solitary waves and not on any other parameters. It is possible to think of the presented results in terms of control of an incoming pulse by collision with a counterpropagating pulse. Then, one can interpret the results such that a counterpropagating 2π-pulse imparts onto the, initially polarisation insensitive, medium a polarisation sensitivity for the incoming 2π-pulse. In other words, if a 2π-pulse encounters a counterprogating 2π-pulse in the considered three-level medium its propagation characteristics are polarisation dependent although the medium itself is polarisation insensitive. If the counterpropagating solitary wave is linearly polarised the medium becomes birefringent for the incoming solitary wave and if the counterpropagating solitary wave is circularly polarised the medium becomes chiral. In the next section we consider the collision of solitary waves with arbitrary relative polarisation and thereby fathom the polarisation sensitivity of the medium in the presence of a 2π-pulse.

4.3 Arbitrary relative polarisation

Here, the collision characteristics between solitary waves of arbitrary relative polarisation are studied with the expectation of an intermediate behaviour between the effective two-level and genuine three-level case. For the purpose of this investigation the polarisation of one of the 2π-pulses is fixed to E_y-polarisation, whereas that of the other 2π-pulse has a variable angle α relative to the y-axis. The collision outcome is given in Fig. 4.8, for four exemplary group velocities and several polarisation angles, in terms of the velocity of the faster (or only) collision product.

For $\alpha = 0^\circ$ we have the two-level case, while the genuine three-level case of orthogonal polarisations is recovered for $\alpha = 90^\circ$. From Fig. 4.8 we see that there are two regimes

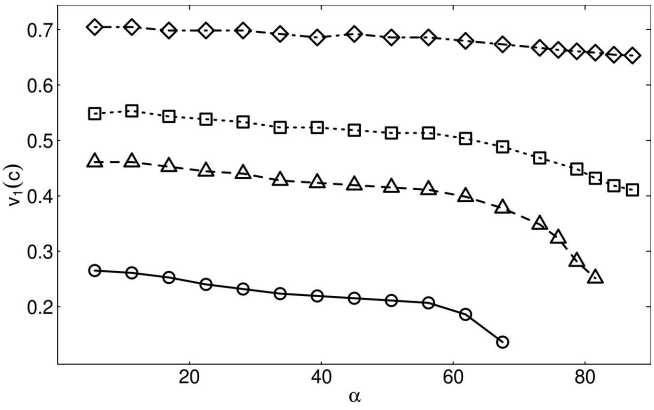


Figure 4.8: Group velocity v_1 after collision plotted over angle α (in degrees) between polarisations of counterpropagating simultons for initial group velocities of $v_0 = 0.75\,\mathrm{c}$ (diamonds), $v_0 = 0.65\,\mathrm{c}$ (squares), $v_0 = 0.6\,\mathrm{c}$ (triangles) and $v_0 = 0.5\,\mathrm{c}$ (circles).

in the dependency of the final group velocity on the polarisation angle. In the first regime, reaching up to high angles between the polarisations, the group velocity decreases approximately linearly with the polarisation angle. This regime is followed by a sharp drop in the final group velocities. The location of the drop is around $\alpha_d = 60^\circ$ for all depicted initial group velocities. At polarisation angles above the drop angle, slow secondary solitary waves are created. Hence, more energy is taken away from the primary solitary waves. Generally speaking, the collision behaviour is closer to the two-level case for angles up to α_d and the three-level behaviour is approximated beyond this point, although secondary solitary waves are created for lower group velocities than in the case of orthogonal polarisations.

Take for example the collision outcomes at $v_0 = 0.6\,\mathrm{c}$. In the previous sections we have discovered that, for this initial group velocity, parallel polarised solitary waves will propagate almost unaffected, whereas in the genuine three-level case (with orthogonal polarisation) the solitary waves break up into breathers. In the angle dependent study we find that the pulses split into breathers only above $\alpha_b \approx 82^\circ$. Between α_d and α_b secondary waves are created. In the case of $v_0 = 0.5\,\mathrm{c}$ we have $\alpha_b \approx 70^\circ$ leading to a small window of creation of secondary solitary waves. Looking at the data for $v_0 = 0.75\,\mathrm{c}$ (the highest group velocity investigated here), it seems as if the polarisation angle does not matter much to the collision outcome; again, however, we have secondary solitary wave creation above $\alpha_d \approx 60^\circ$ so that for $\alpha < \alpha_d$ the energy lost by the initial solitary wave is deposited in the medium in form of a population grating, whereas for

$\alpha > \alpha_d$ the energy lost is partly used for the creation of a new, secondary solitary wave. Thus, varying the relative polarisation between the counterpropagating solitary waves in a degenerate three-level system allows for a steady interpolation between the different collision outcomes.

4.4 Conclusions

In this chapter the finite-difference time-domain method was employed to analyse the collision of counterpropagating simultons of pulse area 2π in a one-dimensional setting. We have found that simulton birth can occur in a three-level medium if the input pulses are resonant with orthogonal transitions and are faster than a critical group velocity of $v_0 \approx 0.62\,\mathrm{c}$ in the symmetric case. For pulses resonant with parallel transitions the medium is reduced to a two-level system in its interaction with the light field and collisions result in a population grating in the interaction region. This population grating is a result of an oscillation of the effective pulse area in space that stems from the changing phase-relation between the colliding pulses at different locations along the one-dimensional interaction region.

We showed in detail the dependencies of output pulse velocities versus input pulse velocities for the symmetric input pulse case. Higher initial pulse velocities of the orthogonal simultons resulted in slower secondary pulses being created in the collision process. This indicates that the disturbance created by the collision is greater if the initial pulses are slower, which leads to a larger part of the pulse being separated from the initial pulse. Slow collision products are vulnerable to dephasing and backscattering processes that lead to a deposition of inversion close to the interaction region. The Bloch equations for a three-level system were analysed to find the origin of the different collision outcomes. For parallel simultons interaction is mediated only by the inversion, whereas for orthogonal simultons the interaction mediated by the cross-polarisation becomes important too. Intermediate behaviour between the two-level and three-level case has been found in the interaction when the angle of relative polarisation was varied, as well as when the detuning for a non-degenerate three-level system with the same directionality of the dipole matrix elements was investigated.

The above study has been performed in a one-dimensional propagation approxima-

tion equivalent to a plane-wave approximation. To study the collision behaviour in a realistic system such as a gas-filled hollow core fibre [106] or waveguide, the proper conditions on solitary propagation in resonantly absorbing waveguides have to be formulated first. In the next chapter we make a crucial step towards this goal by investigating whether SIT solitons can still exist if the input pulse is chirped. As seen in Sec. 2.2 waveguides have a dispersion relation that ensures that different frequencies propagate at different speeds resulting in chirped pulses. If chirp (which can be considered as accumulated dispersion) can be compensated, it is not unreasonable to expect that waveguide dispersion can also be compensated directly by the transparent interaction with resonant absorbers. Self-induced transparency in nanophotonic waveguides and collisions of counterpropagating solitons therein will then be demonstrated numerically in chapter 6.

Chapter 5

Dynamic transition from complete population transfer to self-induced transparency

In this chapter the propagation of chirped plane-wave pulses through resonant two-level systems is investigated. The results presented here have also been published in [56]. As discussed in Section 3.3, the Maxwell-Bloch equations allow for solitary propagation due to a re-emission into the pulse if the pulses are unchirped and exceed an area of π. For chirped pulses, however, the area theorem is not directly applicable. Numerical studies on the transformation of chirped pulses into 2π-pulses using static techniques, such as conversation laws [107] or the inverse scattering transform [108], have been performed. They found that the critical area for soliton formation depends not only on the magnitude of the applied chirp but also on the pulse shape (unlike for unchirped input pulses). Because of the static nature of the applied techniques in [107, 108], dynamic aspects of the transition from chirped pulses to unchirped solitary waves could not be investigated. Also, the state of the two-level system after passage of the pulses is not considered.

While the studies [107, 108] where constrained to moderately chirped pulses, the interaction of strongly chirped pulses with absorbing two-level systems is of fundamental interest, since it allows for robust population transfer by adiabatic rapid passage (explained in Section 3.2). In [53, 54] it has been found experimentally and by numerical

calculations that strongly chirped pulses impinging on a dense ensemble of absorbers are capable of transferring the two-level population only at entrance into the medium. The fact that the achieved inversion quickly decreases with propagation distance is attributed to a combined effect of absorption of the pulse and subsequent stimulated emission.

Here, the propagation of chirped pulses through absorbing two-level systems is studied from the perspective of self-induced transparency theory. In so doing the formation of unchirped solitary waves out of the initially chirped pulses is identified as the main limitation on adiabatic rapid passage in dense ensembles. Although absorption of the pulse energy is indeed important in limiting the inversion, it is foremost the pulse reshaping that finally renders the medium transparent to the pulse. In addition, some of the energy originally deposited in the medium is transformed into 2π-pulses by stimulated emission processes. The investigation performed here focuses on linearly chirped Gaussian input pulses, since an analytic Fourier transform of those pulses can be found. Using this Fourier transform, it is possible to analytically determine the relation between the electric field magnitude at the center frequency and the time-domain area of the pulses, enabling a convenient choice of parameters.

In the first Section of this chapter, Section 5.1, the dynamics of adiabatic rapid passage are illustrated in full time-domain, where the manifestation of adiabatic following is expressed by the phase relationship between exciting field and induced polarisation. Section 5.2 maps and compares the regimes for soliton creation in dense ensembles and complete population transfer (CPT) for varying chirp and pulse amplitude. Section 5.3 then explores the propagation of moderately chirped pulses in a dense ensemble of two-level systems. In this regime we find that the chirp is rapidly lost and that the pulses reshape into SIT solitons with intensity-dependent group velocity. Propagation of strongly chirped pulses well inside the CPT regime is investigated in Sec. 5.4. Here, the pulses induce CPT for the first few wavelengths, undergo substantial absorption at the resonance frequency, and shed radiation while reshaping into solitary waves. The main findings of the Chapter are summarised in Section 5.5.

5.1 Adiabatic rapid passage in full time-domain

This section is intended to illustrate the mechanism of adiabatic rapid passage (ARP) in full time-domain. To this end, a linearly chirped Gaussian pulse characterised by a time dependence of the electric field

$$E(t) = E_0 \cos([\omega_0 + \alpha(t - t_0)][t - t_0]) \exp(\frac{t - t_0}{2\tau^2}) \,, \tag{5.1}$$

is used, with α being the magnitude of the linear temporal chirp. In the frequency domain the field is given by

$$\tilde{E}(\omega) = \tilde{E}_0 \exp\left[-\frac{(\omega - \omega_0)^2}{2\Gamma^2} + i\alpha' \frac{(\omega - \omega_0)^2}{2}\right], \tag{5.2}$$

where α' denotes the magnitude of the linear spectral chirp.

For a linearly chirped Gaussian pulse one can define a dimensionless chirp that quantifies the change in instantaneous frequency. The requirement for ARP on the linear chirp is then written as $|\alpha|\,\tau^2 = |\alpha'|\,/\Gamma^2 \gg 1$. In order to achieve ARP, the pulse must also be intense enough to produce the avoided crossing in the adiabatic states. This condition on the intensity is best expressed via the pulse area, familiar from SIT, which is usually defined in time-domain by the integral over the temporal envelope of the electric field

$$\theta_t = \mu \int_{-\infty}^{\infty} \mathrm{d}t E_0 \exp\left[\frac{t - t_0}{2\tau^2} - i\alpha\frac{t^2}{2}\right]. \tag{5.3}$$

This time-domain area does, however, demand the definition of a pulse envelope, which can be negative depending on the pulse phase. Hence, it is not always straightforward to establish the time-domain pulse area experimentally. Another, here more useful, definition of the pulse area can be given in frequency domain, denoted by θ_ω. If we demand that the two definitions coincide for transform-limited (unchirped) pulses θ_ω is given by [102]

$$\theta_\omega = 2\mu\tilde{E}_0\tau/\hbar \,. \tag{5.4}$$

As a consequence, for chirped pulses one has $\theta(\omega) \leq \theta_t$. From Figure 4 of [52] it can be seen that $\theta_\omega \gg \pi$ provides a formulation of the adiabaticity condition in terms of frequency domain pulse area.

Figure 5.1, which compares excitation by unchirped, moderately chirped, and strongly chirped pulses with a frequency domain area of 2π shows that adiabatic following manifests in full time-domain by a polarisation that stays almost exactly in phase with the excitation pulse at all times. An unchirped 2π-pulse, in contrast, induces a polarisation that is always exactly out of phase with the exciting field and exhibits a phase-jump of π when absorption switches to emission in the middle of the pulse. For a moderately chirped pulse the behaviour switches from an in-phase excitation at the leading edge of the pulse to an out-of phase excitation at the tail of the pulse. This indicates that the adiabatic state could not be followed by the electronic states. The same happens when the excitation is not intense enough and the adiabaticity condition is not fulfilled because of an insufficient Rabi frequency. In the latter case no complete Rabi oscillation is possible.

5.2 The connection between pulse area theorem and adiabaticity condition

In this section the connection between the pulse area of SIT theory and the adiabaticity condition on CPT is explored. For transform-limited pulses the area theorem [equation (3.32)] applies to frequency-domain area as well as time-domain area. If the pulses are chirped, however, it does not apply to either definition of the area. From a practical point of view it is easiest to think of chirped pulses as transform-limited pulses that have been stretched due to a linear process, such as propagation through a dispersive waveguide or a dispersive grating. In this way the pulse can be prepared with a specific area in frequency-domain θ_ω. Because of the ease (experimentally as well as numerically) of determining θ_ω as the maximum spectral amplitude, it will in the following be used as a pulse parameter to be varied.

As shown above, the other important parameter that determines the success of a Gaussian pulse in transferring the population of a two-level system is the chirp of the pulse. The dimensionless linear chirp $\alpha\tau^2 = \alpha'/\Gamma^2$ and the pulse area taken together completely determine the final population inversion achieved by the exciting Gaussian pulse. Figure 5.2 shows a numerically calculated contour-plot of the inversion reached in a single atom that is excited by a linearly chirped Gaussian pulse. Herein, dimensionless

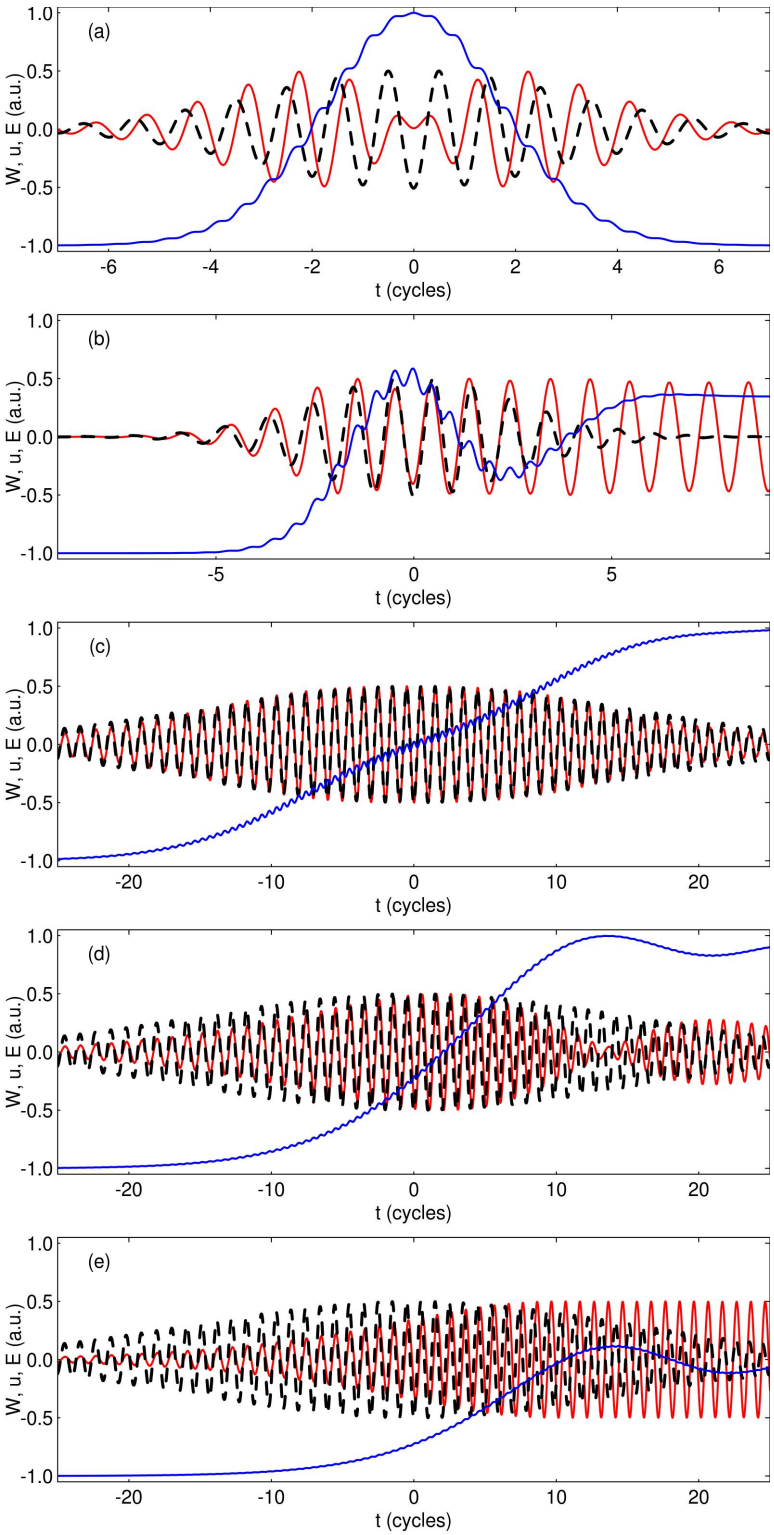


Figure 5.1: Evolution of a two-level system driven by a pulse with different values of frequency domain pulse area and chirp (a) $\alpha\tau^2 = 0$, $\theta_\omega = 2\pi$, (b) $\alpha\tau^2 = 2$, $\theta_\omega = 2\pi$, (c) $\alpha\tau^2 = 5$, $\theta_\omega = 2\pi$, (d) $\alpha\tau^2 = 5$, $\theta_\omega = \pi$, and (e) $\alpha\tau^2 = 5$, $\theta_\omega = \pi/2$. The inversion W is given by the solid blue line, the real part of the polarisation by the solid red line and the electric field by the dashed black line.

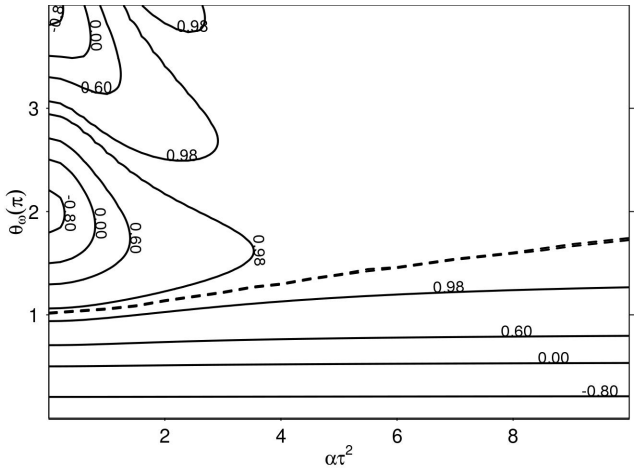


Figure 5.2: Contour-plot of the final inversion W of a single two-level system after excitation by a pulse with area θ and dimensionless chirp $\alpha\tau^2$. Above the dashed line, 2π-pulses are created in a dense ensemble of two-level systems. Note, that the contour-plots in the negative chirp regime are an exact mirror image of the positive chirp regime (compare Fig. 4 of [52]).

linear chirp and the frequency-domain area are varied. The contour-plot shows that pulses with frequency-domain area $\theta_\omega \gg \pi$ and a dimensionless linear chirp $\alpha\tau^2 > 4$ invert the population to an accuracy of more than 99%. Moreover it is noted, that the beginning of the regime of complete population transfer in terms of θ_ω depends only weakly on the applied chirp and the delineation is close to $\theta_\omega = \pi$. Considering that a transform-limited pulse also needs a pulse area of π to achieve complete inversion, it is not surprising that adiabatic rapid passage needs a pulse area that is at least as high.

Chirped plane-wave pulses in a dense ensemble of two-level systems can develop into 2π-pulses if their area is high enough. Unfortunately, there exists no general pulse area theorem for chirped pulses and the critical area for chirped pulses has to be found by performing numerical calculations for each pulse shape and chirp magnitude independently. The result of such propagation studies for linearly chirped Gaussian pulses is also given in Figure 5.2 to provide an easy comparison to the regime of complete population transfer; pulses with an area larger than the area indicated by the dashed line develop into one or several 2π-pulses, while pulses with a lower area develop into pulses of zero area. For the numerical integration of the one-dimensional Maxwell-Bloch equations a dephasing rate of $0.001 f_0$, a two-level density of $N = 10^6\lambda^{-3}$ and a dipole length of $d = 10^{-4}\lambda$ were assumed. The delineation given in Figure 5.2 is not exact, since it is

difficult to distinguish a very slow 2π-pulse from background radiation in the presence of dephasing and backscattering leading to pulse decay. Comparing the regime of complete population transfer in an isolated two-level system and the regime of creation of 2π-pulses in a dense ensemble, it is immediately obvious that pulses, which fulfil the adiabaticity condition, reshape into solitary waves while propagating through the dense ensemble. The comparison between the conditions for ARP and the condition for soliton creation thus reveals the deep connection between the phenomena of SIT solitons and ARP.

In the following section the dynamics of the reshaping process of chirped pulses in resonant absorbers are investigated. As a first step, moderately chirped pulses with a chirp value of $\alpha\tau^2 = 1$, insufficient for robust CPT via ARP (Sec. 5.3) are studied. For these parameters the creation of unchirped solitary waves and radiation is observed and the difference between frequency-domain pulse area and time-domain pulse area for chirped pulses is illustrated. Strongly chirped pulses with $\alpha\tau^2 \gg 1$ propagating through a dense ensemble of two-level systems are investigated in Sec. 5.4. Thereby one finds the dynamic transition from CPT to solitary propagation of one or several solitary waves.

5.3 Resonant propagation of moderately chirped pulses

Moderately chirped pulses with a dimensionless chirp on the order of $\alpha\tau^2 \approx 1$ are neither capable of robust CPT nor do they achieve a full Rabi oscillation of the Bloch vector. Since the inversion plotted in Fig. 5.2 does not return to -1 for such pulses, some initial absorption is expected. The delineation of the soliton regime shows that pulses with $\alpha\tau^2$ reshape into a solitary wave if $\theta_\omega > 1.1\pi$. A dense ensemble of two-level systems with $N = 10^7\lambda^{-3}$ is chosen, so that the differences in group velocities between 2π-pulses of different intensities are maximised and result in appreciable distances between the pulses after the short propagation lengths simulated here. Additionally a dephasing rate of $\omega_0/1000$ is assumed for the absorbing medium and linearly chirped Gaussian pulses of 12 cycles transform-limited duration (FWHM) are employed.

Chirped pulses lose amplitude upon entering the medium, but subsequently they stay stable apart from the decay associated with dephasing and backscattering. Figure 5.3 shows the FROG traces of initial pulses and pulses after propagation through the

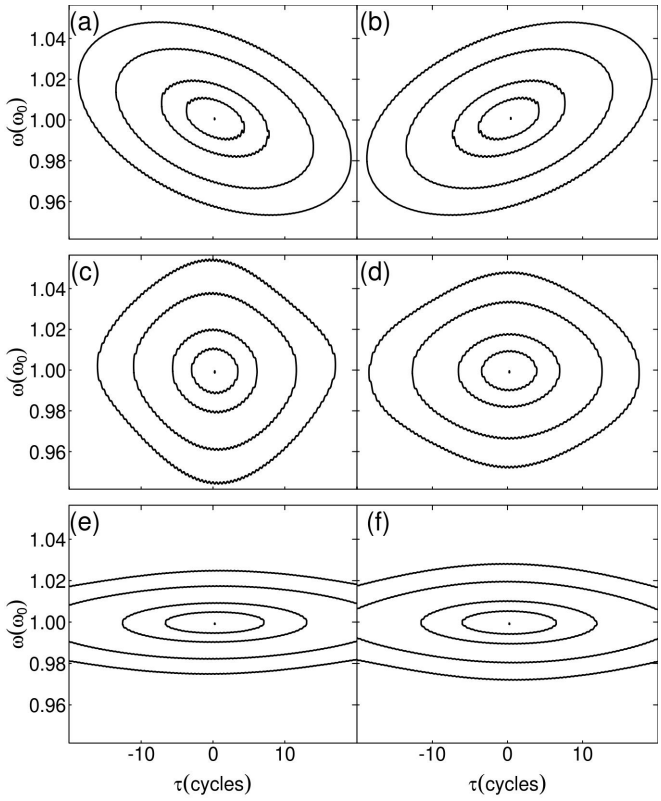


Figure 5.3: FROG traces calculated from equation (A.10) for positive (left) and negative (right) initial chirp of $\alpha\tau^2 = 1$. (a) and (b) show the initial pulses, (c) and (d) the final FROG traces of pulses with initial frequency domain area of 2π and (e) and (f) the final FROG traces of pulses with initial time domain area of 2π.

ensemble of two-level systems, thereby illustrating the changes in the pulses during propagation. From the symmetry of the final FROG traces with regards to the delay τ it can be seen that the chirp disappears in propagation for both, initially negatively or positively chirped, pulses. If the amplitude of the initial pulse corresponds to a frequency domain area $\theta_\omega = 2\pi$ [see Figures 5.3(c) and (d)] the pulses become significantly narrower in time-domain, while they narrow only slightly in frequency-domain due to the initial absorption. If, however, the amplitude of the initial pulse is smaller [see Fig. 5.3(e) and (f)], so that it corresponds to a time domain area of 2π the pulses broaden temporally and narrow significantly in frequency-domain. Note that the final pulses generated by negatively or positively chirped pulses are not necessarily equal. Figures 5.3(c) and (d) reveal a slight difference. Such a difference is possible because the dynamics of a two-level system excited by a positively chirped pulse is different from the dynamics of a two-level system excited by a negatively chirped pulse although the final inversion

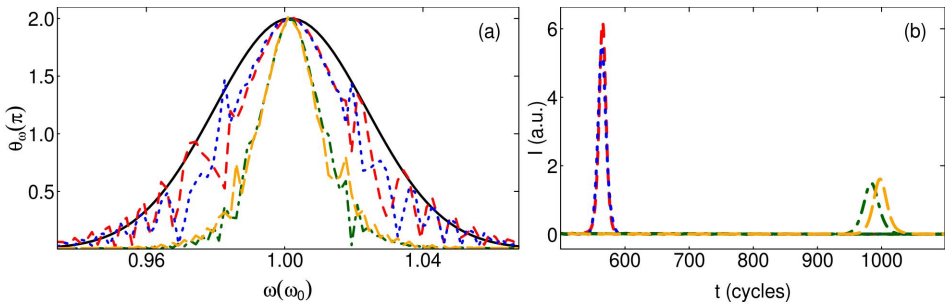


Figure 5.4: (a) Spectra of initial pulse with $\theta_\omega = 2\pi$, $\alpha\tau^2 = 1$ and $\tau_0 = 12$ cycles (solid black line), compared to spectra of final pulses after propagation for $\theta_\omega = 2\pi$ and $\alpha\tau^2 = 1$ (short-dashed red line) or $\alpha\tau^2 = -1$ (dotted blue line); and for $\theta_t = 2\pi$ and $\alpha\tau^2 = 1$ (dash-dotted dark green line) or $\alpha\tau^2 = -1$ (long-dashed orange line). (b) Envelopes after propagation for the final pulses.

reached in a single two-level system is independent of the direction of the chirp.

The difference between the bandwidth of initial and final pulses becomes clearer by looking at the pulse spectra shown in Fig. 5.4(a). Indeed, the narrowing of the pulses in frequency domain that the FROG traces already suggested is clearly visible in the spectra. It can also be seen that the pulses have reshaped from a Gaussian shape to the secant hyperbolic shape typical of a soliton. Furthermore, all final pulses have the same amplitude at the resonance frequency, a fact that confirms the usefulness of the frequency domain formulation of the area theorem to determine the pulse character. The origin of the oscillations at the flanks of the spectrum is the radiation that has been shed by the pulses during the reshaping process into a soliton.

Figure 5.4(b) shows the temporal pulse envelopes after propagation for the different cases depicted in Fig. 5.4(a). Comparing the pulses with the same chirp and different amplitude, we see that the solitary waves created from the less intense initial pulses experience a longer delay, are less intense, and wider in the temporal domain, just as expected from SIT theory. A comparison between negatively and positively chirped pulses reveals that the negatively chirped pulses have a slightly longer delay. Nevertheless, the pulse with time domain area 2π and negative chirp is slightly more intense than its positively chirped counterpart. Considering that the dynamics of a two-level system under excitation from a negatively chirped pulse differs from its dynamics when excited by a positively chirped pulse, this small and unexpected difference may occur due to a slower reshaping and stimulated emission process for positively chirped pulses.

5.4 Resonant propagation of strongly chirped pulses

This section investigates the dynamical transition from CPT to SIT while using the same medium parameters as in the previous section. Three different pulses are studied as example cases. Compared to the previous section, the transform-limited pulse lengths of the pulses are kept at 12 cycles FWHM, but a greater chirp is applied, so that the pulses are well inside the regime of robust CPT. Pulse A has a chirp of $\alpha\tau^2 = 5$, corresponding to the single atom response of Fig. 5.1(c) and a frequency domain pulse area $\theta_\omega = 3\pi$. Pulse B is characterised by $\alpha\tau^2 = 5$ and $\theta_\omega = 4\pi$, and pulse C by $\alpha\tau^2 = 10$ and $\theta_\omega = 3\pi$.

Figure 5.5 presents the spatio-temporal dynamics of the inversion of the dense ensemble of two-level systems excited by the three pulses A, B and C. For all three cases a transition from CPT to transparency is evident, as a stationary inversion is only present at the entrance of the pulse into the medium. Pulse A evolves into two solitary waves that each achieve a complete rotation of the Bloch vector, i.e. they are 2π-pulses. At a later point in time (outside the range of the graphs shown), yet another weak pulse develops from the inverted two-level systems and eventually gets absorbed again due to the dephasing in the medium. By this mechanism some of the population inversion achieved at the entrance into the medium is stripped away. Pulse B with an increased pulse area of 4π initially excites population across a larger region at entrance into the medium, but later on another spawned solitary wave distributes this inversion deeper into the absorbing medium. Also, two fast pulses are created instead of one. When the chirp instead of the area is increased (pulse C) the region of CPT achieved after the pulses have passed does not increase significantly. Again fast solitary waves, slow solitary waves, and radiation carry away most of the energy of the exciting pulses.

Studying the electric field spectra at different spatial points along the absorbing medium can give an indication of the dynamical reshaping that acts on the pulses to transform them into solitary waves. Figure 5.6 compares, for pulse A, the input spectrum with spectra taken at $z = 4\lambda$ and $z = 8\lambda$ inside the absorbing medium. For $z = 4\lambda$ and for $z = 8\lambda$ most of the spectral amplitude has decreased, a consequence of absorption. At $z = 4\lambda$ absorption has burned a spectral hole into the pulse amplitude close to the resonance frequency. The peak exactly at resonance originates from the late, slow

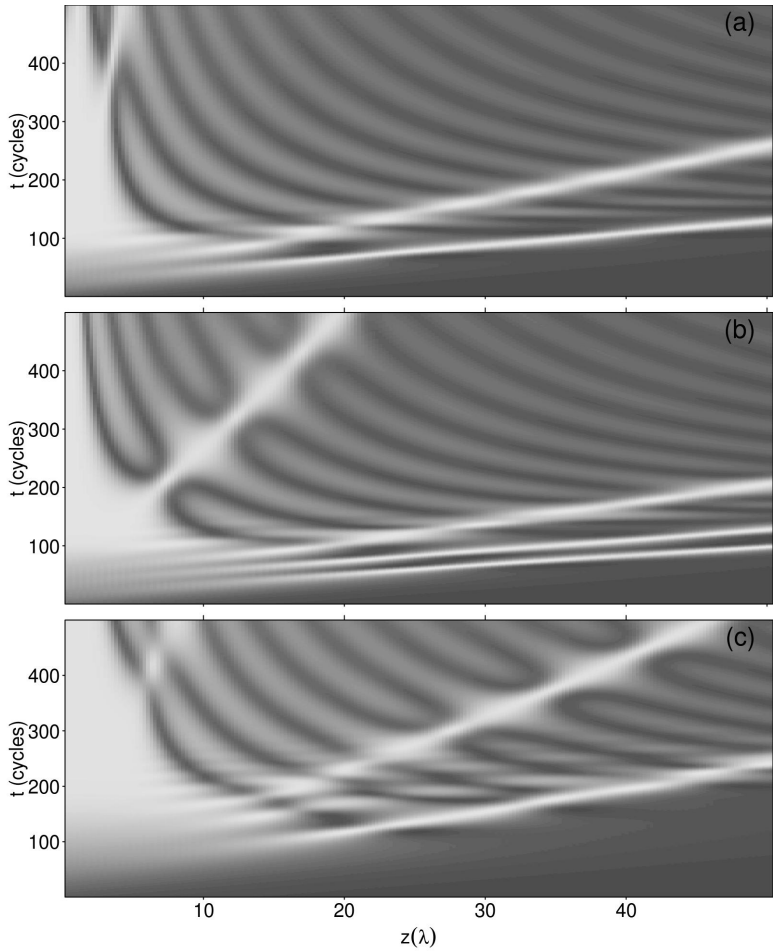


Figure 5.5: Linear grey-scale plot of the Inversion W against time and propagation distance for initial pulses with $\theta_\omega = 3\pi$ and $\alpha\tau^2 = 5$ (a), $\theta_\omega = 4\pi$ and $\alpha\tau^2 = 5$ (b) and $\theta_\omega = 3\pi$ and $\alpha\tau^2 = 10$ (c). Figure reproduced from [56].

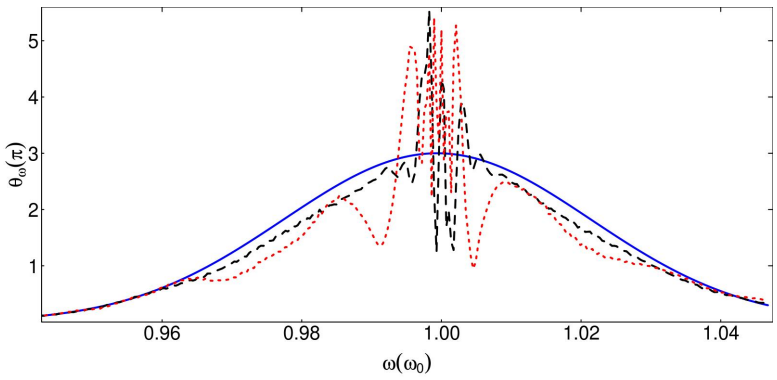


Figure 5.6: Initial pulse spectrum (solid blue line) compared to pulse spectra taken at $z = 4\lambda$ (dashed black line) and $z = 8\lambda$ (dotted red line) for pulse A [Fig. 5.5(a)].

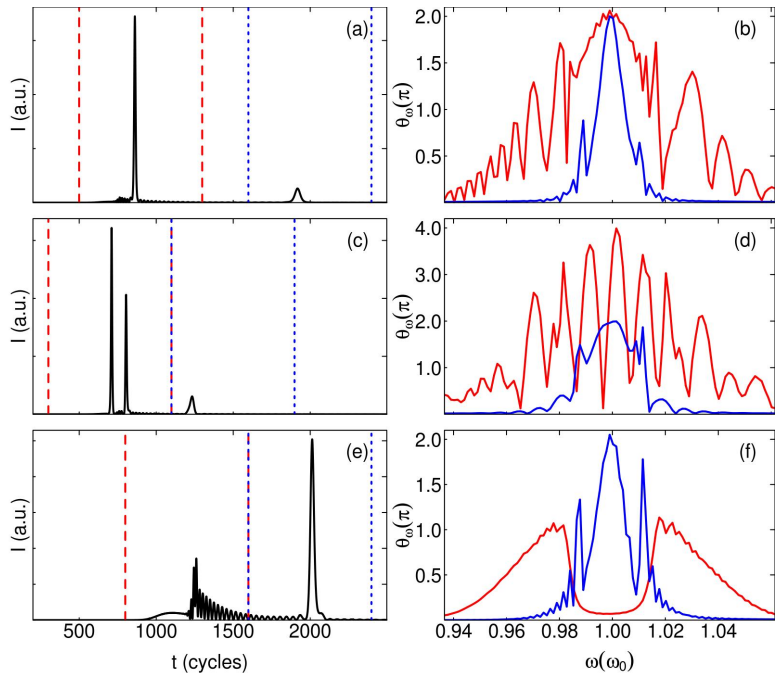


Figure 5.7: Pulse envelopes and spectra for pulses that propagated 200λ through the absorber. Initial pulse area and dimensionless chirp are: (a) and (b) $\theta_\omega = 3\pi$ and $\alpha\tau^2 = 5$, (c) and (d) $\theta_\omega = 4\pi$ and $\alpha\tau^2 = 5$, (e) and (f) $\theta_\omega = 3\pi$ and $\alpha\tau^2 = 10$. The spectra on the left are taken in the time windows indicated by the dashed red line on the right for the solid red line and by the dotted blue line for the solid blue line. The intensity scales are not uniform across the graphs.

solitary wave that is also seen in the top left corner of Fig. 5.5(a). At $z = 8\lambda$ the frequencies close to resonance are already partially restored at the expense of frequencies further away from resonance, a sign of the reshaping into a solitary wave that is spectrally narrower than the initial pulse. In fact, at $z = 8\lambda$ CPT is not observed any more in the inversion of the medium, as the exciting pulse has already split into soliton and radiation parts. The radiation shed by the pulse is responsible for the strong oscillations in the spectrum. A narrow soliton peak on top of the broader soliton peak of the fast 2π-pulse is the consequence of a second, slower solitary wave. These results show that the formation of 2π-pulses out of strongly chirped pulses involves a complex interplay between absorption, dispersion, and nonlinear processes. This interplay dynamically alters the frequency content of the pulse over very short length scales.

Looking at longer propagation distances, Fig. 5.7 shows pulse envelopes and spectra at the exit of the medium, i.e. at a distance where the reshaping of the pulses has already been achieved. Because of the long propagation distance, the slow solitary waves have

now accumulated a considerable delay and can be clearly separated. The spectra are therefore taken in two time windows, the first of which contains the fast propagating radiation part and intense solitary waves, whereas the second window contains only the slow propagating solitary wave. These results illustrate some of the fundamental aspects of SIT and clearly show the solitary wave character of the propagation. For pulse A [Fig. 5.7(a) and (b)] two solitary waves arrive, one of which is fast, intense, very short, and has a broad spectrum with oscillations caused by radiation. In contrast, the slower pulse is less intense, longer in duration, and with a narrower spectrum. The spectral amplitude at the resonance frequency of both pulses corresponds to $\theta_\omega = 2\pi$. Increasing the initial amplitude to $\theta_\omega = 4\pi$ (pulse B) leads to the creation of an additional pulse (as already observed in the inversion map [Fig. 5.5]) that also propagates very fast, so that the first two pulses cannot be separated in the spectrum [see Fig. 5.7(c) and (d)]). Because of their close proximity the pulses interact via the absorbing medium and are not independent solitary waves. In the spectrum, the interaction between the pulses manifests itself as oscillations in the amplitude reaching up to 4π. Exactly at resonance the spectral value only reaches 2π, again illustrating that these two pulses cannot be seen as independent solitons, since the spectrum of two independent solitons should have a value of 4π at resonance. The slowly propagating pulse constitutes another, well separated 2π-pulse.

The last row of Fig. 5.7 shows pulse C with an even higher initial chirp of $\alpha\tau^2 = 10$. Here, only one soliton is created out of the initial pulse of area $\theta_\omega = 3\pi$. Although the initial electric field could be confused with a solitary wave in time domain, the spectra clearly show that only the second part is a 2π-pulse with a 2π amplitude at the central frequency. The first strong electric field pulse registered in time domain is completely off-resonant, containing merely radiation. Figure 5.7, especially panels (e) and (f), reveal the importance of measuring the pulse spectra in order to determine the nature of a pulse propagating through resonant absorbers. The spectral amplitude at resonance gives a simple criterion for the experimental distinction between a 2π-pulse and an off-resonant 0π-pulse. The measured temporal pulse shape without phase information is not sufficient to distinguish between off-resonant 0π-pulses and resonant 2π-pulses.

Polarisation gate FROG traces of pulses A-C after propagation have been taken in the time windows shown on the right of Fig. 5.7 and are depicted in Fig. 5.8. The fast pulses

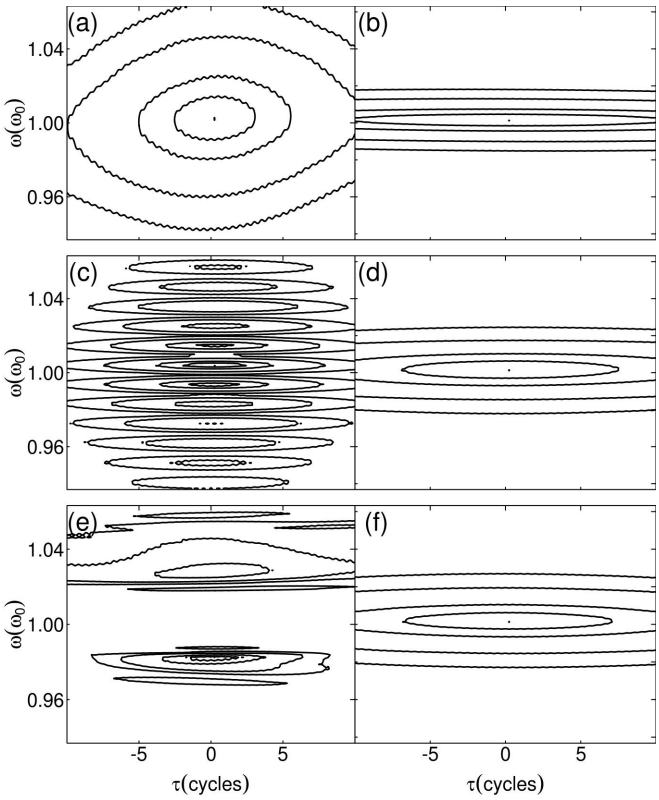


Figure 5.8: (a), (b) Polarisation gate FROG traces corresponding to Fig. 5.7(b); (c), (d) corresponding to Fig. 5.7(d); and (e), (f) corresponding to Fig. 5.7(f). The FROG traces on the left [(a),(c) and (e)] are taken for the earlier time windows and the traces on the right [(b),(d) and (f)] are taken for the later time windows, as marked by dashed (dotted) lines in Fig. 5.7.

are presented on the right, the slow, delayed solitary waves on the left. For both, fast and slow, pulses the chirp has clearly disappeared as the FROG traces are symmetric with regards to $\tau = 0$. However, for the fast pulses corresponding to Figs. 5.7(d) and (f) the complicated spectral structure is reproduced in their FROG traces. The FROG traces on the right, in contrast, largely correspond to simple, sech-shaped, transform-limited pulses with different bandwidths; i.e. they are FROG traces of the fundamental 2π-pulses of SIT theory. Hence, the FROG traces illustrate most clearly the transformation of strongly chirped pulses after propagation through a resonant absorber.

5.5 Conclusions

This Chapter, studying the interaction of chirped pulses with a dense ensemble of two-level systems, revealed the existence of a dynamic transition from complete population transfer to self-induced transparency. At entrance into the medium chirped pulses excite the absorber, while, during propagation, absorption and pulse reshaping combine to produce unchirped pulses that propagate without further absorption. For strongly chirped pulses some of the achieved inversion at entrance is re-emitted into further solitary waves. Hence, the efficiency of adiabatic rapid passage is limited in dense ensembles of two-level systems. Increases in pulse intensity, beyond the intensity needed to fulfil the adiabaticity condition at entrance into the medium, do not translate into more inversion in the medium.

The study of chirped pulses also allowed for the comparison of frequency- and time-domain pulse area theorems in their capability to assess pulse propagation properties. It was found that both area theorems are unable to predict the number of created solitary waves, the frequency domain area is, however, more useful in determining the self-induced transparency character of the pulses [102]. Since it is given by the spectral amplitude alone without requiring any phase information it is more easy to determine. Using FROG traces, thus mixing time-domain and frequency-domain information, gives a very intuitive illustration of the pulse properties.

Chirped pulse propagation through absorbers also showed that the dispersive properties of the absorbers tend to create unchirped pulses, i.e. they compensate for accumulated dispersion. It is thus to be expected that pulses propagating in dispersive

waveguides may stay transform-limited if sufficiently dense absorbers are present in the waveguide. Additionally, it is clear that 2π-pulses that become chirped while propagating through a waveguide will initially experience absorption when encountering an absorbing medium. The next Chapter investigates the conditions on an absorbing waveguide for it to allow for solitary propagation of self-induced transparency pulses.

Chapter 6

Self-induced transparency in nanophotonic waveguides

In the previous chapters we have discussed SIT in a one-dimensional approximation, assuming plane-waves in free-space. We have seen that plane-wave SIT allows for strong interactions between counterpropagating pulses leading even to the birth of additional solitary waves depending on group velocity and relative polarisation of the initial pulses. Further, a dynamic transition between complete population transfer via adiabatic rapid passage and self-induced transparency has been uncovered during which a chirped pulse is split into soliton and radiation parts. Now the main topic of this thesis is addressed, namely to find conditions that allow for a confinement of SIT solitons to a mode area in the range of or smaller than its wavelength using nanophotonic waveguides.

One important prerequisite for the existence of SIT solitons in waveguides is the possibility to define an effectively one-dimensional representation of the multi-dimensional waveguide geometry. In Section 6.1 general conditions on nonlinearity and waveguide geometry are identified that allow the reduction of a nonlinear waveguide to an equivalent one-dimensional system. For fixed-order nonlinearities light propagation in all single-mode waveguides can be reduced to one-dimensional propagation equations, whereas saturable nonlinearities allow for the definition of approximate efficient parameters of a one-dimensional propagation equation. In the presence of the coherent and resonant Maxwell-Bloch equations, however, it is found that a reduction of the waveguide to an effectively one-dimensional system is only possible if the Rabi frequency follows a Heav-

iside step function in the directions transverse to the propagation direction. Section 6.2 examines the propagation of light pulses through nanoscopic gap waveguides filled with resonant absorbers by numerically integrating the two-dimensional Maxwell-Bloch equations. These waveguides fulfil the conditions for effective one-dimensionality to a good approximation. Solitary wave propagation is found if the ratio between absorber density and pulse intensity is high enough to allow for a cancellation of the intrinsic waveguide dispersion. Under these conditions, other classical signatures of SIT, such as negligible absorption, a strong group delay, and pulse breakup of 4π-pulses into two 2π-pulses, are also encountered. Further, Section 6.3 investigates the interaction properties of counterpropagating simultons, again encountering parameter dependent soliton birth. Such light-light interactions could thus, in principle, be employed in compact geometries to enable optical computation. Finally, a scheme for an optical memory, devised for plane-wave SIT [42, 43], is validated in the gap waveguide geometry (see Sec. 6.4), possibly allowing for an extremely compact optical memory. The findings of this chapter are summarised in Section 6.5.

6.1 One-dimensional equations and nonlinear propagation

It is well known that a nonlinear waveguide with a Kerr nonlinearity can be effectively described as a one-dimensional system if it is single-mode and if the frequency content of the pulse is narrow [55, 109]. The question we aim to answer in this section is if the same is true in the presence of arbitrary nonlinearities. The important property for instantaneous nonlinearities is the nonlinear phase shift, which is not determined by the conventional effective area of the waveguide for an arbitrary order of nonlinearity. An average phase shift can, however, still be calculated for each nonlinear order independently. When nonlinearities of different orders are present in a pulse and the strength of each of them is known, a one-dimensional equation can be defined. One such case is the cubic-quintic Ginzburg-Landau equation where the fifth-order nonlinearity enables a simultaneous stabilisation of pulses and background states in non-conservative systems [110].

One-dimensionality is not retained, however, if the susceptibility cannot be expressed as a finite sum of polynomials of the light intensity. In the following, several such cases

are discussed and it is determined whether approximate one-dimensional expressions can be found for arbitrary waveguide geometries.

6.1.1 Saturable nonlinearities

An example of a mixed order nonlinearity is the saturable nonlinearity, since this nonlinearity consists, in general, of contributions from an infinite number of orders. Hence, the relation between nonlinear phase shift and intensity can not be expressed in a simple analytical form any more. For the saturable nonlinearity described by [111, 112]

$$\epsilon_{NL} = \alpha \frac{I}{1 + \kappa I}\,, \tag{6.1}$$

with coefficients α and κ defined, for example, over the radius r_0 of a fibre with Gaussian mode profile (for both, magnetic and electric fields), the nonlinear phase shift can be calculated as

$$\phi_{nl} = \frac{2\pi L}{\lambda} \frac{\int_0^{r_0} n_2 I^2(r)/[1 + \kappa I(r)]\mathrm{d}r}{\int_0^{\infty} I(r)\mathrm{d}r}\,. \tag{6.2}$$

This equation can not be simplified for an arbitrary field profile. Therefore, one-dimensional propagation equations for the description of waveguides with saturable nonlinearities are necessarily approximations. Fig. 6.1(a) shows the different polarisation distributions for a (hypothetical) single-mode fibre with a Gaussian mode profile and the saturable nonlinearity of equation (6.1). An intense pulse propagating through this fibre will experience the polarisation profile corresponding to $\kappa\, I \approx 0$ at the leading and trailing edge but a substantially different profile corresponding, e.g., to $\kappa\, I = 10$, at its maximum.

If a one-dimensional approximation to the propagation equations in the nonlinear waveguide is nonetheless desirable, an effective saturation coefficient κ_{eff} may be defined that describes approximately the nonlinear phase shift for the saturable nonlinearity. This is achieved by replacing equation (6.1) with

$$\epsilon_{NL} = \alpha \frac{I(x)}{1 + \kappa_{\mathrm{eff}} I(x = 0)}\,. \tag{6.3}$$

For a given maximum intensity $I_{\max} = I(x = 0)$, material saturation coefficient κ, and

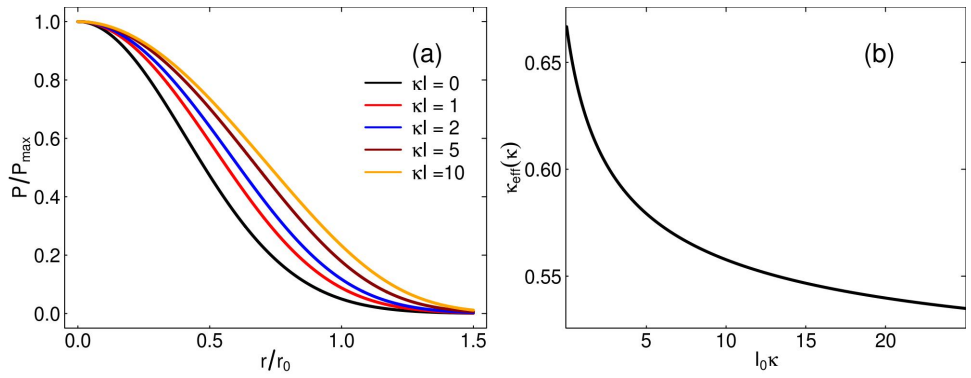


Figure 6.1: (a) Radial dependence of the polarisation P normalized to its maximum value $P_{\max}$ for values of $\kappa\, I$ from 0 to 10 induced by the saturable nonlinearity of equation (6.1). A single-mode fibre with a Gaussian mode profile $[E(r,\phi) = E_0 \exp(r^2/r_0^2)]$ is assumed. (b) Effective saturation coefficient κ_{eff} in dependence of the electric field intensity for a single-mode fibre with Gaussian mode profile.

an electric field profile $\xi(\mathbf{r})$ the effective saturation coefficient κ_{eff} is then calculated as

$$\kappa_{\text{eff}} = \frac{1}{I_{max}} \left(\frac{\int I(\mathbf{r})^2 \mathrm{d}\mathbf{r}}{\int I(\mathbf{r}^2)/[1+\kappa I(\mathbf{r})]\mathrm{d}\mathbf{r}} - 1 \right) \tag{6.4}$$

The result of equation (6.4) for a single-mode fibre with Gaussian mode profile is presented in Fig. 6.1(b). It can be seen that the effective saturation coefficient is smaller than the pure saturation coefficient and it varies by from $\kappa_{\text{eff}} \approx 0.82$ to $\kappa_{\text{eff}} \approx 0.74$ between $I_0 = 0$ and $I_0 = 20$.

As the nonlinear phase shift calculated in Fig. 6.2 shows for the example of a single-mode fibre with Gaussian mode profile, an approximation with κ_{eff} can work reasonably well over a large intensity range. Indeed, when saturation intensities are calculated from experimental data, there are many sources of uncertainties on the exact value of the saturation intensity and the errors stemming from the fundamental issue discussed above are often insignificant.

6.1.2 Saturable absorbers

Saturable absorbers are important components of passive mode-locking schemes to generate short pulses. They can help create and stabilize short pulses in a laser cavity [37], such as for example a vertical external cavity surface-emitting laser (VECSEL) [113], because the edges of the pulses experience more absorption than the more intense

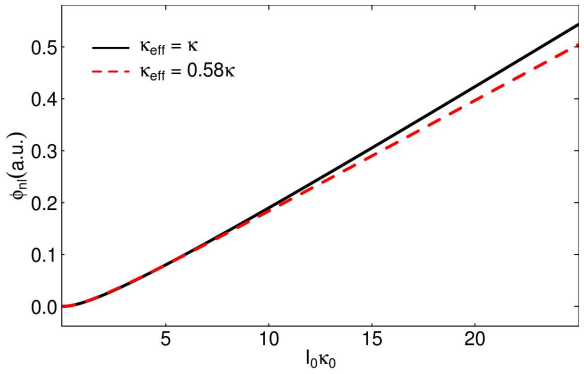


Figure 6.2: Dependence of the nonlinear phase shift on the electric field intensity for a saturable nonlinearity with $\kappa_{\text{eff}} = \kappa$ (solid green line) and an effective saturable nonlinearity $\kappa_{\text{eff}} = 0.58\kappa_0$ (dashed red line).

central parts. In the limit of pulses that are long compared to the dephasing times of the absorber, absorption can be described by simple rate equations where the medium polarisation has been eliminated. Then the absorption α depends on the intensity of the exciting light pulse via the simple relation [114]

$$\alpha(t) = (1 - \triangle\alpha) + \frac{\triangle\alpha}{1 + I(t)/I_{\text{sat}}}\,, \tag{6.5}$$

reminiscent of a saturable nonlinearity. Here $\triangle\alpha$ denotes the modulation depth. In fact, the only difference between this equation and equation (6.1) is that it describes changes in the imaginary part of the refractive index instead of the real part. If the response of the saturable absorbers is local (diffusion is negligible) the analysis of the previous subsection can be applied here as well.

The overall absorption coefficient in a waveguide filled with non-diffusive saturable absorbers is calculated as

$$\alpha = (1 - \triangle\alpha) + \frac{\int \frac{\triangle\alpha I(\mathbf{r})}{1+I(\mathbf{r})/I_{\text{sat}}^{\text{mat}}}\mathrm{d}\mathbf{r}}{\int I(\mathbf{r})\mathrm{d}\mathbf{r}}\,. \tag{6.6}$$

Comparing this to the simple mode-averaged formula with an effective saturation intensity a relation between the intrinsic saturation intensity of the absorber $I_{\text{sat}}^{\text{mat}}$ and the effective saturation intensity of the combined system of material and geometry $I_{\text{sat}}^{\text{eff}}$ can

be derived

$$\frac{I_{\mathrm{sat}}^{\mathrm{eff}}}{I_{\mathrm{sat}}^{\mathrm{mat}}} = I_{\max}\left(\frac{\int \xi^2(\mathbf{r})\mathrm{d}\mathbf{r}}{\int \frac{\xi^2(\mathbf{r})}{1+I_{\max}\xi^2(\mathbf{r})}\mathrm{d}\mathbf{r}}\right)^{-1} . \tag{6.7}$$

Here $\xi(\mathbf{r})$ is the mode profile of the waveguide. Again, note that the experimental errors on the saturation intensity are usually large enough to overshadow the issues stemming from the afore-mentioned analysis. Hence, the approximation of the saturable nonlinearity by an effective one-dimensional model is appropriate. An example of the experimental determination of saturation intensities can be found in [114].

6.1.3 Coherent absorbers

The interaction between a light pulse and a coherent two-level absorber is described by the Bloch equations (3.7). These equations are formulated under the assumption of vanishing relaxation rates in the absorber and are therefore valid if the electromagnetic pulse is much shorter than these relaxation times; the opposite to the saturable absorption limit in the previous subsection. As a consequence the Bloch vector of the two-level system always stays on the surface of the Bloch sphere ($|\rho_{12}|^2 + W^2 = 1$). The state of the two-level system can thus be expressed by the two angles ψ and ϕ of the Bloch vector alone

$$\rho_{12} = \sin(\psi)[\cos(\phi) + i\sin(\phi)] \qquad W = \cos(\psi)\,. \tag{6.8}$$

For a pulse $E^+(x,y;k,\omega) = \sum_\zeta A_\zeta(k,\omega)E_\zeta(x,y,\omega)$ propagating in a waveguide with modes ζ, mode profiles $E_\zeta(x,y,\omega)$ and propagation constants $\beta_\zeta(\omega)$ one can write [27]

$$(\beta_\zeta^2(\omega) - k^2)A_\zeta(k,\omega) = -\frac{\omega\beta_\zeta(\omega)}{2N}\iint_{-\infty}^{\infty} P(x',y',k,\omega)E_\zeta(x',y',\omega)\theta_{\mathrm{active}}dx'dy'\,, \tag{6.9}$$

with θ_{active} the Heaviside step function which is 1 only at positions where an absorber is present and 0 everywhere else. Under the assumption of a slowly varying envelope and by neglecting group velocity dispersion and mode profile dispersion this equation can be further simplified to

$$(\partial_z + \frac{1}{V_g}\partial_t)\varepsilon(z,t) = \frac{i\omega_\zeta}{4N}e^{-i(\beta_\zeta z - \omega_\zeta t)}\iint_{-\infty}^{\infty} P(z,t,x',y')E_\zeta(x',y',\omega)\theta_{\mathrm{active}}dx'dy'\,. \tag{6.10}$$

Now, using equation (6.8) one can replace $P(z,t,x',y')$ with $2\mu N\sin[\psi(z,t,x',y')]$ [26]

and since $\sin(\psi)$ is linear in the electric field we can finally write

$$(\partial_z + \frac{1}{V_\zeta}\partial_t)\varepsilon(z,t) = \frac{i\omega_\zeta \mu}{2} e^{-i(\beta_\zeta z - \omega_\zeta t)} \cdot \iint_{-\infty}^{\infty} \sin[\psi_1(z,t) E_\zeta(x',y',\omega) + a] E_\zeta(x',y',\omega)\theta_{\text{active}} dx' dy' \,, \quad (6.11)$$

where a denotes an initial angle of the Bloch vector ψ common to all absorbers. From equation 6.11 we can see that a linearisation of this equation in the transverse directions is impossible unless the active system is only defined at points of constant field profile so that

$$E_\zeta(x',y',\omega)\theta_{\text{active}} = \text{const}\,, \quad (6.12)$$

since a nonlinearity of infinite order, i.e. a sine-function, is present. If the argument of the sine-function explicitly depends on the transverse coordinates no approximation can be found that is valid for all times and electric field values. A setup that fulfils (6.12) can be achieved either with a very thin gain layer or a waveguide geometry that allows for an approximately constant mode profile. Whenever these conditions are not fulfilled the full multi-dimensional problem has to be solved; one-dimensional equations will give inaccurate or wrong results. Yet, since work by Guzman *et al.* in 1990 [115], where a linearisation and mode-averaging of the polarisation has been performed, many articles have been published that seem to rely on this erroneous procedure [28, 31, 116–119].

To further clarify the problem let us investigate in detail the pulse propagation through a two-dimensional waveguide with resonant absorbers that does not fulfil condition (6.12) [50]. We consider a slab of width $w = 400\,\text{nm}$ and refractive index $n_r = 3.48$ that is doped across its whole width with an absorber of dipole strength $\mu = 1.602 \cdot 10^{-29}\,\text{Cm}$ (resonant at $\lambda = 1550\,\text{nm}$) and surrounded by an air cladding. Because the propagation is calculated in a two-dimensional setup using the FDTD method, waveguide dispersion is inherently included up to arbitrary order, and both absorber and field profiles are resolved in lateral direction. Each pulse is injected with the lateral profile of the fundamental mode at the centre frequency $\nu = 193.4\,\text{THz}$ and with the temporal profile of a 2π-pulse at the centre of the waveguide. For a static lateral profile, the local area of the pulse at a location (x, z) depends on the time-integral of the electric

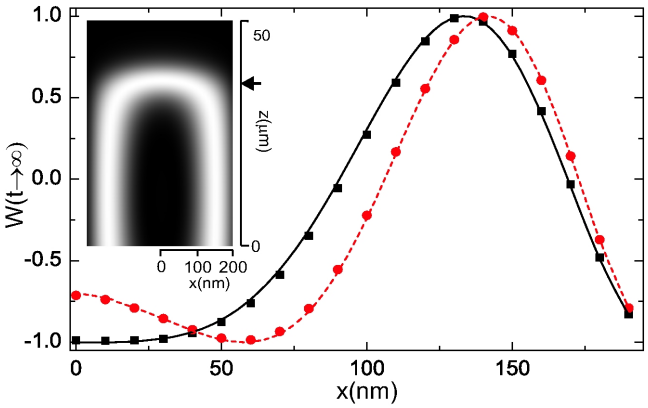


Figure 6.3: Lateral final inversion profile after pulse with $A(x = 0, z = 0) = 2\pi$ has passed; $w = 400\,\mathrm{nm}$, $n_r = 3.48$. Absorber densities are $n = 10^{17}\,\mathrm{cm}^{-3}$ (black squares) and $n = 2 \cdot 10^{18}\,\mathrm{cm}^{-3}$ (red circles). Solid black (dotted red) line is calculated from equation (6.14) with $A(x = 0) = 2\pi$ ($A(x = 0) = 2\pi\kappa$ $\kappa = 1.125$). Inset: snapshot of the population inversion $W(x, z)$ for the case of $n = 2 \cdot 10^{18}\,\mathrm{cm}^{-3}$; $W = 1$ (white), $W = -1$ (black). The arrow indicates the position of the pulse. Figure reproduced from [50].

.

field envelope at this point, i.e.

$$A(x, z) = \frac{\mu}{\hbar} \int_{-\infty}^{\infty} \xi(x) E(z, t) \mathrm{d}t \,, \tag{6.13}$$

where $\xi(x)$ is the profile of the fundamental symmetric TE polarised mode.

Neglecting mode profile dispersion, the residual inversion can be calculated analytically from the pulse area as

$$W(x, z, t \to \infty) = -\cos\left[A(x, z)\right] . \tag{6.14}$$

Figure 6.3 shows the z-average of the final inversion $W(x, t \to \infty)$ for a dilute absorber (black) and a dense absorber (red). For the dilute absorber the simple analytical considerations agree well with the numerical experiment (black line and squares respectively), i.e. the final inversion follows equation (6.13) with $A(x = 0) = 2\pi$. However, for the dense absorber (red line and circles) the inversion pattern is shifted due to the influence of the medium polarisation, so that the effective area of the pulse is increased. Equation (6.13) can still provide the correct transverse dependence when a higher area of $2\pi\kappa$ with $\kappa \approx 1.125$ is assumed.

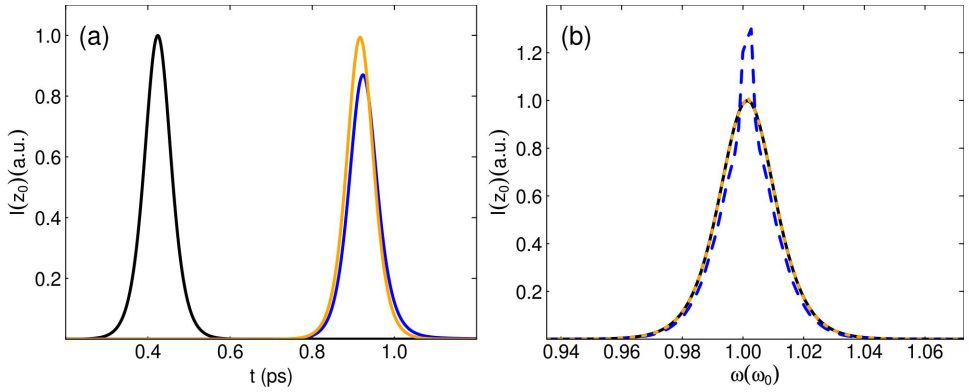


Figure 6.4: (a) Intensity I of the temporal pulse envelopes and (b) pulse spectra taken for the initial pulse (black lines) and at the point z_0 indicated by the arrow in Fig. 6.3 at $x = 0$ for a dense absorber (blue lines) and a dilute absorber (orange lines).

In both cases inversion is left in the absorber after the pulse has passed. This can also be seen from the inset of Fig. 6.3 that shows the inversion pattern in the waveguide while the pulse is still in the system (at the position of the arrow). Indeed, this follows directly from equation (6.13). Residual inversion in the absorber is equivalent to absorption. Hence, the pulse loses energy while propagating, and as a consequence it narrows spectrally and spreads in time according to the area theorem. While the pulse is still fast enough not to be influenced by the dephasing and spatially extended enough not to experience significant backscattering, the main part of the pulse reshapes to keep its area constant at $A(x = 0) = 2\pi$. The trailing electric field shows up in Fig. 6.4(b) as a bump at the resonance frequency in the spectrum of the electric field (blue dashed line). The spectrum is calculated at the longitudinal point indicated by the arrow in the inset of Fig. 6.3 and transversely in the middle of the waveguide ($x = 0$). Hence, we observe again that the spectral intensity at the centre frequency of the pulse is the quantity that correctly defines the action of the electric field on the absorbing medium. It is also much easier to determine than the pulse area defined in the temporal domain, as discussed in the previous chapter.

Comparing the spectra of the initial pulse (black line) and the pulse after propagation through the absorber we see that the pulse has narrowed in frequency space. For the case of a dilute absorber (orange dotted line, corresponding to the black line in Fig. 6.3) no significant pulse reshaping has occurred over the short propagation distance, as can be seen from both pulse spectra and pulse envelopes in Fig. 6.4. The pulse envelopes

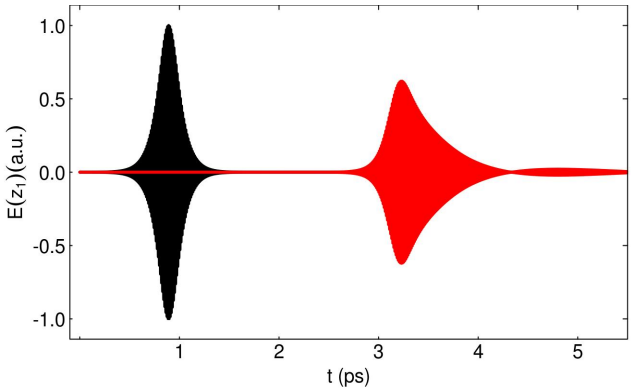


Figure 6.5: Full temporal evolution of the electric field at the injection point (black line) and 80 μm inside the waveguide (red line) for a pulse with area 2π in the middle of the slab waveguide filled with a dense absorber.

[Fig. 6.4(a)] reveal a small pulse delay introduced by the denser absorber due to a reduced group velocity, whereas the trailing electric field is too weak to be visible in this depiction. Also, the increase in pulse duration is much clearer from the narrowing in the spectrum. Thus, by comparing the spectra we see that the 2π-pulse loses energy while propagating through the waveguide filled with the denser absorber, but it essentially remains a 2π-pulse in the middle of the waveguide.

Fig. 6.5 shows the pulse in the dense absorber at a point further along the waveguide. It clearly has become deformed and has lost much of its amplitude. The trailing edge is prolonged significantly and an echo has built up.

Note that we assumed that no broadening is present in the resonant absorber; if there is strong inhomogeneous broadening (broader than the pulse width) the trailing electric field seen in the spectrum would be weaker because the individual polarisations would very soon be out of phase so that no net polarisation would be left. In this sense, the trailing electric field and the shift of the pulse area are a consequence of excluding inhomogeneous broadening, however, the validity of equation (6.13) is not affected by this assumption.

We have therefore established with analytic considerations and numerical tests that the condition for absorption-less 2π-pulse propagation (self-induced transparency) in a resonantly absorbing waveguide is a pulse area that is constant in the transverse direction. Further, it is clear that such a constant pulse area in a waveguide is only possible if the Rabi-frequency itself is constant over the transverse direction. In the

following section a system is introduced where these conditions are approximated and the question that remains to be addressed is if also the dispersion can be overcome to enable solitary wave propagation. We have learned in the previous chapter that chirped pulses always experience initial absorption, meaning that chirp must not accumulate if transparency is to be achieved.

6.2 SIT of resonantly absorbing nano-structured waveguides

In conventional high-dielectric core/low-dielectric cladding waveguides the electric field profile varies over the whole width of the waveguide and an approximately constant Rabi-frequency can only be achieved if the active medium is placed in a very thin strip, like, for example, in a semiconductor quantum well. For such a case an analysis of SIT in waveguides has been performed by Langbein and Lederer [27], where they disregarded the effect of group velocity dispersion and employed the SVEA. In this approximation the 2π-pulse is a solitary wave with a group index of

$$n_g = n_g^{\mathrm{WG}} + \frac{2n\hbar\omega\Gamma}{\epsilon_0 E_{\max}^2} = n_g^{\mathrm{WG}} + n_g^{\mathrm{SIT}}\,. \tag{6.15}$$

Here, n_g^{WG} stands for the group index of the passive waveguide, $E_{\max}$ is the electric field maximum, n is the density of the absorber, ω is the central frequency of pulse and absorption resonance and $\Gamma = w/(\int \xi(\mathbf{r})\xi^*(\mathbf{r})d\mathbf{r})$ denotes the confinement factor of the mode profile $\xi(\mathbf{r})$ over the absorbing region of width w.

Since group velocity dispersion has been ignored in [27], it is unclear whether the scheme conceived would allow for solitary waves. Several studies since have examined the impact of SIT on group velocity dispersion, but, in order to derive analytical results, approximations were made and depending on the specific approximation differing results were obtained [28, 30]. Considering that the nonlinearity in coherent absorption consists of a sine-function, it is not surprising that results depend on the order of nonlinearity where the truncation is performed. Clearly, such truncations must necessarily be invalid as a sine-function of arbitray argument is not well approximated by a Taylor series of finite order. Using the technique of the inverse scattering transform, Lax pairs (see Section 2.3) have been found corresponding to the nonlinear Schrödinger equation combined with the Maxwell-Bloch equation [31, 120, 121]. Soliton solutions to these en-

velope equations are thus obtained and it becomes evident that resonant nonlinearities can also contribute to the nonlinear phase modulation necessary for dispersion compensation [121]. One possibility that has been explicitly excluded from these studies is pulse propagation in resonant waveguides with vanishing Kerr coefficient. In the study presented here the focus is exactly on this case of a purely resonant nonlinearity. Furthermore, the analytical works on solitons of the nonlinear Schrödinger equation combined with the Maxwell-Bloch equations completely ignore the issues raised by non-constant Rabi frequencies in usual single-mode waveguides and simply assume an effective one-dimensionality. Finally, it is desirable to describe the waveguide dispersion originating from its geometry by representing the full geometry instead of using a Taylor expansion scheme.

The goal of this study is a confined solitary wave based on the SIT effect under the assumption that the off-resonant Kerr effect is negligible. To this end, it is necessary to compensate for waveguide dispersion by the absorption nonlinearity alone and hence a large confinement factor of the electric field mode profile has to be achieved to maximise the impact of the nonlinearity on pulse propagation. In maximising the confinement factor we are constrained by the restriction to a constant Rabi-frequency, established as a prerequisite for transparency in the previous section. In a seminal work, Almeida *et al.* proposed a waveguide with a nanoscopic low-index gap in the middle of the high-index core of a conventional dielectric waveguide [46]. They showed that the boundary conditions thus imposed on the electric field allow for a mode whose electric field is highly enhanced and confined inside the small gap area. Furthermore, as long as the gap width is much smaller than the wavelength, the electric field component orthogonal to the surfaces is almost constant inside the gap. Building on the same principle, a fibre with rotational symmetry has been proposed and fabricated that exhibits high field confinement and almost constant field profiles in the gap area [48]. In Fig. 6.6(b) schematics of such waveguides are depicted.

In the following, numerical injections of sech-shaped pulses into the fundamental E_x-polarised mode of a $2D$ slot waveguide with gap width 100 nm are performed which use the total field/scattered field method described in Sec. A.4. The pulse area was chosen to be 2π (later 4π) at the centre of the resonantly absorbing slot waveguide [a $2D$ representation of the geometries shown in Fig. 6.6(b)]. The outcome of the propa-

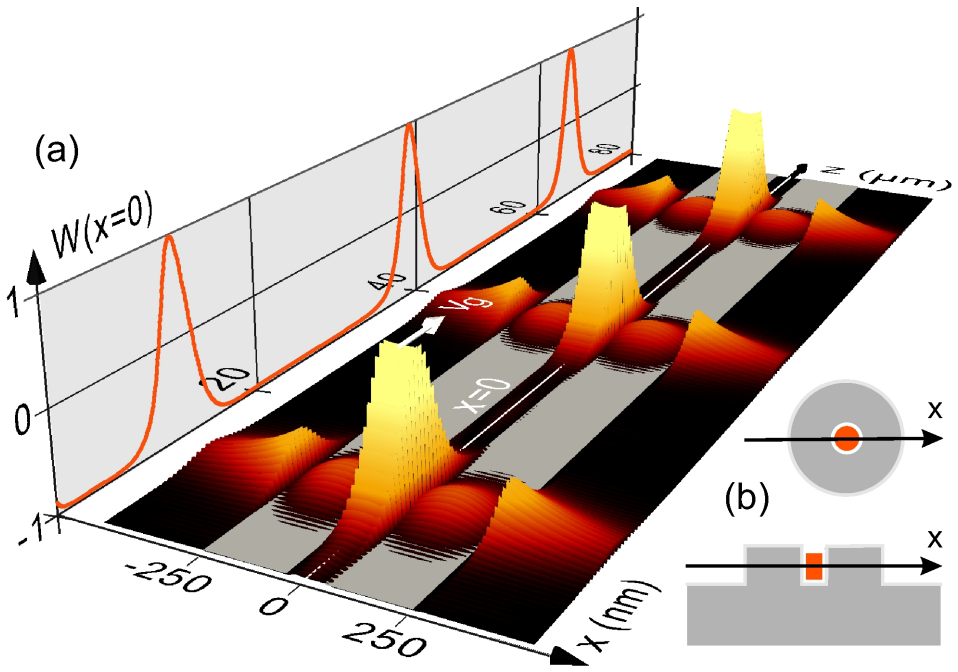


Figure 6.6: (a) Snapshot of a train of TE (E_x) polarised solitons. Lateral field amplitude and inversion $W(x = 0)$ against z for propagating 2π-pulses stabilized by a 100 nm low-index gap. (b) Cross-sections of three-dimensional slot waveguide and low-index core fibre geometries supporting modes with nearly constant field profiles within the gap where the nonlinear material is placed (orange). Figure reproduced from [50].

gation, i.e. whether the pulse is a solitary wave or not, depends on general parameters of the waveguide that are well represented in $2D$, so that valid conclusions on actual $3D$ propagation can be drawn from $2D$ simulations. Figure 6.6(a) shows a snapshot of three 2π-pulses that have been injected into the waveguide in quick succession. From this figure we can already anticipate some of the results presented in detail below. First, we note that the pulse indeed stays confined to the fundamental mode with an almost constant and strongly enhanced electric field in the gap region, a much lower electric field in the high-index region, and an exponentially decreasing field in the low-index cladding. All three pulses have a very similar shape, indicating that their propagation behaviour is very stable, i.e. they may be solitary waves. From the snapshot of the inversion along the symmetry-axis of the waveguide we see that the inversion returns to -1 after the passing of each pulse. Some residual inversion can only be discerned at the entrance of the pulse into the medium, probably a consequence of imperfect numerical injection into the fundamental mode. This inversion behaviour is indicative of 2π-pulses and demonstrates the transparency effect. Nonetheless this figure is not conclusive and the therein presented results were obtained for one specific parameter combination that is favourable to solitary propagation.

A thorough understanding of the propagation of short pulses through coherent, resonant absorbers is performed by investigating dependencies of pulse absorption, broadening, and group velocity on pulse and medium parameters (see Fig. 6.7). The first investigation concerns the optimal gap width in the slot waveguide. Ideally, the width of the waveguide is large enough to allow for a high confinement factor. Nevertheless the constancy of the field profile needs to be maintained, so as not to suffer from substantial absorption. Figure 6.7(a) depicts the propagation distance dependence of the pulse energy for slot waveguides with varying gap widths. For a gap width of 200 nm we see considerable absorption during propagation. Also for $w = 140\,\text{nm}$ the Rabi-frequency varies too much, which renders absorption non-negligible. Reducing the gap width to 100 nm reduces the pulse attenuation to a value below 5 dB/cm, indicating that the Rabi-frequency across the transverse dimension of the gap is almost constant. Even lower values of pulse attenuation are achieved with a gap width of 60 nm, but it has to be considered that lowering the gap width impacts negatively on the confinement factor. On the basis of the above results we conclude that a gap width of 100 nm should be an

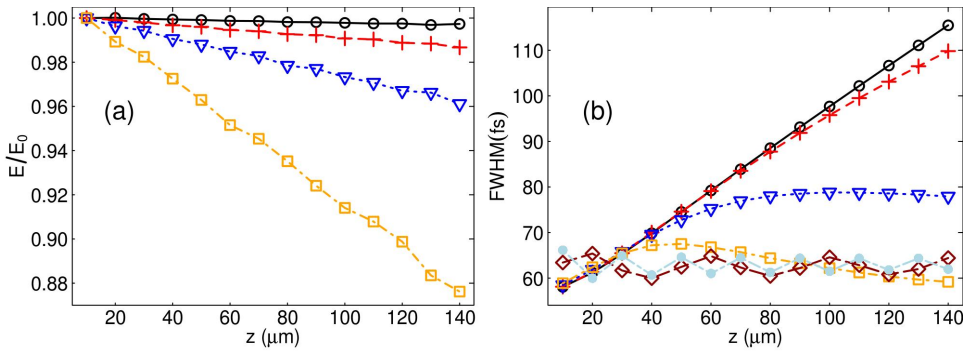


Figure 6.7: (a) Evolution of pulse energy with propagation distance for different slot widths $w = 200\,\mathrm{nm}$ (orange squares), $w = 140\,\mathrm{nm}$ (blue triangles), $w = 100\,\mathrm{nm}$ (red crosses) and $w = 60\,\mathrm{nm}$ (black circles) and an absorber density of $n = 10^{19}\,\mathrm{cm}^{-3}$. (b) FWHM against propagation distance for absorber densities of $n = 0$ (black circles), $n = 10^{17}\,\mathrm{cm}^{-3}$ (red crosses), $n = 5 \cdot 10^{17}\,\mathrm{cm}^{-3}$ (blue triangles), $n = 10^{18}\,\mathrm{cm}^{-3}$ (orange squares), $n = 5 \cdot 10^{17}\,\mathrm{cm}^{-3}$ (dark red diamonds) and $n = 10^{19}\,\mathrm{cm}^{-3}$ (full light blue circles); further parameters are $w = 100\,\mathrm{nm}$, $\tau_0 = 56\,\mathrm{fs}$.

ideal model system to study pulse propagation in resonantly absorbing gap waveguides. Consequently, this value is employed in all the following investigations.

Solitary propagation requires not only transparency, a further condition is the constancy of the temporal field profile (pulse envelope). The simplest measure of the pulse envelope, giving a strong indication on its constancy, is the pulse duration, which is measured in Fig. 6.7(b) for the example of a pulse with initial duration of $\tau = 56\,\mathrm{fs}$ that propagates through a resonantly absorbing gap waveguide. By comparing the evolution of the FWHM of the pulse with propagation distance for different absorber densities, we can identify the condition for dispersion compensation. In the absence of a resonant absorber, the pulse duration increases linearly with propagation distance as a consequence of the intrinsic waveguide dispersion that chirps the pulse. The pulse envelope is thus changed whereas the frequency content of the pulse is stable. For low absorber densities, for which the group velocity of the pulses is not influenced considerably, the pulse also spreads very strongly and reshapes. Figure 6.8(a), comparing pulse envelopes at the exit of the waveguide for the different cases included in Fig. 6.7(b), shows how the pulse envelopes are deformed while propagating through the more dilute absorbers and also indicates the pulse delay. Here, it becomes most evident that a stable pulse shape is accompanied by a considerable delay in propagation, since the pulse shape remains sech-shaped only for the slower pulses (the denser absorbers), although a background of

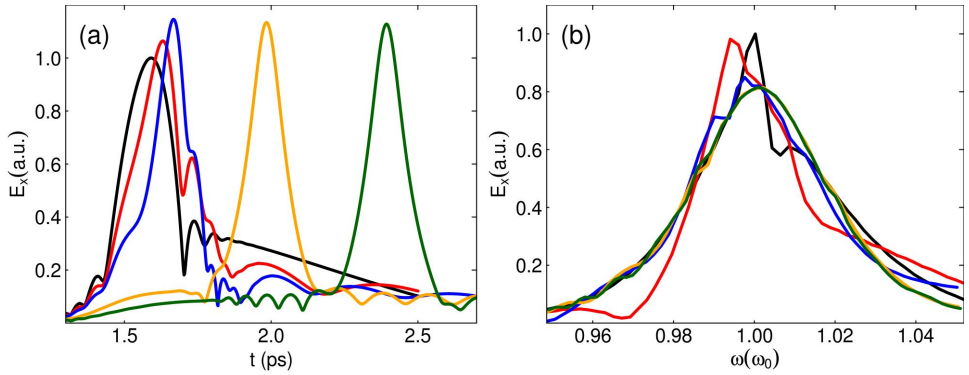


Figure 6.8: (a) Electric field envelopes and (b) spectra of pulses after propagation through 150 μm of a 100 nm slot waveguide with absorber densities of $n = 10^{17}\,\mathrm{cm}^{-3}$ (black lines), $n = 5\times10^{17}\,\mathrm{cm}^{-3}$ (red lines), $n = 10^{18}\,\mathrm{cm}^{-3}$ (blue lines), $n = 5\times10^{18}\,\mathrm{cm}^{-3}$ (orange lines) and $n = 10^{19}\,\mathrm{cm}^{-3}$ (green lines).

radiation evolves. An interesting development, documenting that the FWHM is not a reliable indicator of pulse shape, is seen for the absorber density of $n = 10^{18}\,\mathrm{cm}^{-3}$ (blue lines in both figures). After an initial increase, its FWHM decreases to its original value during propagation, but the pulse shape has become more complex with a small hump behind the initial pulse. One can thus not regard this pulse as a solitary wave.

2π-pulses propagating through the denser absorbers, however, can be said to be solitary waves for most practical purposes, if not in the strict mathematical sense. Their envelope is stable, it is even true that the pulse envelopes of the cases $n = 5\times10^{18}\,\mathrm{cm}^{-3}$ (orange lines) and $n = 10^{19}\,\mathrm{cm}^{-3}$ (green lines), and also their spectra depicted in Fig. 6.8(b) are very smooth and almost identical. The same cannot be said for the spectra of the pulses which have not experienced significant delay due to the resonant absorber. Those spectra are irregular and asymmetric and do not resemble the spectra of solitary waves. Absence of complexity in spectra and envelopes is a sign of solitary waves, whereas complexity indicates the presence of dispersion.

This principle can also be applied to FROG traces of the pulses shown in Fig. 6.9. An unchirped solitary wave results in a symmetric FROG trace with respect to the time delay and such symmetry is present in the pulses that have propagated through the gap waveguide filled with dense absorbers [see Fig. 6.9(c) and (d)]. The chirp on the pulses that have propagated through a gap waveguide filled with dilute absorbers is clearly visible in the asymmetry of the FROG trace and its more complex shape [see Fig. 6.9(a) and (b)]. Thus, the analysis of pulses propagating through waveguides with different

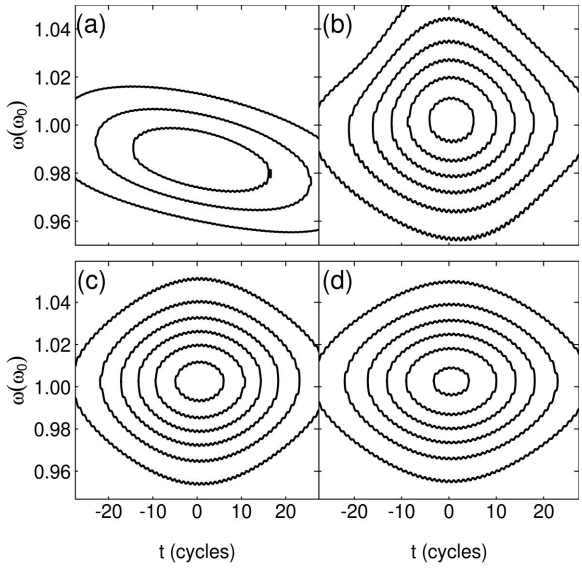


Figure 6.9: FROG plots for pulses of Fig. 6.8. Absorber densities are (a) $n = 10^{17}\,\mathrm{cm}^{-3}$, (b) $n = 10^{18}\,\mathrm{cm}^{-3}$, (c)$n = 5 \times 10^{18}\,\mathrm{cm}^{-3}$ and (d) $n = 10^{19}\,\mathrm{cm}^{-3}$.

absorber densities has revealed that solitary propagation is possible for pulses that incur significant group delay. In altering the group velocity, the absorber also alters the group velocity dispersion and when the absorber is dense enough, the nonlinearity can cancel the dispersive tendency of the waveguide.

To make predictions about dispersion behaviour, it is thus useful to examine the group velocity that a given input pulse experiences in the waveguide. An analytical formula for the group velocity is given in equation (6.15), but it has been derived by applying approximation, e.g., neglecting waveguide dispersion. In Fig. 6.10 we investigate numerically whether the analytical formula can predict the actual group velocity in the waveguide. A good agreement, especially for very fast and very slow pulses is found between analytical and numerical results. Therefore, equation (6.15) can be used to estimate the correct parameters for the planning of experiments on SIT solitary waves in resonantly absorbing waveguides.

SIT is not only characterised by propagation without attenuation and without broadening, but also by the breakup of pulses with area $\theta > 3\pi$ into two 2π-pulses with different amplitudes and group velocities. Let us examine under which conditions we can find this pulse breakup in the investigated gap waveguide. Figure 6.11 shows snapshots of electric field amplitude and inversion in the gap waveguide after a 4π-pulse has been injected

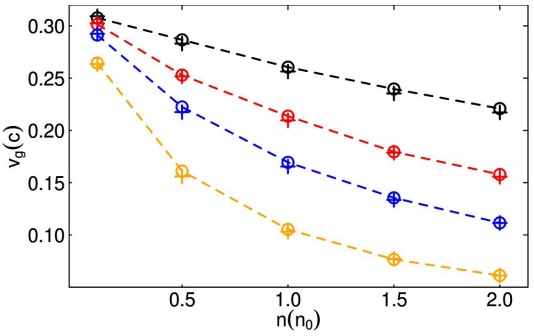


Figure 6.10: Group velocity v_g for $w = 100\,\text{nm}$ against absorber densities ($n_0 = 10^{19}\,\text{cm}^{-3}$) for initial pulse widths (τ_0) of 37 fs (black), 56 fs (red), 76fs (blue) and 113fs (orange) calculated from equation (6.15) (squares) and extracted from numerical simulations (crosses).

into the system for a dense absorber [(a) and (c)] or for a dilute absorber [(b) and (d)]. In the first case we clearly see that the pulse splits into two separate 2π-pulses, a fast and a slow one, whereas in the second case the pulse is unable to separate. This is confirmed by the results presented in Fig. 6.12 showing temporal pulse envelopes and spectra after propagation of $30\,\mu$m through the waveguide. For the dense absorber (black lines) we see a first, intense and short pulse, and a second, less intense and broader pulse well separated in their arrival time. The spectrum of the full time trace shows oscillations, which are expected to decrease with separation. In the case of the dilute absorber (red lines) the envelope shows a single pulse with a slight bump in the trailing edge; no pulse separation has occurred. The spectrum is oscillation-free but slightly asymmetric and not the spectrum of a solitary wave.

Let us now try to understand and classify the observations made. The first case (of the dense absorber) is the case in which the absorber is able to induce a pulse delay and in the second case, no significant delay is induced by the absorbing medium. A simple explanation is that two separate pulses can only develop if the pulse delay dominates over pulse broadening. Ideally, pulse broadening is completely negligible so that the pulse delay allows for the separation of an intense, short pulse and a less intense, broad pulse. Again, we find that the signatures of SIT are only observable if the absorber has a strong influence on the pulse's group velocity.

To summarise, in this section we have found that solitary waves are possible in nanoscopic waveguides if the absorber is strong enough to induce a significant pulse delay.

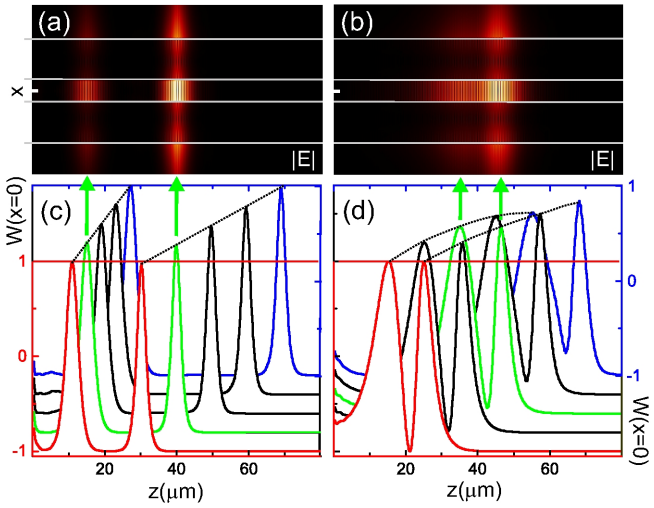


Figure 6.11: Electric field amplitude snapshots of 4π-pulses with $\tau_0 = 95\,\mathrm{fs}$ in a 2D slot waveguide for (a) $n = 10^{19}\,\mathrm{cm}^{-3}$ and (b) $n = 10^{18}\,\mathrm{cm}^{-3}$. Sequence of snapshots of the inversion at intervals of 117 fs for (c) $n = 10^{19}\,\mathrm{cm}^{-3}$ and (d) $n = 10^{18}\,\mathrm{cm}^{-3}$. Arrows indicate correspondence between $2D$ electric field and inversion snapshots (green). Figure reproduced from [50].

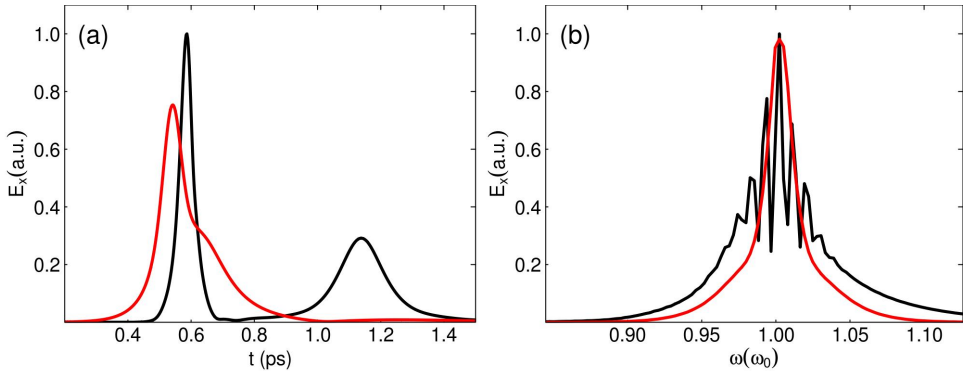


Figure 6.12: (a) Temporal electric field envelopes and (b) spectra for a 4π-pulse after propagation of $30\,\mu\mathrm{m}$ through a slot waveguide with an absorber density of $n = 10^{19}\,\mathrm{cm}^{-3}$ (black lines) and $n = 10^{18}\,\mathrm{cm}^{-3}$ (red lines).

As the pulse delay is governed by pulse intensity, absorber density and confinement factor, and on the other hand, a pulse has to be much shorter than dephasing and relaxation times in the absorbing medium, a compromise between pulse duration and absorber density has to be found to enable an experimental observation of SIT solitons in waveguides. Note that a clear delineation of the regimes was not possible in the context of this thesis due to the computational effort involved in taking just a single data point and due to the problem of determining if a given pulse can be classified as a solitary wave when close to the border of the regimes. See for example the blue data points in Fig. 6.7(b) which indicate solitary wave propagation that could only be ruled out by looking at the pulse spectrum. The possibility of waveguide dispersion compensation by the nonlinearity of a coherent, resonant absorber alone and over a broad range of pulse durations and absorber densities stands in contrast to earlier analytical results, which predicted very specific conditions for dispersion compensation [30] or ruled it out altogether [28]. Those results, however, relied on approximations that are arguably invalid for the type of nonlinearity encountered in resonant absorbers. Thus, the findings presented here give important new insights into resonant light-matter interaction in the intense pulse propagation regime through waveguiding structures.

In the following sections it will be examined whether SIT in gap waveguides is, in principle, suitable for applications and phenomena predicted using one-dimensional propagation equations. The first phenomenon to be examined are pulse collisions (see [45] and Chapter 4 of this thesis). Secondly, optical memory schemes envisioned in [42, 43] are investigated in the gap waveguide.

6.3 Pulse collisions in gap waveguides

In Chapter 4 we have discussed collisions of counterpropagating simultons in a plane-wave configuration. Having established how to achieve SIT in nano-structured waveguides it is certainly of interest to establish whether the same general collision behaviour as in the plane-wave case can also be observed in resonantly absorbing gap waveguide structures. Since a two-dimensional representation for the waveguide is chosen, there is no degree of freedom in the polarisation of the fundamental symmetric waveguide mode that we exploit for SIT. Thus, for the purpose of the numerical study of pulse collisions

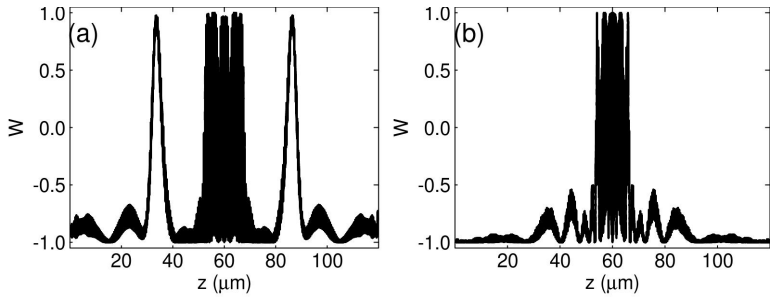


Figure 6.13: Snapshots of the inversion along the middle axis of a gap waveguide filled with resonantly absorbing two-level systems after collision of counterpropagating pulses for a density of (a) $n = 5 \times 10^{18}\,\mathrm{cm}^{-3}$ and (b) $n = 10^{19}\,\mathrm{cm}^{-3}$. The initial pulse duration is 94 fs in both cases.

in three-level media we need to employ a three-level system whose transitions are orthogonal because of different resonance frequencies. In this case orthogonality is given if the frequency content of the pulses is restricted to one transition only. Note that for an experimental situation using a fibre exhibiting rotational symmetry two degenerate modes with orthogonal polarisations exist and the polarisation dependent scheme for plane-waves can be used.

The computational complexity of the $2D$ propagation problem does not allow for a similarly exhaustive parameter scan as performed for collisions of plane-wave simultons. Hence, the following investigations are restricted to a general proof of principle demonstration, giving examples for the different regimes, namely, the two-level collision with and without solitary wave annihilation and the three-level collision with solitary wave birth and with simulton breakup. As the group velocity in a waveguide includes the waveguide dispersion, it is not expected that the same dependence on group velocity can be found for the collision regimes as in the plane-wave case.

First, let us examine the collision behaviour in a two-level medium to see whether, also in the gap waveguide, there exists a transition between inelastic collisions after which a solitary wave is still present and a collision leading to complete pulse break-up. Indeed, for a 2π-pulse collision in a gap waveguide filled with a two-level medium we find the two regimes encountered in the one-dimensional case. Figure 6.13 shows the inversion along the middle axis of the waveguide after the collision of two counterpropagating pulses for two different absorber densities. A collision in the lower density medium [Fig. 6.13(a)] allows for the pulses to keep their 2π-pulse character after collision. They

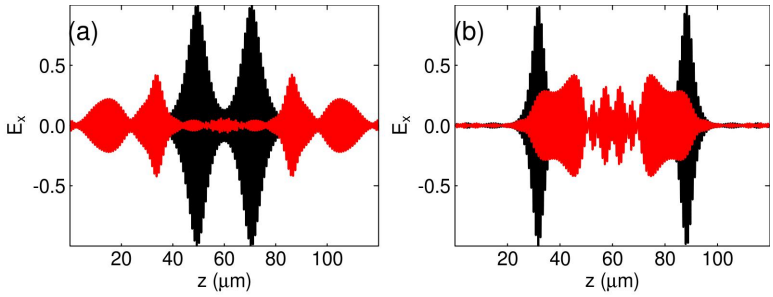


Figure 6.14: Snapshots of the electric field E_x along the middle axis of a slot waveguide filled with resonantly absorbing two-level systems after (red lines) and before (black lines) collision of counterpropagating pulses for a density of (a) $n = 5 \times 10^{18}\,\mathrm{cm}^{-3}$ and (b) $n = 10^{19}\,\mathrm{cm}^{-3}$. The initial pulse duration is 94 fs in both cases.

propagate more slowly and are less intense as they have lost energy to the excitation of the population grating in the collision region. When 2π-pulses of the same duration collide in a medium with higher absorber density, [Fig. 6.13(b)] they annihilate each other and only off-resonant radiation is left. This can be appreciated more clearly when looking at snapshots of the electric field before and after the collision of the counterpropagating pulses (see Fig. 6.14). In the case of the denser absorber a strong electric field remains after collision [see Fig. 6.14(b)], but it is not in the form of a sech-shaped pulse. It is, however, in the form of off-resonant radiation that is unable to appreciably excite the medium. In contrast, for a lower absorber density [Fig. 6.14(b)] the electric field has lost in intensity after collision, but it clearly still forms a pulse. Combined with the information given by the absorber densities we can confirm that the final pulses are 2π-pulses. To summarise, the collision of pulses in gap waveguides filled with a two-level medium or, equivalently, the collision of pulses acting on the same transition exhibits the same two regimes encountered in plane-wave collisions. No qualitative change in collision behaviour is observed by going from plane-wave pulses to guided pulses.

We have seen earlier that collisions in a three-level medium or, equivalently, collisions of pulses acting on two orthogonal transitions in a medium can lead to the birth of additional solitary waves in a plane-wave scenario. Figure 6.15(a) confirms that the same is possible in the collision of 2π-pulses guided in a nanoscopic gap waveguide. The occupation densities after the collision in the lower density absorber, and therefore faster 2π-pulse, show the clear characteristics of soliton birth; after collisions we find two 2π-pulses propagating in each direction. Figure 6.16(a), showing the accompanying

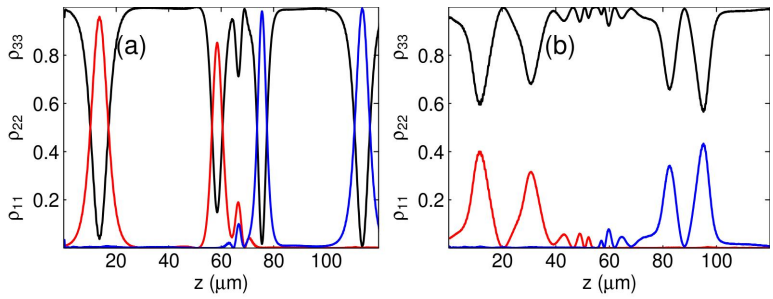


Figure 6.15: Snapshots of the occupation densities ρ_{11} (black line), ρ_{22} (red line) and ρ_{33} (blue line) along the middle axis of a slot waveguide filled with resonantly absorbing two-level systems after collision of counterpropagating pulses for a density of $n = 5 \times 10^{18}\,\mathrm{cm}^{-3}$ and an initial pulse duration of (a) 47 fs and (b) 70 fs respectively.

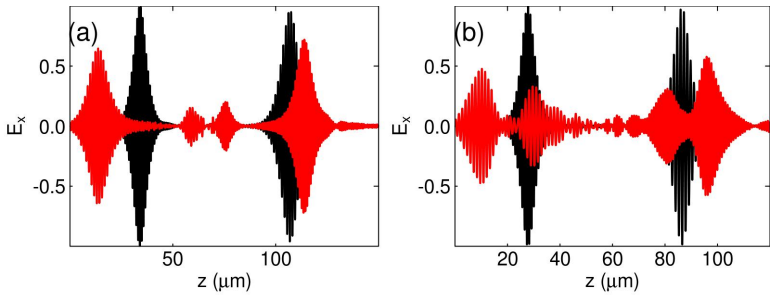


Figure 6.16: Snapshots of the electric field E_x along the middle axis of a slot waveguide filled with resonantly absorbing two-level systems after (red lines) and before (black lines) collision of counterpropagating pulses for a density of $n = 5 \times 10^{18}\,\mathrm{cm}^{-3}$ and an initial pulse duration of (a) 47 fs and (b) 70 fs respectively.

snapshot of the electric field confirms this observation. Indeed, we can distinguish intense, faster pulses to the very right and very left and slower, less intense pulses that are still close to the interaction region. Increasing the absorber density and pulse duration and thus the ratio between energy stored in the medium and energy in the electromagnetic field, we reach the regime in which the collision products are not individual solitary waves but rather interacting pulses, just as in the plane-wave case. This is supported by the occupation densities of the excited states [see Fig. 6.15(b)], which do not reach their maximum value of 1 any more, as well as from the snapshots of the electric fields [see Fig. 6.16(b)], which do not show separate pulses. To conclude, the study of pulse collisions in gap waveguides has revealed the same characteristics as the plane-wave collisions studied in Chapter 4. Therefore, nanoscopic gap waveguides or low-index core fibres could provide the platform for an experimental realisation of parameter-dependent

soliton birth.

6.4 Realisation of plane-wave SIT memory schemes in gap waveguide

In [42] Loiko *et al.* presented a scheme for the trapping of SIT solitons in an atomic medium exhibiting a Λ-type three-level system. Therein, a control pulse on the lower-frequency transition $|2\rangle \leftrightarrow |3\rangle$ is used to transfer the energy of a soliton resonant with the higher-frequency transition $|1\rangle \leftrightarrow |3\rangle$ into an atomic excitation of the higher ground-state $|2\rangle$, a phenomenon observed in [104]. Subsequently, the region of excitation can be shifted by injection of additional solitons on the transition $|2\rangle \leftrightarrow |3\rangle$ until the excitation leaves the medium and the original pulse is recovered.

Beeker *et al.* varied the proposed scheme by considering additional solitons acting on the transition $|1\rangle \leftrightarrow |3\rangle$ [43]. In this case, those additional pulses are able to create more excited regions with the relative phase of the coherence ρ_{12} depending on the amplitudes of the exciting pulses. Shifting the excitation also leads to a re-emission of the control pulse whose phase is then dependent on the phase between the original SIT pulse and the control pulse possibly enabling a logical XOR-gate.

All considerations for these schemes have been undertaken in plane-wave approximation. In this section it is investigated whether such memory schemes for Λ-type atomic media can be generalised to the gap waveguide in order to enable a realisation in compact geometries. To this end, the main result (Figure 4) of [43] in the gap waveguide geometry with a gap of 100 nm is replicated. In the analysis of [43] three regimes of interaction are delineated by the relation between the power of first and second soliton. The power of a SIT soliton is inversely proportional to its duration, so that we can also say that the first regime is given by $\tau_1 < \tau_2$, the second by $\tau_1 \geq \tau_2$ and the third one by $\tau_1 \gg \tau_2$. In the first two regimes the ground-state coherence in the region excited by the two consecutive pulses switches its phase, whereas the phase of the coherence is maintained between the two regions in the third regime. Here, only the second and third regimes are compared as the first and second regime are very similar in most aspects and do not warrant a separate discussion in this context. For $\tau_1 = \tau_2$ the first excited region is predicted to be shifted by the second soliton, but the second excited region is

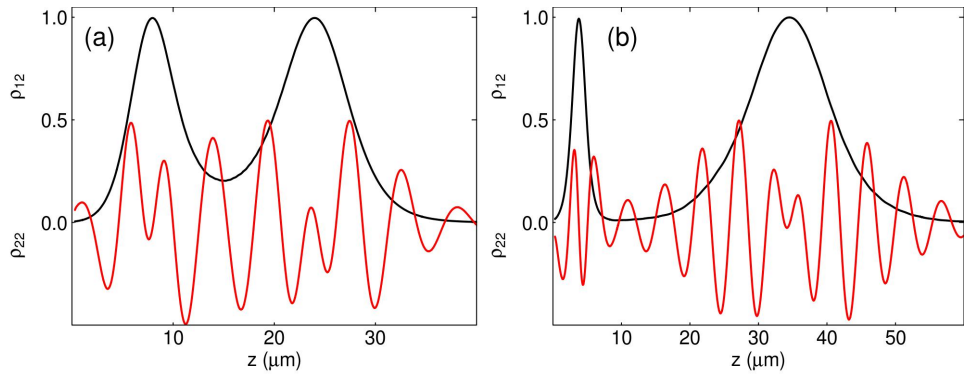


Figure 6.17: Population density ρ_{22} (black line) of the upper ground-state and inter-ground-state coherence ρ_{12} (red line) after pulses have passed for (a) $\tau_1 = \tau_2$ and (b) $\tau_1 = 6\tau_2$.

close to the first one.

Note, that the analysis of Beeker *et al.* was performed in rotating wave and slowly varying envelope approximations whereas here the full-time domain method is used. Thus, the phase of the coherence is not immediately given, but, as we will see, phase shifts are nonetheless clearly visible from the data. Further, as for the collisions, both transitions have to have the same polarisation orientation because a $2D$ calculation is performed; a fibre with rotational symmetry in the transverse dimensions could allow for SIT on transitions with different polarisations.

Comparing the coherence ρ_{12} after all pulses have left the system for $\tau_1 = \tau_2$ [Fig. 6.17(a)] to ρ_{12} for $\tau_1 = 6\tau_2$ [Fig. 6.17(b)] we observe that in the former case no phase change of ρ_{12} is present between the two excited regions. In the latter case, however, a phase change is clearly visible at the maximum of the excitation, in agreement with the predictions of Beeker *et al.* [43]. Thus, we conclude that the memory scheme proposed in [43] could be implemented in the here investigated gap waveguide.

6.5 Conclusions

In this chapter a study of pulse propagation in nonlinear and, particularly, resonantly absorbing waveguides was presented. First, conditions for the viability of one-dimensional propagation equations were formulated and a definition of effective coefficients to derive approximate one-dimensional equations was proposed for saturation nonlinearities. Next, a necessary condition for solitary wave propagation via self-induced transparency

was identified: the constancy of the Rabi-frequency over the transverse pulse profile. Using the example of the $2D$ slot waveguide filled with a resonant absorber in the low-index slot, it was found that solitary wave propagation is possible if the absorber density is high enough to induce a significant change in the group velocity, i.e. slowing-down of the pulse. In that case, the nonlinear absorber induces a dispersion that counteracts the intrinsic waveguide dispersion, enabling a stable pulse shape in time- and frequency-domain. Hence, SIT is not only able to reshape chirped pulses – pulses with accumulated dispersion – into solitons, as seen in Chapter 5, but is also able to prevent pulses from becoming chirped in a waveguide.

Studying 4π-pulse propagation, the pulse breakup was found to occur in the same group velocity regime that enables solitary wave propagation. Having thus established that all signatures of SIT are present in gap waveguides under the right conditions, simulton collisions were investigated to see if parameter-dependent soliton birth can be realised in a compact and practical configuration. Indeed, the regimes encountered in the collision of counterpropagating plane-wave simultons (Chapter 4) are also present in gap waveguide SIT of three-level systems. Thus, it may be possible to use this strong, parameter-dependent light-light interaction in waveguides for computational purposes in a realistic and compact geometry. Furthermore, an investigation of optical memory schemes devised in plane-wave approximation revealed that they possess a gap waveguide counterpart. In conclusion, SIT in nanoscopic gap waveguides filled with dense absorbers is equivalent to plane-wave SIT in the relevant aspects investigated here and it proves to be an ultra-compact and reliable realisation of SIT. Because of the strong light-light interactions in resonant absorbers, SIT in ultra-compact geometries could provide a realistic platform for efficient optical computing schemes.

Chapter 7

Summary and Outlook

In summary, this thesis presents several new theoretical results on self-induced transparency. Firstly, the collisions of counterpropagating simultons in degenerate, coherent three-level systems were studied and the birth of an additional pair of simultons was discovered. This soliton birth depends on the group velocity of the simultons and the relative polarisation of the counterpropagating pulses. For parallel polarisation of the pulses the collision behaviour in a two-level system is recovered where the initial solitons may only lose energy or break up completely and always leave a population grating in the interaction region. For orthogonal polarisation of the pulses, in contrast, the electronic population in the interaction region always returns to the ground state, whereas the 2π-pulses either split to create an additional pair of 2π-pulses or break up completely, depending on the group velocity, which in turn depends only on the ratio between energy in the electromagnetic field and energy deposited in the medium. Thus, the numerical finding of parameter-dependent soliton birth should be observable in a typical plane-wave SIT experiment by varying pulse lengths and amplitudes of counterpropagating 2π-pulses travelling through a gas cell and monitoring the output. The excited transition in the gas must thereby be degenerate (or near-degenerate) with equal oscillator strengths, e.g. a $J = 0$ to $J = 1$ transition.

Independent of an experimental confirmation of this finding, it would also be interesting to study theoretically the influence of some of the neglected phenomena such as inhomogeneous broadening or diffusion on the interaction behaviour. Additionally, the study here was restricted to a symmetrical input situation in which either two or no new

solitons were created. In situations with asymmetrical input in terms of pulse lengths (amplitudes) it should also be possible to create only one additional soliton travelling in one direction. A detailed study could potentially reveal the parameters determining whether such a scenario is expected to happen. Regarding the behaviour of counter-propagating SIT solitons it should be noted that the interaction between these solitons is much stronger than the interaction between Kerr solitons, which only induce a phase-shift in each other. Such pulse interactions could therefore open new possibilities for optical gates employed in optical computing systems that are not available using other nonlinear interactions.

Not only in this context it would be desirable to realise those interactions in a confined geometry rather than a geometry where the plane wave approximation applies. This thesis discusses the possibility of confining SIT solitons to waveguides and for the first time preforms two-dimensional numerical simulations of the Maxwell-Bloch equations in realistic dielectric waveguide structures, which provide nanoscopic confinement of light fields in the transverse direction. Waveguiding is accompanied by dispersion and to assess the influence of dispersion on SIT solitons a first study looks at the impact of chirp on soliton formation in resonant absorbers. Thereby, a dynamic transition between adiabatic rapid passage with chirped pulses and SIT is uncovered. Strongly chirped pulses that induce a complete population transfer in single absorbers are reshaped into 2π-pulses and off-resonant radiation when propagating through a dense absorbing medium, while a small initial chirp of the pulses is compensated quickly. This chirp-compensation indicates that the action of the waveguide dispersion on the light pulses may also be reduced or eliminated.

The two-dimensional simulations of waveguides reveal that solitary propagation is indeed possible in waveguides if the absorber density is strong enough to significantly influence the group velocity of the pulses and the Rabi frequency is constant over the cross-section of the absorber. The latter condition can be derived analytically from considerations of the local pulse area along the transverse dimension of the waveguide and numerical results on the propagation in dielectric slab waveguides and slot waveguides with large slot illustrate the substantial absorption and reshaping of the pulse and the residual inversion in the medium. If a 2D slot waveguide with a slot width of only 100 nm is used the propagation is shown to approach a solitary regime, in which

absorption becomes negligible and the pulse stays transform-limited in case of a substantial reduction of the group velocity by the absorbing medium. Further, it is found that soliton birth and an optical memory scheme built on SIT solitons [43] are also possible in such nanoscopic gap waveguides.

An experimental confirmation of solitary propagation in waveguides could be achieved with a waveguide featuring a nanoscopic (below 100 nm) low-index gap that can be filled with an absorbing medium, which has a well-separated transition (the transition may be degenerate if the oscillator strengths are equal) and long dephasing times. The required pulse duration τ now depends on the dipole matrix element of the absorber transition μ, its frequency ω, the absorber density N, the refractive index in the low-index gap n and the confinement factor of the field over the gap Γ. Namely, the pulse duration must fulfil $\tau^2 > \hbar\epsilon_0/(2\omega N n \mu^2 \Gamma)$. At the same time, the pulse duration must be shorter than the dephasing times in the medium that can be prolonged by cooling the apparatus.

There are several directions for further research building on the present thesis. It would be of advantage to better understand the influence of Kerr and Raman effects – inevitably occurring in waveguides – on the soliton formation. The magnitude of Kerr and Raman effects and their impact of the propagation behaviour is expected to be stronger for shorter pulses. In an experimental setting one would ideally use nanogap waveguides in which these effects are minimal. The influence of inhomogeneous broadening of the absorber may also have to be considered.

A further interesting area of research is the possibility to achieve even stronger confinement of optical solitons using plasmonic waveguides [122]. Here, the electric field propagates in the form of surface plasmons created at the interface between metals and dielectrics. Such surface plasmons suffer from high ohmic losses when tightly confined to the metal, which need to be compensated to achieve temporal solitons. An obvious approach for loss-compensation is the deployment of gain materials, an approach conventionally employed in fibre optical communication systems. It has been shown recently that metallic losses can thus be overcome [123–127], but it is unclear whether temporal solitons can be maintained when metallic loss is introduced into a waveguide. The magnitude of the gain required is orders of magnitude higher than in optical fibres bringing new challenges especially regarding the noise behaviour and the dispersion that would be introduced by the gain material.

Finally, using the numerical techniques employed in this thesis supplemented by the techniques presented in [126] the dynamics of hybrid plasmon-exciton systems could be studied. In this context, the efficiency of adiabatic rapid passage in a plasmonic environment can be studied in the regime of field enhancement and also in the regime of excitation suppression [128, 129]. In general, the coherent dynamic effects associated with those systems are represented in semi-classical finite-difference time-domain studies of such systems. The tools for research into this vibrant topic are at our disposal and it is expected that one could reveal exciting new effects of the interaction between plasmons and excitons.

Appendix A

Numerical methods

The numerical results in this thesis have been obtained by the integration of Maxwell's equation with the auxiliary-differential-equation finite-difference time-domain (ADE-FDTD) method. To this end I used an existing FDTD code, developed in our group, and extended it by the addition of the Bloch equations as auxiliary differential equations. In this chapter I describe the ADE-FDTD method and methods for the extraction of results that were used in this thesis.

The finite-difference time-domain (FDTD) method [130, 131] integrates Maxwell's curl equations (2.1) in their macroscopic form directly without approximations beyond those introduced by the numerical discretisation. Accuracy of the solutions requires that the spatial discretisation steps dx are much smaller than the wavelength of interest λ, i.e. one needs at least $dx \leq \lambda/15$. Further, stability requires that the time steps dt need to obey $dt \leq Cdx/c$, the so-called Courant criterion with the Courant number C, which depends on the number of dimensions d considered via $C = 1/\sqrt{(}d)$. In the simulations presented here, the discretisation is chosen even finer because of the need to resolve the nanoscopic geometries and/or because of better accuracy of the solution of the Bloch equations. Maxwell's equations are obviously formulated in three dimensions, however, one often encounters problems for which light propagation is restrained to one or two dimensions while the system can be assumed to be infinitely extended in the other dimensions. Because the computational and memory costs of the calculations increase exponentially with the number of dimensions considered, one commonly restricts oneself to one- or two-dimensional calculations. In this thesis, only one- or two-dimensional are

considered, so that in the next two Sections I will introduce the FDTD method for those two cases. The further sections introduce several auxiliary methods that are used to complete the FDTD method as a numerical simulation tool for the analyses performed.

A.1 FDTD in one dimension

Here, the FDTD equations for the case of a one dimensional computational domain are outlined. In the one dimensional case Maxwell's equations reduce to:

$$\frac{\partial H_y(t,z)}{\partial t} = -\frac{\partial E_x(t,z)}{\partial z} \tag{A.1}$$

$$\frac{\partial H_x(t,z)}{\partial t} = \frac{\partial E_y(t,z)}{\partial z} \tag{A.2}$$

$$\frac{\partial D_y(t,z)}{\partial t} = \frac{1}{\epsilon_b(z)}\frac{\partial H_x(t,z)}{\partial z} \tag{A.3}$$

$$\frac{\partial D_x(t,z)}{\partial t} = -\frac{1}{\epsilon_b(z)}\frac{\partial H_y(t,z)}{\partial z} \tag{A.4}$$

$$\mathbf{E}(t,z) = \frac{1}{\epsilon(z)}(\mathbf{D}(t,z) - \mathbf{P}(t,z))\,, \tag{A.5}$$

while the fields in propagation direction are static ($\partial_t E_z = \partial_t H_z = 0$) .

These equations can easily be discretised using the second order accurate Yee scheme:

$$\mathbf{H}(t+\frac{\Delta t}{2}, z+\frac{\Delta z}{2}) = \mathbf{H}(t+\frac{\Delta t}{2}, z+\frac{\Delta z}{2}) + \frac{\Delta t}{\Delta z}(\mathbf{E}(t, z+\Delta z) - \mathbf{E}(t,z)) \tag{A.6}$$

$$\mathbf{D}(t+\Delta t, z) = \mathbf{D}(t,z) + \frac{\Delta t}{\Delta z}\left(\mathbf{H}(t+\frac{\Delta t}{2}, z+\frac{\Delta z}{2}) - \mathbf{H}(t+\frac{\Delta t}{2}, z-\frac{\Delta z}{2})\right)$$

$$\mathbf{E}(t+\Delta t, z) = \frac{1}{\epsilon(z)}[\mathbf{D}(t+\Delta t, z) - \mathbf{P}(t+\Delta t, z)]\,,$$

with Δt and Δz as fixed quantities fulfilling the conditions $\Delta x \leqslant \lambda_0/15$, $\Delta t < \Delta x/c$. λ_0 denotes the shortest wavelength of interest in the particular problem.

Equation (A.6) contains the magnetic fields at times $t+\Delta t/2$ and points $z+\Delta z/2$, in effect the middle points of the interval. This enables us to calculate Maxwell's equations in an explicit integration scheme, which is of second order accuracy and stable as long as above conditions for Δt and Δz are fulfilled. Absorbing boundary conditions at the extremes of the computation domain have to be added for a simulation of open systems (see Sec. A.5). The polarisation $\mathbf{P}(z,t)$ is determined by the auxiliary differential equations (see Sec. A.3) which are integrated locally on each grid cell with the electric

field acting as the external perturbation on the medium dynamics. Finally a light pulse can be injected into the simulation domain with the so called Total Field/Scattered Field technique (Sec. A.4). Any form of light pulse is possible as long as it follows a sufficiently smooth function with a slow build up, because high frequency components in the field might get amplified numerically, thereby rendering the integration scheme unstable.

A.2 FDTD in two dimensions

In two-dimensional simulations it is assumed that structure and light field are homogeneous in one direction, here the z-direction. Therefore all derivatives of electric and magnetic fields in this direction can be set to zero to simplify the calculations. In the absence of sources and with the magnetic permeability $\mu = 1$, the resulting discrete update equations for the fields look as follows [131]

$$
\begin{aligned}
E_x|^{n+1/2}_{i,j+1/2} &= C_a(\epsilon) E_x|^{n-1/2}_{i,j+1/2} + C_b(\epsilon) \cdot \left(H_z|^{n}_{i,j+1} - H_z|^{n}_{i,j} \right) \\
E_y|^{n+1/2}_{i-1/2,j+1} &= C_a(\epsilon) E_y|^{n-1/2}_{i-1/2,j+1} + C_b(\epsilon) \cdot \left(H_z|^{n+1/2}_{i-1,j+1} - H_z|^{n}_{i,j+1} \right) \\
E_z|^{n+1/2}_{i-1/2,j+1/2} &= C_a(\epsilon) E_z|^{n-1/2}_{i-1/2,j+1/2} + \\
&\quad C_b(\epsilon) \cdot \left(H_y|^{n}_{i,j+1/2} - H_y|^{n}_{i-1,j+1/2} + H_x|^{n}_{i-1/2,j} - H_x|^{n}_{i-1/2,j+1} \right) \\
H_x|^{n+1}_{i-1/2,j+1} &= D_a H_x|^{n}_{i-1/2,j+1} + D_b \cdot \left(E_z|^{n+1/2}_{i-1/2,j+1/2} - E_z|^{n+1/2}_{i-1/2,j+3/2} \right) \\
H_y|^{n+1}_{i,j+1/2} &= D_a H_y|^{n}_{i,j+1/2} + D_b \cdot \left(E_z|^{n+1/2}_{i+1/2,j+1/2} - E_z|^{n+1/2}_{i-1/2,j+1/2} \right) \\
H_z|^{n+1}_{i,j+1} &= D_a H_z|^{n}_{i,j+1} + \\
&\quad D_b \cdot \left(E_x|^{n+1/2}_{i,j+3/2} - E_x|^{n+1/2}_{i,j+1/2} + E_y|^{n+1/2}_{i-1/2,j+1} - E_y|^{n+1/2}_{i+1/2,j+1} \right) ,
\end{aligned}
\tag{A.7}
$$

with numerical constants $D_{a,b}$ and $C_{a,b}$. In two-dimensional finite-difference time-domain simulations numerical dispersion occurs that leads to slightly different propagation speeds for different frequencies and along different angles to the grid. This problem is, however, minimised if the wavelength is resolved with many grid points [131]. In this thesis a resolution of 155 grid points per wavelength is employed for two-dimensional simulations, ensuring that numerical dispersion is negligible.

A.3 Auxiliary differential equations

The FDTD method calculates the dynamics of electric and magnetic fields in the presence of effective permittivities $\epsilon(\mathbf{r}, \mathbf{E}(\mathbf{r},t), \mathbf{B}(\mathbf{r},t))$ and permeabilities $\mu(\mathbf{r}, \mathbf{E}(\mathbf{r},t), \mathbf{B}(\mathbf{r},t))$. For permittivities and permeabilities independent of electric and magnetic fields, Maxwell's curl equations and time-independent constitutive relations are sufficient to determine the spatio-temporal dependence of the fields. If permittivities or permeabilities depend on electric or magnetic fields, however, the time-dependence of these parameters has to be calculated with auxiliary differential equations determining polarisations or currents entering the constitutive relations of electric and magnetic fields. Here, we restrict ourselves to non-magnetic materials with $\mu = 1$ and $\epsilon(\mathbf{r}, E(\mathbf{r},t))$, so that $\mathbf{H} = \mathbf{B}$ and the electric displacement is written as $\mathbf{D}(\mathbf{r},t) = \epsilon'(\mathbf{r})\mathbf{E}(\mathbf{r},t) + \mathbf{P}(\mathbf{r}, \mathbf{E}(\mathbf{r},t))$. All static permittivities are included in ϵ' (the dash will be omitted from now on) and the dynamic response is included in the polarisation $\mathbf{P}(\mathbf{r}, \mathbf{E}(\mathbf{r},t))$, which we consider to be purely local in its response to the electric field. For an absorber the local approximation amounts to a neglect of a possible diffusion of excitations, an approximation that is valid for absorbers constituted by doping impurities or fluorescent dyes and also for gaseous absorbers if the pulse durations are very short. The approximation is, however, inaccurate for excitons in semiconductors.

When the dipolar transitions of a quantum mechanical level system are coupled to Maxwell's equations, the governing Bloch equations for the density matrix have to be integrated with a 4^{th} order Runge-Kutta scheme if a high accuracy is required. Here, a complication arises because, strictly speaking, the FDTD method does not provide values for the electric field at the mid-points and end-points of a time step. Estimates for those values are, however, required for the interpolation in the Runge-Kutta scheme. One way to resolve this problem is by calculating the electric field E from the polarisation P and the electric displacement D, which can be updated without prior knowledge of the polarisation P as its time derivative does not directly depend on P (see [104]). The electric displacement can then be interpolated to the mid-point of the time step and E calculated via equation (3.13).

The FDTD code developed in the TAC group for computations in any number of dimensions does not calculate the electric displacement due to the memory overhead

associated with defining D at every grid point. Therefore, we have to define an electric displacement D at the points containing active material. Furthermore, the program allows, in principle, several polarisations stemming from different material modules to appear at a single grid cell. In that case the polarisation at the grid cell is the sum of the individual polarisations and it becomes apparent that the sum of all polarisations $\sum_{j\neq i} P_j$ has to be known before one can calculate the field E from the displacement D and the polarisation P_i. This can be achieved by redefining D in equation (3.13) as an effective displacement D' which already contains all other polarisations

$$D' = D - \sum_{j\neq i} P_j \,. \tag{A.8}$$

This ensures that all other polarisations defined in the same grid cell can be calculated in the same way as before and that we can use the Runge-Kutta scheme for the quantum mechanical level system, provided we do not define more than one Maxwell-Bloch system in the same grid cell and we always calculate this system last.

A flow-chart of the procedure looks as follows:

---

stepE:

calculate D'^n from $H^{n-1/2}$

---

stepEMat:

$D'^n = D'^{n-1} - \frac{\partial}{\partial t} P_j^n \quad \forall\, j \neq i$

save D'^n

calculate three-level system parameters P_i^n and $\hat{\rho}^n$
from
D'^{n-1}, D'^n and P_i^{n-1}

$E^n = \frac{1}{\epsilon}(D'^n - P_i^n)$

---

stepH:

calculate $H^{n+1/2}$ from E^n

---

stepHMat:

calculate $P_j^{n+1/2}$ and $N_j^{n+1/2}$
from
E^n, $P_j^{n-1/2}$ and $N_j^{n-1/2}$

$D'^n = E^n + \frac{1}{\epsilon} P_i^n$

A.4 Pulse injection via the total field/scattered field method

The total-field/scattered-field (TFSF) Method is designed to numerically inject arbitrary incident fields on the simulated structure without setting explicit temporal boundary conditions on electric and magnetic fields. Setting explicit temporal boundary conditions, i.e. setting $E(\mathbf{r}, t)$ and $H(\mathbf{r}, t)$ for all t, needs to be avoided because it introduces

spurious reflections into the setup that severely reduce the accuracy of the simulations. Built on the equivalence theorem, which states that the electromagnetic fields inside a region are defined by the fields on the surface alone, the TFSF method [131, 132] calculates the total fields, generated inside the region of interest by a source on the surface, to an accuracy limited only by the accuracy of the original FDTD code. In the region outside the surface only scattered fields are calculated, ensuring that fields in this region are zero if no materials are present in the region of interest. Thus, at the surface between the two regions the time-stepping algorithm is modified to account for the difference between total and scattered fields by adding the desired incident field. Details of the algorithm can be found in Chapter 5 of [131]. Note that the superposition principle is essential for the method in the outer (scattered field) region so that nonlinear materials should be confined to the inner region.

For the two-dimensional waveguide calculations performed here the pulses injected conform to a given mode shape of the waveguide. Consequently, the mode shape has to be calculated in a pre-calculation and then inserted in the form of a look-up table of the space-dependence of the amplitude at the TFSF surface on top of the time-dependence of the light pulse. These calculations were performed with a mode calculator. Imperfections in the injection arise especially because of the wideband nature of the incident pulses and the dispersion of the waveguide. The mode shape in the look-up table is created for the centre frequency of the pulse, so that other frequencies contain contributions of other waveguide modes. Also, electric and magnetic fields are located at different points inside the grid cell and dispersion may render the assumed incident field distributions inaccurate. Some of the original reshaping seen for the pulses that enter the absorbing medium in the slot waveguide may well be attributable to those numerical effects.

A.5 Boundary conditions

Simulation domains are always bounded since computer resources are limited. While calculating pulse propagation problems one usually wishes to assume that the structure extends much longer than in the simulation and no back-reflections from the boundary into the simulation domain should occur. In this case, absorbing boundary conditions have to be employed that minimize reflection. Throughout this thesis perfectly matched

layer (PML) absorbing boundary conditions are employed and a short explanation of them is therefore in order.

PMLs [131, 133, 134] simulate an non-physical absorbing material medium at the boundaries of the domain that is perfectly matched in propagation speed and direction for any wave frequency incident on the boundary. The match is perfect for the continuous Maxwell equations but not for the discrete Maxwell equations, i.e. a finite accuracy is associated with this technique, as with all other discrete solvers for differential equations. Usually, the accuracy of the overall simulations is limited more strongly by numerical dispersion than by the accuracy of the PMLs. For the calculations performed in this thesis uni-axial PMLs [135] with eleven additional cells were used. Such boundary conditions simulate an anisotropic, uni-axial medium with electric and magnetic permittivity tensors and perform as well as the original PMLs while assuming a physical material model. Details of the implementation can be found in Chapter 7.5 of [131]. Because the attenuation of the PMLs is proportional to the propagation constant orthogonal to the boundaries, grazing incidence constitutes a problem for both types of PMLs as significant reflection can take place. In order to minimize these reflections the two-dimensional simulations of pulse propagation in waveguides have been performed with a large lateral separation between the boundary and the waveguide structure. In this way the fields propagating along the PMLs are very small. By noting that a further increase in the separation did not perceptively change the pulse propagation, it was assured that inaccuracies due to reflections from the PMLs were negligible.

A.6 Extraction of pulse velocities

Extracting pulse velocities is always connected to measuring the change in the position of the pulse maximum from one snapshot to another snapshot at a later time. Here, the pulse maxima at different times are measured not by taking the electric field maxima but by taking the positions of the maxima of the inversion. This is a more accurate measure since the electric field maximum in a full time-domain simulation can be a half-cycle removed from the maximum of the pulse envelope, whereas the inversion maximum is not subject to those oscillations.

A.7 Frequency-resolved optical gating

Frequency-resolved optical gating (FROG) [136, 137] is intended as a measurement technique to extract pulse envelope and phase from experimentally obtained ultra-short light pulses. Since there typically are no shorter events to compare and measure the pulse with, the only way of obtaining information about the pulse is by measuring it with itself. This can be achieved by splitting the pulse, giving a variable delay to one part of it and then overlap the pulses in a nonlinear material to produce a harmonic signal. When the frequency spectrum of the signal is measured with varying pulse delay, it is possible to deduce the evolution of the pulse intensity and frequency with delay, the so-called FROG-trace. From this data the time-domain representation of the pulse can be completely reconstructed even in the presence of substantial noise since the pulse data is overdetermined by the FROG trace.

In this thesis the full shape of the pulses in time-domain is already given by the numerical data. The FROG technique is used to visualise the evolution of frequency with time, i.e. the chirp of the pulse. The polarisation gate FROG technique [137] that is most appropriate for the visualisation of chirp, therefore employed here, measures the following spectrogram

$$|E_g(\omega,\tau)|^2 \propto \left| \int_{-\infty}^{\infty} dt E_{\text{signal}}(t,\tau) e^{-i\omega t} \right|^2 , \tag{A.9}$$

with a signal field comprised of a product of electric field and gate function according to

$$E_{\text{signal}}(t,\tau) = E(t)g(t-\tau) = E(t)\left|E_{\text{env}}(t-\tau)\right|^2 . \tag{A.10}$$

E_{env} denotes the pulse envelope, which is calculated from the numerical data by interpolating the electric field's local maxima.

Bibliography

[1] J. C. Maxwell, "A dynamical theory of the electromagnetic field," Philos. T. R. Soc. **155**, 459 (1865).

[2] J. Kerr, "Xl. a new relation between electricity and light: Dielectrified media birefringent," Philosophical Magazine Series 4 **50**, 337 (1875).

[3] J. Kerr, "Liv. a new relation between electricity and light: Dielectrified media birefringent (second paper)," Philosophical Magazine Series 4 **50**, 446 (1875).

[4] H. Maiman, "Stimulated optical radiation in ruby," Nature **187**, 493 (1960).

[5] R. J. Collins, D. F. Nelson, A. L. Schawlow, W. Bond, C. G. B. Garrett, and W. Kaiser, "Coherence, narrowing, directionality, and relaxation oscillations in the light emission from ruby," Phys. Rev. Lett. **5**, 303 (1960).

[6] P. A. Franken, A. E. Hill, C. W. Peters, and G. Weinreich, "Generation of optical harmonics," Phys. Rev. Lett. **7**, 118 (1961).

[7] R. W. Terhune, P. D. Maker, and C. M. Savage, "Optical harmonic generation in calcite," Phys. Rev. Lett. **8**, 404 (1962).

[8] J. A. Giordmaine, "Mixing of light beams in crystals," Phys. Rev. Lett. **8**, 19 (1962).

[9] P. D. Maker and R. W. Terhune, "Study of optical effects due to an induced polarization third order in the electric field strength," Phys. Rev. **137**, A801 (1965).

[10] S. L. McCall and E. L. Hahn, "Self-induced transparency by pulsed coherent light," Phys. Rev. Lett. **18**, 908 (1967).

[11] G. L. Lamb, "Analytical descriptions of ultrashort optical pulse propagation in a resonant medium," Rev. Mod. Phys. **43**, 99 (1971).

[12] L. Allen and J. H. Eberly, *Optical Resonance and two-level atoms* (John Wiley & Sons, New York, 1975).

[13] A. I. Maimistov, A. M. Basharov, S. O. Elyutin, and Y. M. Sklyarov, "Present state of self-induced transparency theory," Phys. Rep. **191**, 1 (1990).

[14] S. L. McCall and E. L. Hahn, "Self-induced transparency," Phys. Rev. **183**, 457 (1969).

[15] D. J. Korteweg and G. de Vries, "Xli. on the change of form of long waves advancing in a rectangular canal, and on a new type of long stationary waves," Philosophical Magazine Series 5 **39**, 422 (1895).

[16] J. S. Russell, "Report on waves," Fourteenth meeting of the British Association for the Advancement of Science (1844).

[17] C. S. Gardner, J. M. Greene, M. D. Kruskal, and R. M. Miura, "Method for solving the korteweg-devries equation," Phys. Rev. Lett. **19**, 1095 (1967).

[18] N. J. Zabusky and M. D. Kruskal, "Interaction of "solitons" in a collisionless plasma and the recurrence of initial states," Phys. Rev. Lett. **15**, 240 (1965).

[19] J. D. Gibbon and J. C. Eilbeck, "A possible n soliton solution for a nonlinear optics equation," J. Phys. A–Math. Gen. **5**, L122 (1972).

[20] P. J. Caudrey, J. D. Gibbon, J. C. Eilbeck, and R. K. Bullough, "Exact multisoliton solutions of the self-induced transparency and sine-gordon equations," Phys. Rev. Lett. **30**, 237 (1973).

[21] A. Hasegawa and F. Tappert, "Transmission of stationary nonlinear optical pulses in dispersive dielectric fibers. i. anomalous dispersion," Appl. Phys. Lett. **23**, 142 (1973).

[22] A. Hasegawa and F. Tappert, "Transmission of stationary nonlinear optical pulses in dispersive dielectric fibers. ii. normal dispersion," Appl. Phys. Lett. **23**, 171 (1973).

[23] M. Blaauboer, B. A. Malomed, and G. Kurizki, "Spatiotemporally localized multidimensional solitons in self-induced transparency media," Phys. Rev. Lett. **84**, 1906 (2000).

[24] Y. Silberberg, "Collapse of optical pulses," Opt. Lett. **15**, 1282 (1990).

[25] A. V. Gorbach, W. Ding, O. K. Staines, C. E. de Nobriga, G. D. Hobbs, W. J. Wadsworth, J. C. Knight, D. V. Skryabin, A. Samarelli, M. Sorel, and R. M. D. L. Rue, "Spatiotemporal nonlinear optics in arrays of subwavelength waveguides," Phys. Rev. A **82**, 041802(R) (2010).

[26] H.-E. Ponath and M. Schubert, "Optical soliton-like surface phenomena," J. Mod. Opt. **30**, 1139 (1983).

[27] U. Langbein, F. Lederer, and H. E. Ponath, "Nonstationary nonlinear phenomena in optical slab-waveguides. i. general theory," Opt. Quantum Electron. **16**, 251 (1984).

[28] M. Nakazawa, E. Yamada, and H. Kubota, "Coexistence of self-induced transparency soliton and nonlinear schrödinger soliton," Phys. Rev. Lett. **66**, 2625 (1991).

[29] M. Nakazawa, Y. Kimura, K. Kurokawa, and K. Suzuki, "Self-induced-transparency solitons in an erbium-doped fiber waveguide," Phys. Rev. A **45**, R23 (1992).

[30] S. Chi, T.-Y. Wang, and S. Wen, "Theory of self-induced transparency in a kerr host medium beyond the slowly-varying-envelope approximation," Phys. Rev. A **47**, 3371 (1993).

[31] K. Porsezian and K. Nakkeeran, "Optical soliton propagation in an erbium doped nonlinear light guide with higher order dispersion," Phys. Rev. Lett. **74**, 2941 (1995).

[32] M. J. Konopnicki and J. Eberly, "Simultaneous propagation of short different-wavelength optical pulses," Phys. Rev. A **24**, 2567 (1981).

[33] G. Vemuri, G. S. Agarwal, and K. V. Vasavada, "Cloning, dragging, and parametric amplification of solitons in a coherently driven, nonabsorbing system," Phys. Rev. Lett. **79**, 3889 (1997).

[34] A. Rahman, "Optical pulse propagation in v-type media," Phys. Rev. A **60**, 4187 (1999).

[35] A. A. Afanas'ev, V. M. Volkov, V. V. Dritz, and B. A. Samson, "Interaction of counter-propagating self-induced transparency solitons," J. Mod. Opt. **37**, 165 (1990).

[36] M. J. Shaw and B. W. Shore, "Collisions of counterpropagating optical solitons," J. Opt. Soc. Am. B **8**, 1127 (1991).

[37] U. Keller, "Recent developments in compact ultrafast lasers," Nature (London) **424**, 831 (2003).

[38] R. W. Ziolkowski, J. M. Arnold, and D. M. Gogny, "Ultrafast pulse interactions with two-level atoms," Phys. Rev. A **52**, 3082 (1995).

[39] S. Hughes, "Breakdown of the area theorem: Carrier-wave rabi flopping of femtosecond optical pulses," Phys. Rev. Lett. **81**, 3363 (1998).

[40] A. V. Tarasishin, S. A. Magnitskii, V. A. Shuvaev, and A. M. Zheltikov, "Evolution of ultrashort light pulses in a two-level medium visualized with the finite-difference time domain technique," Opt. Express **8**, 452 (2001).

[41] I. P. Christov, M. M. Murnane, and H. C. Kapteyn, "High-harmonic generation of attosecond pulses in the "single-cycle" regime," Phys. Rev. Lett. **78**, 1251 (1997).

[42] Y. Loiko, C. Serrat, R. Vilaseca, V. Ahufinger, J. Mompart, and R. Corbalán, "Ultrashort pulse control of space-dependent excitations in a three-level system," Phys. Rev. A **75**, 023801 (2007).

[43] W. P. Beeker, C. J. Lee, E. Can, and K. J. Boller, "Storage by trapping and spatial staggering of multiple interacting solitons in λ-type media," Phys. Rev. A **82**, 053839 (2010).

[44] M. Romagnoli, S. Wabnitz, and L. Zoccolotti, "Ultrashort soliton switching based on coherent energy hiding," Opt. Lett. **16**, 1249 (1991).

[45] A. Pusch, J. M. Hamm, and O. Hess, "Controllable interaction of counterpropagating solitons in three-level media," Phys. Rev. A **82**, 023805 (2010).

[46] V. R. Almeida, Q. Xu, C. A. Barrios, and M. Lipson, "Guiding and confining light in void nanostructure," Opt. Lett. **29**, 1209 (2004).

[47] Q. Xu, V. R. Almeida, R. R. Panepucci, and M. Lipson, "Experimental demonstration of guiding and confining light in nanometer-size low-refractive-index material," Opt. Lett. **29**, 1626 (2004).

[48] G. S. Wiederhecker, C. M. B. Cordeiro, F. Couny, F. Benabid, S. A. Maier, J. C. Knight, C. H. B. Cruz, and H. L. Fragnito, "Field enhancement within an optical fibre with a subwavelength air core," Nat. Photon. **1**, 115 (2007).

[49] T. Fujisawa and M. Koshiba, "Guided modes of nonlinear slot waveguides," IEEE Photonic. Tech. L. **18**, 1530 (2006).

[50] A. Pusch, J. M. Hamm, and O. Hess, "Femtosecond nanometer-sized optical solitons," Phys. Rev. A **84**, 023827 (2011).

[51] N. N. Rosanov, V. E. Semenov, and N. V. Vyssotina, "Collisions of few-cycle dissipative solitons in active nonlinear fibers," Laser Phys. **17**, 1311 (2007).

[52] V. S. Malinovsky and J. L. Krause, "General theory of population transfer by adiabatic rapid passage with intense, chirped laser pulses," Eur. Phys. J. D **14**, 147 (2001).

[53] M. R. Fetterman, J. C. Davis, D. Goswami, W. Yang, and W. S. Warren, "Propagation of complex laser pulses in optically dense media," Phys. Rev. Lett. **82**, 3984 (1999).

[54] J. C. Davis, M. R. Fetterman, W. S. Warren, and D. Goswami, "Propagation of complex shaped ultrafast pulses in highly optically dense samples," J. Chem. Phys. **128**, 154312 (2008).

[55] J. Laegsgaard, "Mode profile dispersion in the generalised nonlinear schrödinger equation," Opt. Express **15**, 16110 (2007).

[56] A. Pusch, J. M. Hamm, and O. Hess, "Dynamic transition from complete population transfer to self-induced transparency," Phys. Rev. A **85**, 043807 (2012).

[57] S. M. Dutra, *Cavity Quantum Electrodynamics: The strange theory of light in a box* (Wiley Interscience, 2005).

[58] D. Braak, "Integrability of the rabi model," Phys. Rev. Lett. **107**, 100401 (2011).

[59] H. Kogelnik, in *Integrated Optics*, Topics in Applied Physics, Vol. 7 (Springer Berlin / Heidelberg, 1975) pp. 13–81.

[60] C. R. Doerr and H. Kogelnik, "Dielectric waveguide theory," J. Lightwave Technol. **26**, 1176 (2008).

[61] V. Shahraam Afshar and T. M. Monro, "A full vectorial model for pulse propagation in emerging waveguides with subwavelength structures part i: Kerr nonlinearity," Opt. Express **17**, 2298 (2009).

[62] M. D. Turner, T. M. Monro, and V. Shahraam Afshar, "A full vectorial model for pulse propagation in emerging waveguides with subwavelength structures part ii: Stimulated raman scattering," Opt. Express **17**, 11565 (2009).

[63] J. Joannopoulos, P. R. Villeneuve, and S. Fan, "Photonic crystals," Solid State Commun. **102**, 165 (1997).

[64] S. Noda, K. Tomoda, N. Yamamoto, and A. Chutinan, "Full three-dimensional photonic bandgap crystals at near-infrared wavelengths," Science **289**, 604 (2000).

[65] Y. Xiao-Li, "Light guiding in a slot waveguide that includes an additional confining core region," Opt. Express **18**, 6408 (2010).

[66] T. Fujisawa and M. Koshiba, "All-optical logic gates based on nonlinear slot-waveguide couplers," J. Opt. Soc. Am. B **23**, 684 (2006).

[67] E. Shahmoon, G. Kurizki, M. Fleischhauer, and D. Petrosyan, "Strongly interacting photons in hollow-core waveguides," Phys. Rev. A **83**, 033806 (2011).

[68] L. F. Mollenauer, R. H. Stolen, and J. P. Gordon, "Experimental observation of picosecond pulse narrowing and solitons in optical fibers," Phys. Rev. Lett. **45**, 1095 (1980).

[69] J. R. Taylor, ed., *Optical Solitons – Theory and Experiment* (Cambrigde Univ. Press, 1992).

[70] Y. S. Kivshar and G. P. Agrawal, *Optical solitons* (Elsevier Science, 2003).

[71] V. E. Zakharov and A. B. Shabat, "A scheme for integrating the nonlinear equations of mathematical physics by the method of the inverse scattering problem. i," Funct. Anal. Appl+ **8**, 226 (1974).

[72] T. Aktosun, in *Encyclopedia of Complexity and Systems Science*, edited by R. A. Meyers (Springer New York, 2009) pp. 4960–4971.

[73] P. D. Lax, "Integrals of nonlinear equations of evolution and solitary waves," Commun. Pur. Appl. Math. **21**, 467 (1968).

[74] M. J. Ablowitz, D. J. Kaup, A. C. Newell, and H. Segur, "Nonlinear-evolution equations of physical significance," Phys. Rev. Lett. **31**, 125 (1973).

[75] P. Urquhart, "Review of rare earth doped fibre lasers and amplifiers," IEE Proc–J **135**, 385 (1988).

[76] F. Bloch, "Nuclear induction," Phys. Rev. **70**, 460 (1946).

[77] R. P. Feynman, F. L. Vernon, and R. W. Hellwarth, "Geometrical representation of the schroedinger equation for solving maser problems," J. Appl. Phys. **28**, 49 (1957).

[78] I. I. Rabi, "Space quantization in a gyrating magnetic field," Phys. Rev. **51**, 652 (1937).

[79] D. V. Novitsky, "Local field effect as a function of pulse duration," Phys. Rev. A **82**, 015802 (2010).

[80] C. M. Bowden and J. P. Dowling, "Near-dipole-dipole effects in dense media: Generalized maxwell-bloch equations," Phys. Rev. A **47**, 1247 (1993).

[81] M. M. T. Loy, "Observation of population inversion by optical adiabatic rapid passage," Phys. Rev. Lett. **32**, 814 (1974).

[82] N. V. Vitanov, T. Halfmann, B. W. Shore, and K. Bergmann, "Laser-induced population transfer by adiabatic passage techniques," Annu. Rev. Phys. Chem. **52**, 763 (2001).

[83] M. Born and V. Fock, "Beweis des adiabatensatzes," Z. Phys. A–Hadron. Nucl. **51**, 165 (1928).

[84] W. S. Warren, H. Rabitz, and M. Dahleh, "Coherent control of quantum dynamics: The dream is alive," Science **259**, 1581 (1993).

[85] J. S. Melinger, S. R. Gandhi, A. Hariharan, D. Goswami, and W. S. Warren, "Adiabatic population transfer with frequency-swept laser pulses," J. Chem. Phys. **101**, 6439 (1994).

[86] W. Warren, "Effects of pulse shaping in laser spectroscopy and nuclear magnetic resonance," Science **242**, 878 (1988).

[87] A. Assion, T. Baumert, M. Bergt, T. Brixner, B. Kiefer, V. Seyfried, M. Strehle, and G. Gerber, "Control of chemical reactions by feedback-optimized phase-shaped femtosecond laser pulses," Science **282**, 919 (1998).

[88] C. Brunel, B. Lounis, P. Tamarat, and M. Orrit, "Triggered source of single photons based on controlled single molecule fluorescence," Phys. Rev. Lett. **83**, 2722 (1999).

[89] D. Goswami, "On the practicality of adiabatic quantum computing with optical schemes," IJQI **5**, 179 (2007).

[90] Y. Wu, I. M. Piper, M. Ediger, P. Brereton, E. R. Schmidgall, P. R. Eastham, M. Hugues, M. Hopkinson, and R. T. Phillips, "Population inversion in a single ingaas quantum dot using the method of adiabatic rapid passage," Phys. Rev. Lett. **106**, 067401 (2011).

[91] C.-M. Simon, T. Belhadj, B. Chatel, T. Amand, P. Renucci, A. Lemaitre, O. Krebs, P. A. Dalgarno, R. J. Warburton, X. Marie, and B. Urbaszek, "Robust quantum

dot exciton generation via adiabatic passage with frequency-swept optical pulses," Phys. Rev. Lett. **106**, 166801 (2011).

[92] R. B. Vrijen, D. I. Duncan, and L. D. Noordam, "Limitations on quantum ladder climbing in complex systems," Phys. Rev. A **56**, 2205 (1997).

[93] K. Mishima and K. Yamashita, "Theoretical study on quantum control of photodissociation and photodesorption dynamics by femtosecond chirped laser pulses," J. Chem. Phys. **110**, 7756 (1999).

[94] R. K. Bullough, P. J. Caudrey, J. C. Eilbeck, and J. D. Gibbon, "A general theory of self-induced transparency," Opt. Quant. Electron. **6**, 121 (1974).

[95] N. Wright and M. C. Newstein, "Self-focusing of coherent pulses," Opt. Commun. **9**, 8 (1973).

[96] H. M. Gibbs, B. Bölger, F. P. Mattar, M. C. Newstein, G. Forster, and P. E. Toschek, "Coherent on-resonance self-focusing of optical pulses in absorbers," Phys. Rev. Lett. **37**, 1743 (1976).

[97] J. de Lamare, M. Comte, and P. Kupecek, "Spatial distortions of laser pulses in coherent on-resonance propagation: Large-scale self-focusing," Phys. Rev. A **50**, 3366 (1994).

[98] Y. Niu, K. Xia, N. Cui, S. Gong, and R. Li, "Spatiotemporal evolution and multiple self-focusing of ultrashort pulses in a resonant two-level medium," Phys. Rev. A **78**, 063835 (2008).

[99] J. de Lamare, P. Kupecek, and M. Comte, "Spatial distortions of laser pulses in coherent on-resonance propagation: Small-scale self-focusing," Phys. Rev. A **51**, 4289 (1995).

[100] I. M. Asher, "Experimental investigation of self-induced transparency and pulse delay in ruby," Phys. Rev. A **5**, 349 (1972).

[101] R. E. Slusher and H. M. Gibbs, "Self-induced transparency in atomic rubidium," Phys. Rev. A **5**, 1634 (1972).

[102] F. A. Hopf and M. O. Scully, "Transient-pulse behavior and self-induced transparency," Phys. Rev. B **1**, 50 (1970).

[103] P. D. Drummond, "Formation and stability of vee simultons," Opt. Commun. **49**, 219 (1984).

[104] Y. Loiko and C. Serrat, "Coherent and phase-sensitive phenomena of ultrashort laser pulses propagating in three-level lambda-type systems studied with the finite-difference time-domain method," Phys. Rev. A **73**, 063809 (2006).

[105] D. V. Novitsky, "Femtosecond pulses in a dense two-level medium: Spectral transformations, transient processes, and collisional dynamics," Phys. Rev. A **84**, 013817 (2011).

[106] A. V. Gorbach and D. V. Skryabin, "Soliton self-frequency shift, non-solitonic radiation and self-induced transparency in air-core fibers," Opt. Express **16**, 4858 (2008).

[107] R. T. Deck and G. L. Lamb, "Phase variation in coherent-optical-pulse propagation," Phys. Rev. A **12**, 1503 (1975).

[108] L. V. Hmurcik and D. J. Kaup, "Solitons created by chirped initial profiles in coherent pulse propagation," J. Opt. Soc. Am. **69**, 597 (1979).

[109] N. Karasawa, S. Nakamura, N. Nakagawa, M. Shibata, R. Morita, H. Shigekawa, and M. Yamashita, "Comparison between theory and experiment of nonlinear propagation for a-few-cycle and ultrabroadband optical pulses in a fused-silica fiber," IEEE J. Quantum Elect. **37**, 398 (2001).

[110] N. Akhmediev and V. V. Afanasjev, "Novel arbitrary-amplitude soliton solutions of the cubic-quintic complex ginzburg-landau equation," Phys. Rev. Lett. **75**, 2320 (1995).

[111] A. Maluckov, L. Hadžievski, N. Lazarides, and G. P. Tsironis, "Left-handed metamaterials with saturable nonlinearity," Phys. Rev. E **77**, 046607 (2008).

[112] P. P. Beličev, I. Ilić, V. Milanović, J. Radovanović, and L. Hadžievski, "Tunneling

times in metamaterials with saturable nonlinearity," Phys. Rev. A **80**, 023821 (2009).

[113] U. Keller and A. C. Trooper, "Passively modelocked surface-emitting semiconductor lasers," Phys. Rep. **429**, 67 (2006).

[114] J. Travers, J. Morgenweg, E. Obraztsova, A. Chernov, E. Kelleher, and S. Popov, "Using the e22 transition of carbon nanotubes for fiber laser mode-locking," Laser Phys. Lett. **8**, 144 (2011).

[115] A. Guzman, M. Romagnoli, and S. Wabnitz, "Self–induced transparency soliton digital switch," Appl. Phys. Lett. **56**, 614 (1990).

[116] V. V. Kozlov, "Self-induced transparency soliton laser via coherent mode locking," Phys. Rev. A **56**, 1607 (1997).

[117] J. Zeng, J. Zhou, G. Kurizki, and T. Opatrny, "Backward self-induced transparency in metamaterials," Phys. Rev. A **80**, 061806 (2009).

[118] M. A. Talukder and C. R. Menyuk, "Self-induced transparency modelocking of quantum cascade lasers in the presence of saturable nonlinearity and group velocity dispersion," Opt. Express **18**, 5639 (2010).

[119] V. V. Kozlov, N. N. Rosanov, and S. Wabnitz, "Obtaining single-cycle pulses from a mode-locked laser," Phys. Rev. A **84**, 053810 (2011).

[120] S. Kakei and J. Satsuma, "Multi-soliton solutions of a coupled system of the nonlinear schrödinger equation and the maxwell-bloch equations," J. Phys. Soc. Jpn. **63**, 885 (1994).

[121] A. Kundu, "Hidden possibilities in controlling optical soliton in fiber guided doped resonant medium," AIP Advances **1**, 022137 (2011).

[122] A. D. Boardman, G. S. Cooper, A. A. Maradudin, and T. P. Shen, "Surface-polariton solitons," Phys. Rev. B **34**, 8273 (1986).

[123] M. C. Gather, K. Meerholz, N. Danz, and K. Leosson, "Net optical gain in a plasmonic waveguide embedded in a fluorescent polymer," Nat. Photon. **4**, 457 (2010).

[124] S. Xiao, V. P. Drachev, A. V. Kildishev, X. Ni, U. K. Chettiar, H.-K. Yuan, and V. M. Shalaev, "Loss-free and active optical negative-index metamaterials," Nature (London) **466**, 735 (2010).

[125] S. Wuestner, A. Pusch, K. L. Tsakmakidis, J. M. Hamm, and O. Hess, "Overcoming losses with gain in a negative refractive index metamaterial," Phys. Rev. Lett. **105**, 127401 (2010).

[126] S. Wuestner, A. Pusch, K. L. Tsakmakidis, J. M. Hamm, and O. Hess, "Gain and plasmon dynamics in negative-index metamaterials," Phil. Trans. R. Soc. A **369**, 3525 (2011).

[127] A. Pusch, S. Wuestner, J. M. Hamm, K. L. Tsakmakidis, and O. Hess, "Coherent amplification and noise in gain-enhanced nanoplasmonic metamaterials: A maxwell-bloch langevin approach," ACS Nano **6**, 2420 (2012).

[128] R. D. Artuso and G. W. Bryant, "Strongly coupled quantum dot-metal nanoparticle systems: Exciton-induced transparency, discontinuous response, and suppression as driven quantum oscillator effects," Phys. Rev. B **82**, 195419 (2010).

[129] S. M. Sadeghi, "The inhibition of optical excitations and enhancement of rabi flopping in hybrid quantum dot–metallic nanoparticle systems," Nanotechnology **20**, 225401 (2009).

[130] K. Yee, "Numerical solutions of initial boundary value problems involving maxwell's equations in isotropic media," IEEE T. Antenn. Propag. **AP-14**, 302 (1966).

[131] A. Taflove and S. C. Hagness, *Computational Electrodynamics: The Finite-Difference Time-Domain Method, Third Edition* (Artech House, 2005).

[132] D. E. Merewether, R. Fisher, and F. W. Smith, "On implementing a numeric huygen's source scheme in a finite difference program to illuminate scattering bodies," IEEE T. Nucl. Sci. **27**, 1829 (1980).

[133] J.-P. Berenger, "A perfectly matched layer for the absorption of electromagnetic waves," J. Comput. Phys. **114**, 185 (1994).

[134] J.-P. Berenger, "Improved pml for the fdtd solution of wave-structure interaction problems," IEEE T. Antenn. Propag. **45**, 466 (1997).

[135] Z. Sacks, D. Kingsland, R. Lee, and J.-F. Lee, "A perfectly matched anisotropic absorber for use as an absorbing boundary condition," IEEE T. Antenn. Propag. **43**, 1460 (1995).

[136] R. Trebino and D. J. Kane, "Using phase retrieval to measure the intensity and phase of ultrashort pulses: frequency-resolved optical gating," J. Opt. Soc. Am. A **10**, 1101 (1993).

[137] R. Trebino, K. W. DeLong, D. N. Fittinghoff, J. N. Sweetser, M. A. Krumbugel, B. A. Richman, and D. J. Kane, "Measuring ultrashort laser pulses in the time-frequency domain using frequency-resolved optical gating," Rev. Sci. Instrum. **68**, 3277 (1997).